FINITE-ELEMENT ANALYSIS OF INNER EAR HAIR BUNDLES: A PARAMETER STUDY OF BUNDLE MECHANICS

by

Robert Keith Duncan

Thesis submitted to the Faculty of the
Virginia Polytechnic Institute and State University
in partial fulfillment of the requirements for the degree of

MASTER OF SCIENCE

in

Engineering Mechanics

Approved:

J. W. Grant

O. H. Griffin

R. W. Landgraf

August, 1993
Blacksburg, Virginia

C.2

FINITE-ELEMENT ANALYSIS OF INNER EAR HAIR BUNDLES: A PARAMETER STUDY OF BUNDLE MECHANICS

by

Robert Keith Duncan

Committee Chairman: J. W. Grant

Engineering Science and Mechanics

(Abstract)

Inner ear hair cells have been identified as the sites of mechanoelectrical transduction from a mechanical event (e.g. hearing, motion) to an electrical event (e.g. neural response). Deflection of bundles of hair-like stereocilia extending from these cells has been associated with the transduction process. Stereocilia bundle structure and stiffness controls deflection and thus the fundamental sensitivity of the transduction process. The finite-element method was used along with analytical techniques to characterize individual stereocilium and stereocilia bundle stiffnesses. A three 'stack' bundle with a Young's modulus of 3 GPa (F-actin protein) and Poisson's ratio of 0.4 (nearly incompressible) resulted in a stiffness of $K = 2.1 \times 10^{-3}$ N/m. This value is within the range of experimentally determined stiffnesses. Tip-link and subapical band interconnecting structures each contribute significantly to bundle stiffness and each could act as the gating-spring in transduction models, which propose gating structures as a means of regulating ionic activity and therefore neural activity. Stiffness depends most strongly on individual stereocilium geometry and material description, tip-link orientation and material description, and stereocilia bundle width. Stiffness depends least on stereocilia height variations and subapical bands configuration. Linear analysis was reliable up to deflections of 3.5 μm, the upper limit of physical response. Preliminary dynamic response indicates a natural frequency of 382 kHz for the vibration mode resembling physical deformation behavior. Future models should include hexagonal bundle arrangements, transversely isotropic stereocilia material descriptions, and viscoelastic tip-link behavior.

ACKNOWLEDGEMENTS

I would first acknowledge my Lord and God Jesus Christ for giving me the courage and strength necessary to undertake and complete this work. This thesis was also made possible through the advice and instruction of my advisory committee: Dr. J. W. Grant, Dr. H. Griffin, and Dr. R. Landgraf. Dr. Grant introduced me to the world of biomedical engineering as an undergraduate. Without his continuous guidance and support, this research would not have been possible. Dr. Griffin was my definitive source for understanding the complexities of finite element analysis. I have him to thank for correcting many of my analytical and computational errors. I would also like to thank Dr. Landgraf for broadening my scope of engineering and first opening my eyes to the creative world of research.

There are many others who I also have to thank for what is sentimentally called moral support. My parents, who have always been a source of encouragement and understanding, receive my utmost appreciation. To B.T. Owen, thanks for going the extra mile to help me with some of the figures. To everyone in the BME lab who put up with constant groaning and pacing, I'm truly grateful. I would also like to express my dedication of this paper to my wife, Cynthia, without whose love and support I would be lost in this world.

TABLE OF CONTENTS

LIST OF FIGURES

LIST OF TABLES

1.0 INTRODUCTION

1.1 ANATOMY AND PHYSIOLOGY

In order to understand the problem of modeling inner ear hair bundles, a prior knowledge of the anatomy and physiology of the inner ear is necessary. This section will begin by discussing the macroscopic divisions of the inner ear proceeding then to specific sensory regions finally detailing the inner ear hair cells. This discussion will accomplish two main goals by (1) providing the vocabulary necessary for understanding this work and (2) introducing some difficulties in biomedical modeling.

The inner ear is a labyrinth of winding passages consisting of membranous organs as in Figure 1 (Friedmann and Ballantyne, 1984). The anatomy of the inner ear can be categorized into three main divisions: the vestibular (motion-sensing) region, the cochlear apparatus (hearing), and an endolymphatic system. The endolymphatic system provides the endolymph fluid which fills the organs of the vestibule and the cochlea. A perilymph fluid separates the organs of the inner ear from their protective shell of bone.

The vestibular region includes the three semicircular canals, the utricle, and the saccule. Each of these structures contains regions of specialized sensory epithelia. Sensory epithelium are comprised of both supporting cells and sensory cells, or hair cells. These regions are called cristae in the semicircular canals and maculae in the utricle and saccule as shown in Figure 2. The sensory epithelia of the macula sacculi, macula utriculi, and the three cristae are composed of two types of cells as illustrated in Figure 3. The type 1 cell is rounded and flask shaped and is surrounded by a nerve. The type 2 cell is cylindrically shaped with nerves in contact at its base. The functional differences between these two types of cells is still unknown.

The sensory epithelia of the cochlea are contained in the organ of Corti. The cross-sectional view of the cochlea in Figure 4 shows the spiralling pattern of the organ of Corti as it winds through the passages of the cochlea. The enlarged view of the organ of Corti illustrates supporting cells and membranes as well as the two divisions of sensory cells,

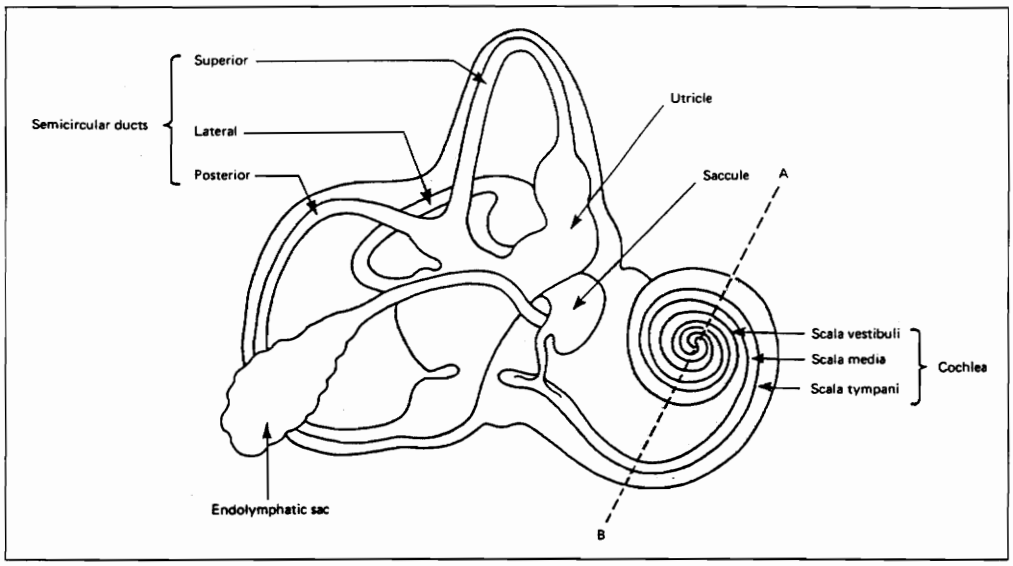

Figure 1. Schematic drawing of the inner ear (Friedmann and Ballantyne, 1984).
The inner ear can be divided into three main regions: the cochlea, the vestibular apparatus, and the endolymphatic system. The vestibular apparatus is represented in this illustration by the semicircular ducts, the utricle, and the saccule. The cochlea is traditionally associated with hearing, whereas the vestibular apparatus is associated with motion.

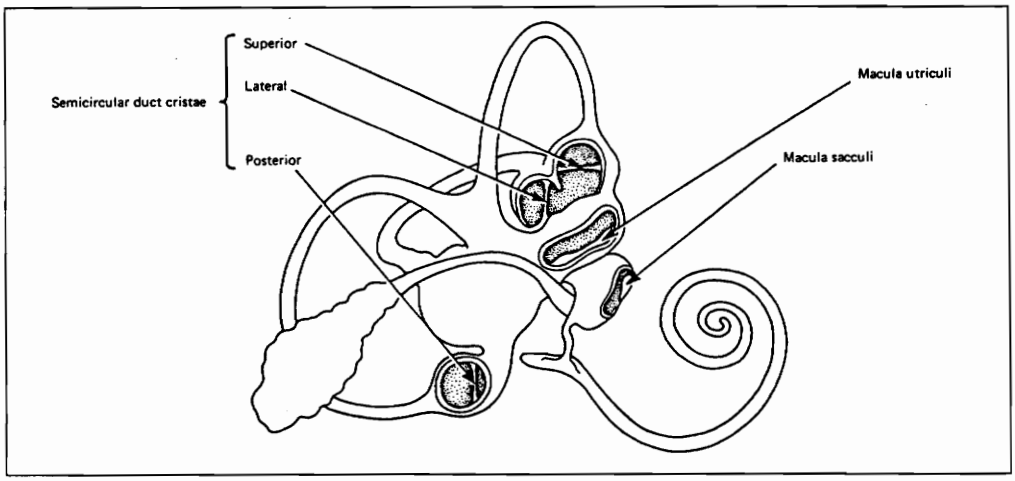

Figure 2. The vestibular sensory cell regions, or epithelia (Friedmann and Ballantyne, 1984).
The sensory regions in the semicircular ducts are called cristae, whereas in the utricle and saccule, these regions are called maculae.

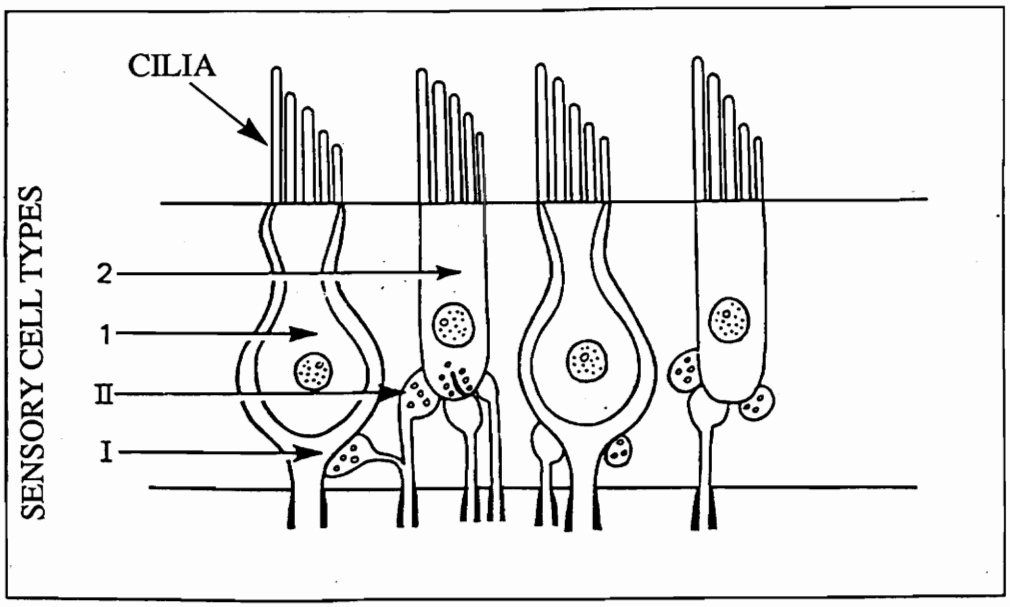

Figure 3. Vestibular sensory cell types (Friedmann and Ballantyne, 1984).
These sensory cells represent the two cell types in the vestibular apparatus. The type 1 cell is rounded and flask shaped surrounded by the type I nerve. The type 2 cell is cylindrical in shape with button type II nerves attached at its base.

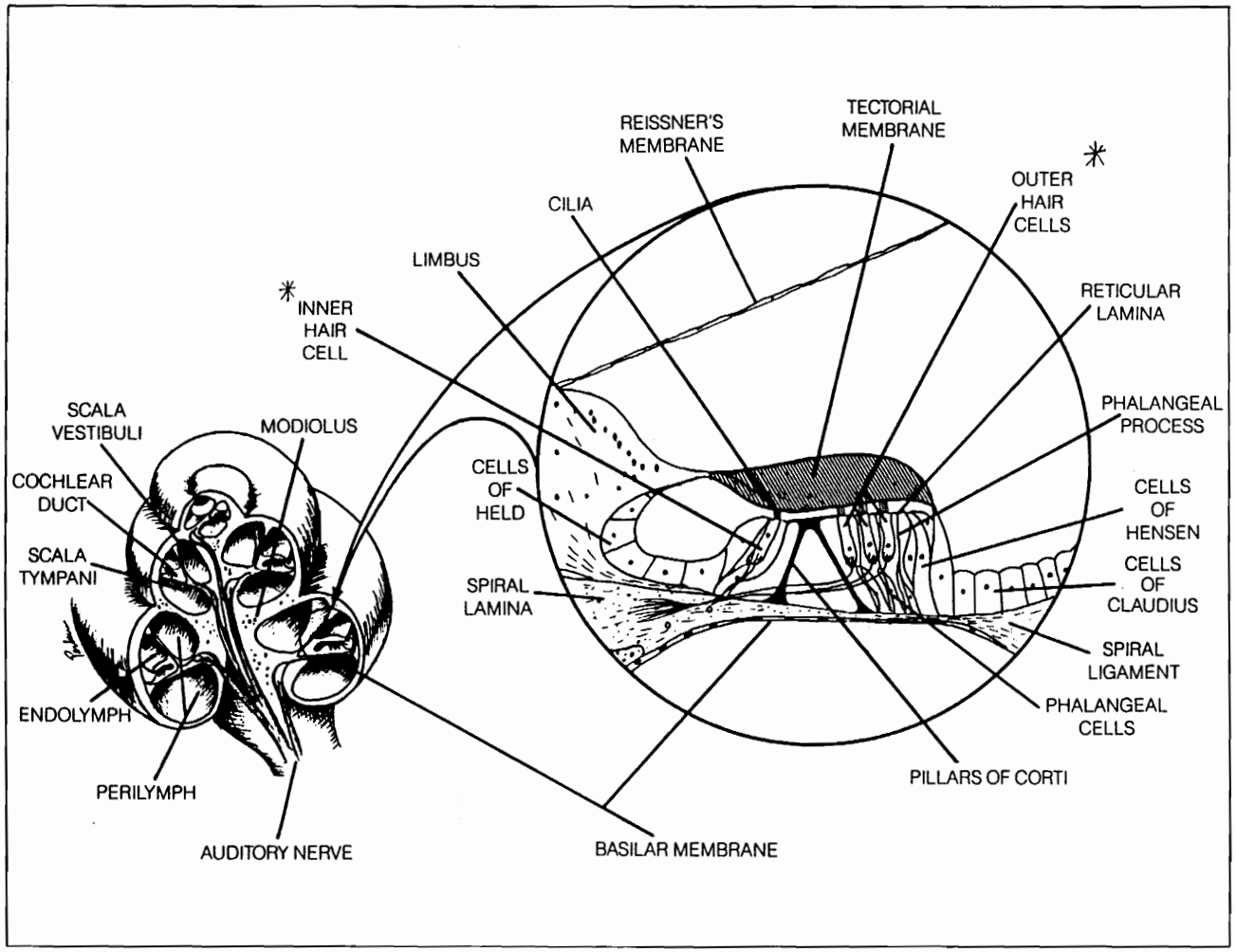

Figure 4. Organ of Corti (Perkins and Kent, 1986).

The organ of Corti is the sensory structure in the cochlea. A cross-section of the cochlea is illustrated and labelled to the left. A blow-up of the organ of Corti is shown to the right. An asterisk (*) marks the inner and outer hair cells, which are the sensory cells in the cochlea.

inner and outer hair cells. The inner hair cells are bulbous in form similar to that of the type 1 sensory cells of the vestibule. The outer hair cells are columnar in shape as compared with the type 2 cells of the vestibule.

The hair cells located throughout the inner ear have three basic structures in common as illustrated in Figure 3: (1) the sensory cell, (2) the small hairs extending from the top surface, and (3) an attached nerve. The hairs are called cilia and are broken down into two categories: stereocilia and kinocilia. Stereocilia are slender, cylindrically shaped hairs that taper at their base and connect to the sensory cell. Each cell has a bundle of stereocilia arranged in a staircase fashion of varying degrees in number and in height. Also, some cells have a large, cylindrically shaped hair called a kinocilium located at the apex of the bundle. In mammals, kinocilia are not present in the hearing apparatus, yet appear in vestibular hair bundles. Kinocilia and stereocilia are arranged in various configurations. Before detailing these structures further and presenting them in figures, some caution must be addressed as to the reliability of techniques in ultrastructural anatomy.

1.1.1 Techniques In Ultrastructural Anatomy

Characterization of inner ear hair cells is particularly difficult due to their size, on the order of micrometers. Two standard ultrastructural techniques have been developed and used: transmission electron microscopy (TEM) and scanning electron microscopy (SEM) (Friedmann and Ballantyne, 1984). In TEM an electron beam is transmitted through the specimen producing the micrograph, while in SEM an image is formed from the secondary electrons emanating from the specimen's coated surface. The resulting micrographs not only show the morphology of the specimens, but can allude to connectivity and material considerations through changes in the shades of electron density.

Differences in technique also arise in specimen preparation. The general TEM preparatory procedure is as follows:

1. Fixation by vital perfusion or post-mortem immersion.

2. Second fixation by osmium tetroxide.
3. Rinse, dehydrate in alcohol, and embed in resin.
4. Section, mount on grid, and stain.

Artefacts are often introduced in the micrograph when fixation is performed incorrectly. Even in properly prepared specimens, tissue shrinkage is known to occur. The artefacts are factitious structures and must be identified or incorrect anatomical descriptions will be made. An example of a transmission electron micrograph is given in Figure 5. These micrographs tend to have a two-dimensional appearance which can occlude anatomical details.

The general SEM preparatory procedure is as follows:

1. Fixation similar to that used in TEM.
2. Rinse
3. Critical-point drying or freeze-drying.
4. Mounting to specimen holders.
5. Coating by vacuum evaporator or diode sputter coater.

The resulting micrographs have a three-dimensional appearance as in Figure 6. Since the fixation procedures are similar to those used in TEM, artefacts can also be introduced in SEM. The large blebs of the scanning electron micrograph of Figure 7 are thought to be artefacts of the fixation procedure (Pickles, 1985). Obviously such large factitious structures can lead to incorrect modeling. Another problem in determining ultrastructural morphology from SEM is an added variable dimension from the coating used in step 5 above. Also, fixation shrinkage can reduce approximately 10% of the diameter of the stereocilia (E. H. Peterson, personal communications). It can also obstruct filamentous structures in the specimen. In order to minimize errors in characterizing ultrastructural anatomy, both TEM and SEM should be used.

1.1.2 Stereocilia Ultrastructural Anatomy And Physiology

The stereocilium is comprised of a core of parallel, cross-linked filaments surrounded by a thin membrane as in Figure 8 (Tilney et al., 1983). The arrows in Figure 8 indicate transverse striations, possible cross-bridges, between the filaments. The filaments have been shown to be the protein actin in its polymerized form (F-actin)

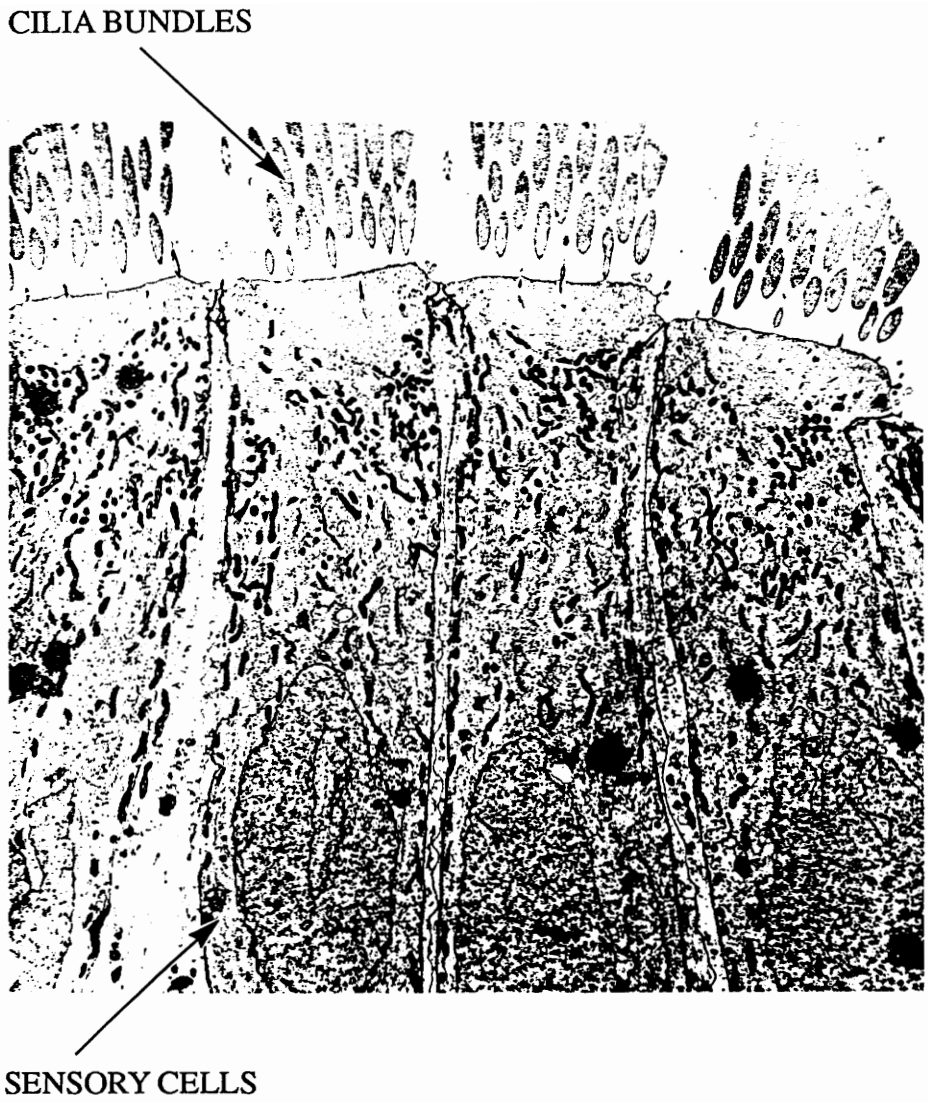

Figure 5. Example of a transmission electron micrograph (TEM) (Friedmann and Ballantyne, 1984).

This TEM example is of the apical portions of the hair cells and supporting cells in the lizard basilar papilla (hearing organ). The good contrast is due to the fixative technique. Note the 2-D nature of the micrograph.

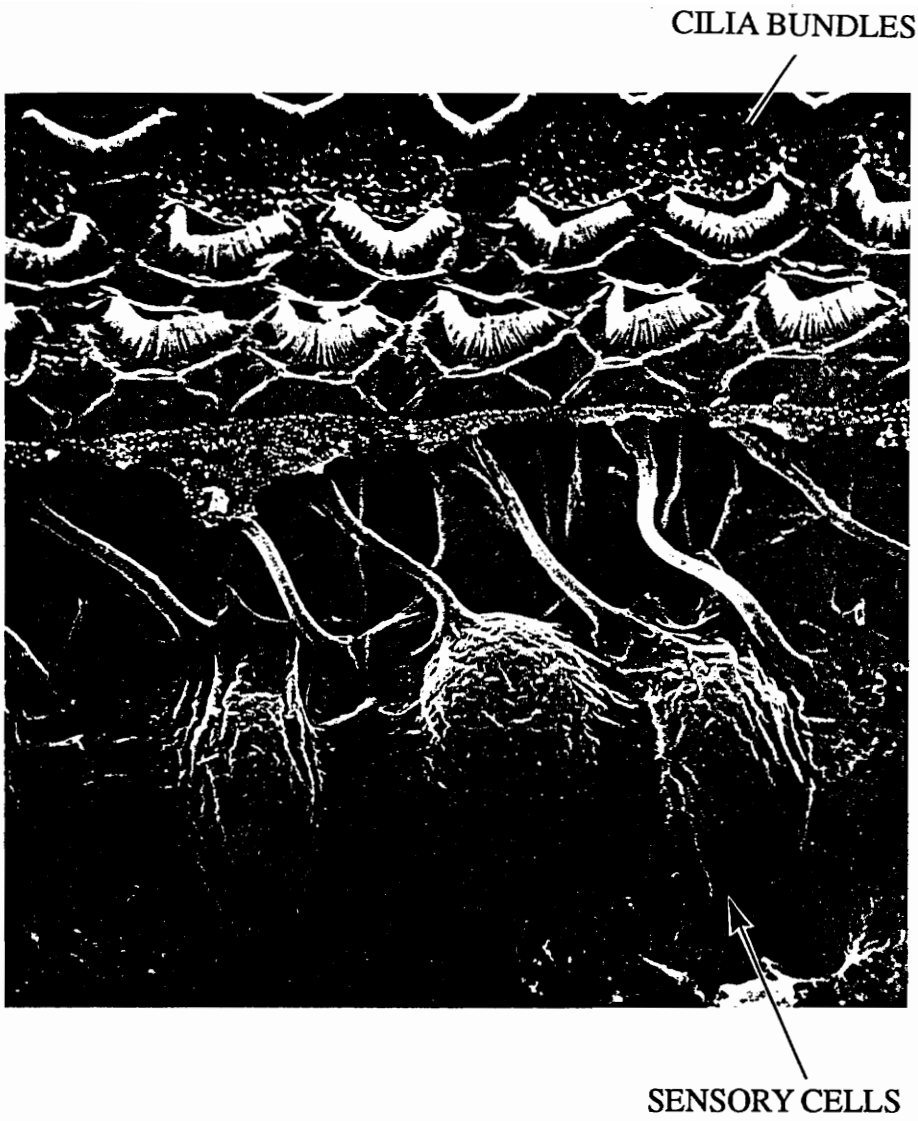

Figure 6. Example of a scanning electron micrograph (SEM) (Friedmann and Ballantyne, 1984).

This SEM example is of the guinea-pig organ of Corti outer hair cells. Note the 3-D nature of the micrograph.

Figure 7. Example of SEM artefacts introduced by the method of fixation (Pickles, 1985).

The arrows mark horizontal links connecting adjacent stereocilia of an inner hair cell of the guinea-pig cochlea. These links shown at a greater magnification in the inset are presumably real structures, while the large blebs on the stereocilia are thought to be artefacts due to fixative techniques. Scale bars: 100 nm.

(Pickles, 1985). Thus, they are similar to microvilli (small cylindrical protrusions most often found in the small intestine) in that they do not contain microtubules, or small cylindrical structures within the surrounding membrane. Kinocilia, however, are true cilia in that they do contain an array of microtubules (Pickles, 1985). Actin is presumably the primary structural component of stereocilia although other cytoskeletal proteins, such as myosin, have been identified in the stereocilia. The presence of actin and myosin, which are both present in muscle and have been identified with cell motility, suggest possible active control of stereocilia mechanical properties (Pickles, 1985).

The mechanical properties of the stereocilia depend on two factors. One is the mechanical properties of the stereocilia's filamentous constituents, namely actin. The second is the degree and nature of cross-linking between the filaments. An investigation into the bird cochlea by Tilney et al. (1983) revealed the deformation behavior of the cross-bridges. Figure 9 from their results shows two possible modes of deformation of a three filament model. In Figure 9b the filaments are bent requiring the cross-bridges to remain perpendicular to the long axis of the filaments. This mode would result in stretching the left filament and compressing the right filament. The resulting condition resembles the plane-sections-remain-plane assumption in mechanics of materials. In Figure 9c the filaments are allowed to slip relative to one another such that the cross-bridges remain parallel to one another. Thus, no stretching or compressing of the filaments takes place. The TEM micrograph of Figure 9d shows that the actual deformation behavior of a stereocilium resembles that of Figure 9c and not Figure 9b. Therefore, the actin filaments must slide relative to one another in bending. This slippage would seem to indicate that the filaments are not tightly cross-linked. This conclusion is consistent with other studies on the deformation behavior of stereocilia (Howard and Ashmore, 1986). For most of the analyses in this paper, the Young's modulus for actin has been applied to the entire stereocilia. The Young's modulus for actin, comparable to that of tubulin, is taken to be 3×10^9 N/m^2 (Howard and Ashmore, 1986). The Poisson's ratio, ν, is 0.4 which is consistent with nearly incompressible solids.

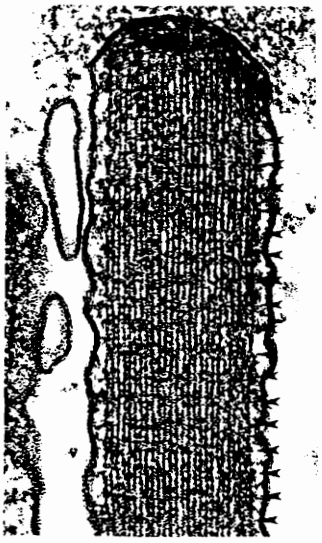

Figure 8. Actin filaments shown in stereocilium cross-section (Tilney et al., 1983).

This longitudinal section through the tip of a bird cochlea stereocilium shows the long, parallel filaments of actin running along the stereocilium. The arrows mark periodic bands assumed to be cross-bridges.

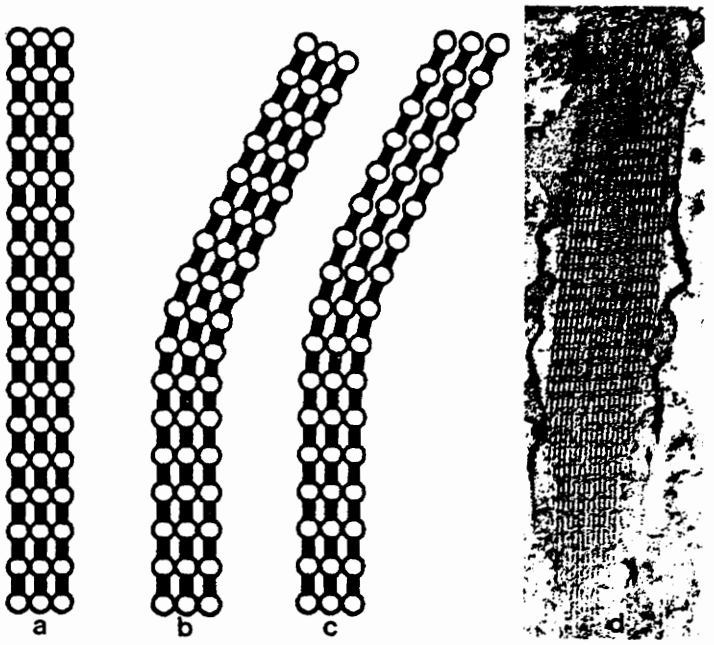

Figure 9. Actin cross-bridges and their relationship to stereocilia bending behavior (Tilney et al., 1983).

(a) Illustration of three filaments with circles representing cross-bridge points. (b) Illustration of one possible configuration in bending. The cross-bridges remain perpendicular to the filaments resembling the plane-sections-remain-plane assumption in mechanics of materials. (c) Illustration of another possible configuration in bending. The cross-bridges no longer remain perpendicular to the filaments, but parallel to each other. (d) Thin section of a bent stereocilium. Notice that the bent stereocilium in (d) fits the configuration in (c), not (b). Thus, the filaments are free to slide past one another in bending.

Dimensional data for hair cell stereocilia are extremely varied from species to species and also depending on location within the inner ear (see various micrographs in Friedmann and Ballantyne, 1984). For preliminary models, I have taken values reported for stereocilia in the sacculus of the frog (Howard and Ashmore, 1986). The actin core radii is 180 nm in the upper region of the stereocilia and 60 nm at the point of insertion into the cuticular plate. The height of the taper at the base of the stereocilia is 1 μm, while the average overall height of the stereocilia is 10 μm.

A dense bundle of actin microfilaments form a rootlet at the proximal end of the stereocilia. Proximal will refer to the point of attachment of a structure, whereas distal will refer to a region far from the point of attachment. This rootlet extends from the stereocilium into the cuticular plate at the apical portion, or apex, of the sensory cell as in Figure 10. The cuticular plate consists of actin filaments from these rootlets, the actin-binding protein spectrin, and tropomyosin (Tilney et al., 1992). The connection of stereocilia to cuticular plate is extremely rigid such that the stereocilia are usually modeled as cantilevered beams.

1.1.3 Stereocilia Bundle Interconnections

The bundles of cilia found atop the hair cells of the inner ear are composed of anywhere from tens to thousands to tens of thousands of stereocilia. Vestibular bundles have been categorized into two types: loose and tight (Bagger-Sjoback and Takumida, 1988) as in Figure 11. In the hearing apparatus cochlear outer hair cells seem to be packed in a V- or W-shaped array, while inner hair cells are arranged in nearly straight rows. With each progressing row in any arrangement, the stereocilia ascend in height in a staircase, or pipe-organ, fashion. The stereocilia lean in on one another such that their axes are convergent (Pickles, 1985). Their morphological characteristics depend on species and location. The illustration of Figure 11 also shows the three types of interconnections which have been identified (Furness and Hackney, 1985). These interconnections are (1) between the tips of the stereocilia of one row to the sides of the stereocilia in the next taller

Figure 10. Rootlet anchoring the base of a stereocilium to the cuticular plate (Tilney et al., 1983).

This longitudinal section cut through the base of a stereocilium clearly identifies the electron dense structure known as the rootlet. The rootlet is formed by the terminal actin filaments at the base of the stereocilium.

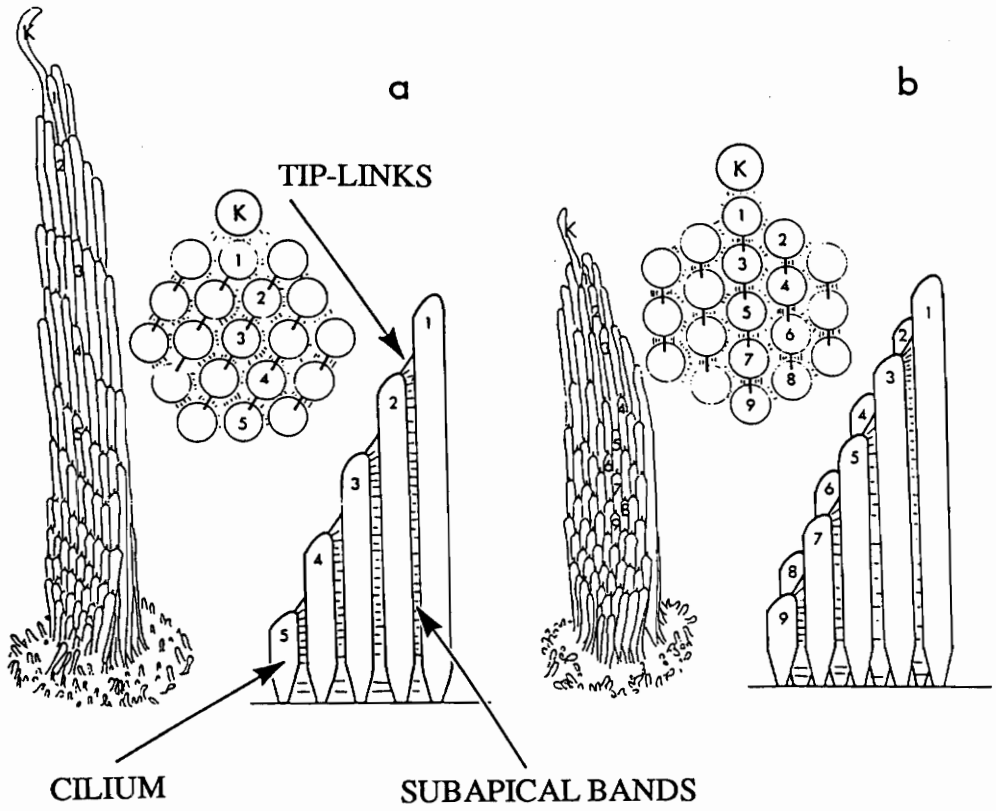

Figure 11. Two hair bundle types (Bagger-Sjoback and Takumida, 1988).
(a) The 'tight' hair bundle type consists of parallel transverse rows of stereocilia. (b) The 'loose' hair bundle type consists of longitudinal rows of stereocilia. Assumed hexagonal arrangements are illustrated for each bundle type with the numbers representing different stereocilia rows. Tip-links are shown in each bundle as well as bands of interconnecting links along the entire length of the stereocilium. Many investigators show these later links to occur only at the upper regions of the stereocilia (known as subapical bands).

row (tip-links), (2) between the stereocilia of adjacent rows (row-to-row bands), and (3) between the stereocilia of the same row (side-to-side bands).

The tip-links have been found at various orientations (see micrographs in Furness and Hackney, 1985; Pickles, 1985). The variety in orientation angle could be a result of functional differences between hair cells, or they could simply be artefacts of the microscopy techniques. The diameter of the tip-links has been given ranging from 5 nm (Pickles, 1985) to 6 nm (Bagger-Sjoback and Takumida, 1988). The tip-link is composed of a core of filamentous material surrounded by a membrane (Osborne et al., 1988). The filament material has not been identified. Thus, this paper will initially assume its mechanical properties to be that of actin. Some experiments (Howard and Hudspeth, 1988) have determined the Young's modulus of the tip-links to be approximately 4 MPa. This value was arrived at by making many assumptions about the mechanical properties of the stereocilia bundle and stiffness behavior. It has not been confirmed by any other literature, thus it will not be used initially in this paper. Later models will however explore the effects of moduli in this range.

The row-to-row and side-to-side links are bands of fine filaments running parallel to the cuticular plate. Figure 11 illustrates these links as occurring along the entire length of the stereocilia. Some micrographs support this conception, yet many investigators have evidence that these links occur mainly in the apical regions of the bundle as shown in Figure 7 (Pickles, 1985; Furness and Hackney, 1985). The side-to-side links are expected to mechanically couple stereocilia of the same row. If an applied force or deflection is assumed to be uniformly distributed along the entire row, these links would not contribute to the stiffness of the bundle. This assumption will be used in this work. The row-to-row links would then serve, as do the tip-links, as a mechanism for transmitting deformation from one row to another. There are no available dimensional or mechanical properties for these links in the literature. They will be assumed to have the same properties of the tip-links. These links are not constrained rotationally, thus they remain parallel to the cuticular plate during deflection.

1.1.4 Mechanoelectrical Transduction

Mechanoelectrical transduction in hair cells was experimentally reproduced by Hudspeth and Corey (1977; 1979). Their experiments showed that hair cells depolarize when the stereocilia of the bull frog sacculus were deflected towards the kinocilium, the direction of neural excitation. Later experiments by Hudspeth and Corey quantified cilia displacement effects on the electrical activity across the cell membrane (Pickles, 1985). The resulting curve was an asymmetrically saturating relationship between displacement and current flow. Deflection in the excitatory direction produced a gradually saturating current flow for deflections greater than 0.7 μm. Deflection in the opposite direction saturated at approximately 0.1 μm and at low currents. Thus, deflection away from the kinocilium is termed the inhibitory direction.

The transduction process begins with deflection of the sensory cilia in the direction of the tallest stereocilium, or kinocilium if it is present. Deflection is a result of excitation from surrounding media (gel or fluid) under the action of acoustic, gravitational, or accelerative stimulus. The resulting stress conditions open transduction channels allowing high ionic concentrations to flood into the sensory cell. The increased ionic concentration in the sensory cell causes the cell to depolarize, increasing the electrical activity across the cell membrane from cell to nerve. A neutral ionic state is observed in the opposite direction, resulting in hyperpolarization of the cell. The process of increasing and decreasing the polarization of the cell results in a release of neural transmitters at the nerve synapse. These neural transmitters in turn change the nerve distal synapse polarization which triggers a spike encoder located in this region. This spike encoder sets up a spike train where frequency is proportional to polarization, and this frequency information is sent to the central nervous system. Isolated deflection of the kinocilium results in no potential changes in the hair cell (Pickles, 1985).

Many experiments have been performed in order to locate the transduction channels in the stereocilia. Fluorescence imaging by Ohmori (1988) indicated the influx of Ca^{2+} or Mn^{2+} ions presumably into transduction channels. These experiments

suggested the point of stereocilia insertion into the cuticular plate as the site for the channels. However, overwhelming evidence from calcium imaging and immunolabelling experiments (Hackney et al., 1991; Hackney et al., 1992; Pickles and Corey, 1992) have localized the channels to occur near the tips of the stereocilia. Extracellular field potential experiments by Hudspeth (1982) demonstrated that current flow was greatest at the tips of the stereocilia seeming to confirm this location for the transduction channels.

If the tips of the stereocilia are indeed the locations for the transduction channels, it is no surprise to find specialized structures there, namely the tip-links and subapical bands. Both structures could be associated with the opening and closing of the transduction channels. A simple gating-spring model has been proposed for the opening and closing of the channels. The tension/compression action of the spring opens/closes the gate to the channel controlling the influx of ions. Both the tip-links and subapical bands could act as this spring. The amiloride immunolabelling performed by Hackney et al. (1991; 1992) suggests that the channels are actually at the subapical bands and not at either end of the tip-links. Although inconsistent with these findings, the predominant model in the literature is the tip-link hypothesis, where the tip-link is the gating-spring (Pickles, 1985).

1.2 RELEVANCE AND MOTIVATION

The anatomy and physiology review of the previous section has identified inner ear hair cells as the sites of mechanoelectrical transduction from a mechanical event (e.g. acoustics, acceleration) to an electrical event (e.g. nerve impulse response in the central nervous system, or CNS). The block diagram of Figure 12 illustrates the overall hair cell transduction process from mechanical input stimulus to electrical output to the CNS with specific reference to the relevance of ciliary bundle structure, stiffness, and deflection.

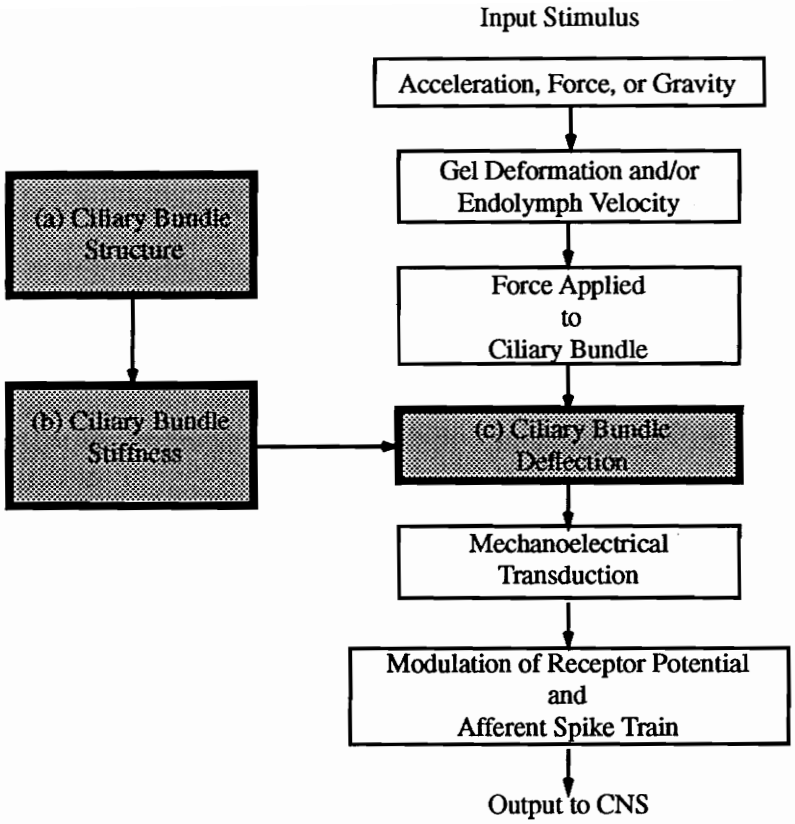

Figure 12: Block diagram of the mechanoelectrical transduction process (Duncan and Grant, 1993). The shaded blocks indicate the subjects covered in this paper.

The deflection (c) by surrounding media of stereocilia bundles plays a key role in the transduction process. Bundle stiffness (b) resulting from the ciliary bundle structure (a) controls deflection and thus the fundamental sensitivity of the mechanoelectrical transduction process. So far, the study of sensory hair bundle stiffness has been limited to experimental analysis and simple mathematical models.

One method for the experimental determination of bundle stiffness (defined as the force required for a 1 μm displacement) was to push, or pull, the bundle with a probe of known compliance (Strelioff and Flock, 1984; Crawford and Fettiplace, 1985; Howard and Ashmore, 1986). Residual movements of the probes, assumptions in optical

correction factors, possible probe nonlinearities, and possible cell deterioration can all introduce significant error into the stiffness analysis. Another study used water jet excitation and optical imaging to determine bundle stiffness (Szymko et al., 1992). The water jet force was calibrated using a fiberglass probe of known compliance and then applied to a sample hair cell. Optical imaging allowed displacement to be measured and the stiffness to be determined. This technique also could introduce significant error in the force correction factor between probe and cell bundle and in possible fluctuations in the applied force. Average values obtained from many of these experiments are given in Table 1 (Szymko et al., 1992). These experimental values range over two orders of magnitude probably indicating the variability of stiffness in these structures.

TABLE 1: Experimental Stiffness Values

INVESTIGATOR	STIFFNESS ($\times 10^{-4}$ N/m)	HAIR CELL ORGAN
Ashmore (1984)	1.32	frog sacculus
Flock and Strelioff (1984)	7.8 to 34.7	guinea pig cochlea
Strelioff and Flock (1984)	1 to 97.2	guinea pig cochlea
Crawford and Fettiplace (1985)	6	turtle cochlea
Howard and Ashmore (1986)	2.56	frog sacculus
Howard and Hudspeth (1987)	6.3	bullfrog sacculus
Denk, Webb, and Hudspeth (1989)	3.41	frog sacculus
Russell, Richardson, and Kossl (1989)	16 to 35	mouse cochlea
Szymko, Dimitri, and Saunders (1992)	5.04	chick cochlea

Stiffness experiments have also been performed in the study of the mechanoelectrical transduction process. Howard and Hudspeth (1988) used several experiments on bullfrog sacculus hair cells to determine the compliance of the hair bundle associated with the gating of mechanoelectrical transduction. The results would presumably indicate the possibility of the tip-link as the gating-spring mechanism. In their analysis a major assumption was made concerning the linearity of stiffness terms predicting overall bundle stiffness. There was no previous physiologic or mathematical

evidence indicating the accuracy of assuming bundle stiffness as the sum of bundle components (e.g. stereocilia pivotal stiffness, transduction channel compliance, gating-spring stiffness). Indeed, basic mechanics of materials would seem to contradict such an assumption. Also, there is presently no method of verifying this model experimentally. Other methods must be used in determining bundle stiffness and the stiffness contributions of individual bundle components.

The dawning of high-powered, high-speed computational software has paved the way for biomedical modeling. Modeling has the advantages of reducing experimental error, eliminating the animals required for experimentation, and simulating conditions impossible in experimentation. While modeling should not be relied upon solely, it offers unique possibilities in the study and confirmation of physiologic function. An accurate model of the behavior of inner ear hair cells can confirm experimental mechanics studies and be used to study the cells of high-order mammals unavailable for experimentation. Models can also be used to understand physical abnormalities associated with inner ear hair cells such as deafness, spatial disorientation, equilibrium and hearing deterioration with age, and zero-gravity effects. Therefore, accurate mathematical and computational models of inner ear hair cells are not only needed but necessary in fully understanding hair cell mechanics.

1.3 OBJECTIVES

The objectives of this research are as follows:

- To adequately characterize the experimentally determined deformation behavior of inner ear hair bundles.
- To identify the contributions of individual bundle components to the overall bundle stiffness.
- To perform a parametric study of stiffness changes with individual structure moduli, size, orientation, and location.

- To determine any nonlinear components in overall bundle stiffness.
- To determine the feasibility of linear versus nonlinear constitutive equations in characterizing bundle deformation.
- To study any differences in inhibitory versus excitatory stiffnesses.
- To perform preliminary dynamic analyses to obtain model natural frequencies.

Additionally, this research will elucidate the deficiencies in available anatomical and physiological data, will provide the path for future study, and may provide insight into the mechanisms for transduction.

1.4 OVERVIEW

The following chapter (Chapter 2) will provide the foundations for solving analytical mathematical models and computational finite-element models. This chapter will also review the computational software and algorithms used in the analyses. Chapter 3 includes the stiffness results and parametric study of a single stereocilium and will describe the process in constructing the bundle finite-element model. The stiffness effects of the subapical bands, tip-links, and bundle geometry will be discussed in Chapter 4 followed by nonlinear analyses in Chapter 5. Chapter 6 will concluded the analysis by presenting preliminary dynamic results used to obtain natural (undamped) frequencies. It should be noted that the order of presentation in this paper does not follow the order of accomplishment of the actual research. Restructuring and problem reformulation was a frequent occurrence. Chapter 7 will present a summary and conclusions, while Chapter 8 contains suggestions for future work.

2.0 METHODOLOGY

Biomedical modeling poses unique problems to the engineer. Some of these were discussed in Chapter 1 (e.g. TEM and SEM artefacts, species and location dependent data, inability to determine material properties). Basic model assumptions will include: isotropic, linear elastic materials with circular cross-sections. All stereocilia in a single row will be assumed to be forced equally such that the side-to-side subapical bands will play no role in resisting deflection (i.e. no contribution to bundle stiffness). Therefore our models will assume that the bending of a single stereocilium at a specific height will characterize the bending behavior of its entire row. This assumption is most useful when considering the nearly straight rows of the cochlear inner hair cells, while it is less valid for cochlear outer hair cells and vestibular hair cells. Another major assumption in this work is that all stereocilia are parallel, in the undeformed state, although they have recently been shown to have convergent axes (Pickles, 1985).

Before discussing the implementation of these assumptions into analytical and computational models, we must first fully define the term "bundle stiffness".

2.1 OVERALL BUNDLE STIFFNESS

Bundle stiffness k is defined as the force F required to produce a unit deflection of the tallest stereocilium, or $k=F/\delta$, where δ is the bundle deflection in the plane of increasing stereocilia height and F is applied to the tallest stereocilium. This concept is illustrated in Figure 13. The term stiffness will be used in this paper to refer to resistance to deflection in the excitatory direction (Figure 13) unless otherwise noted as inhibitory stiffness. Inhibitory stiffness will be defined in a similar manner as excitatory stiffness yet with the deflection being in the opposite, or inhibitory, direction. These definitions for stiffness are consistent with those used by the experimental researchers sited previously (Chapter 1).

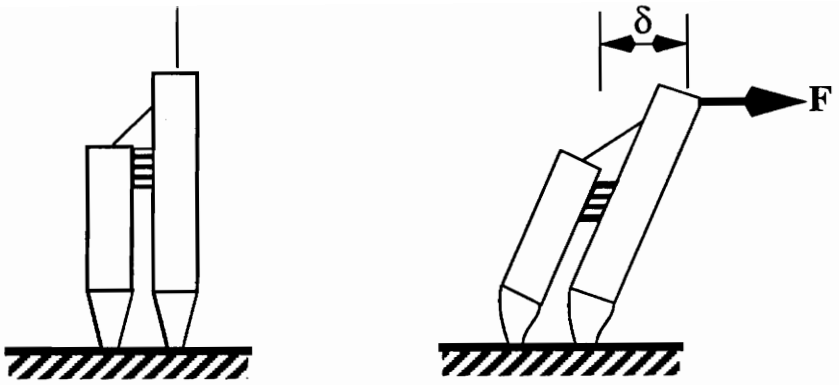

Figure 13: Overall bundle stiffness diagram defining stiffness K as the force F required to produce a unit deflection of the tallest stereocilium (Duncan and Grant, 1993). δ = the lateral bundle deflection and F = applied force.

2.2 ANALYTICAL MODELING TECHNIQUES

Analytical solutions were obtained for the bending of a single stereocilium so that this basic building-block of the overall structure was well understood. Elasticity problems can often be solved analytically to obtain closed-form solutions. Closed-form solutions were sought in order to (1) characterize the bending behavior of a single stereocilium, (2) obtain stiffness data for various dimensions and moduli, and (3) validate future computational approximations.

Castigliano's theorem on deflections will be used in the analysis. This method is based on the concept of complementary energy and expressed in terms of total strain energy. Total strain energy is defined as the integral of the strain energy density over the structure volume. Limitations to this method are linear elastic material behavior, small displacements, and plane sections must remain plane. Under these assumptions the complementary energy and total strain energy are equal. The resulting equations relating deflection and applied force will be developed in the following chapter. These equations will enable the determination of stiffness in terms of stereocilium geometry and material properties.

The integration of strain energy density can be very complex. In these cases, MATHEMATICA v1.2 was used for the integrations. In all cases the integrations were exact; they did not require algorithms for numerical solutions. MATHEMATICA was also used for displaying surface plots of the output. In this manner, the dependent variable, stiffness, could be plotted against two independent variables (i.e. two radii or two heights).

2.3 FINITE-ELEMENT METHOD

The complexity of the bundle structure requires the use of finite-element analysis (FEA). FEA enables the problem to be broken into discrete, coupled components that approximate the continuum description. These components, or elements, are represented by a linear combination of piecewise polynomial functions. The functions, along with prescribed boundary conditions, are then used to solve the governing equations. The values of the solution are found at preselected points called nodes located on the boundary or in the interior of an element. Three inherent sources of error in FEA are: (1) the approximation of the structure geometry, (2) the approximation of the solution, and (3) error due to computational approximations (Reddy, 1984). After describing the computational workstations, this discussion will introduce the types of elements used in the analysis, describe how these elements form a finite-element model (preprocessing), and present the method of analysis.

2.3.1 Computational Tools

UNIX-based Apollo and RISC workstations were used for the finite-element analysis. PATRAN v2.5 was used for the pre-processor model description and post-process analysis. ABAQUS v4.9.1 and v5.2 were used to analyze the various geometries and load cases.

2.3.2 Element Types

Many of the errors in FEA are a direct result of the chosen element type. Therefore, a discussion of the elements used in this work is essential when considering model validity. Figure 14 illustrates the four types of elements used in this paper: beam,

wedge, hexagonal, and spring. The beam elements are 2 or 3 node elements depending on the order of interpolation desired, whether cubic or quintic, respectively. These elements are most often used for small strain, large rotation analysis (ABAQUS manual, 1989). This means that element elongation is small compared to the original length. Therefore, this element is ideal for modeling bending of uniformly cross-sectioned members. Beam elements must be given material properties and a characteristic cross-section. Each node of a beam element has six degrees of freedom: three translational and three rotational.

The wedge and hexagonal elements are three-dimensional elements with quadratic interpolation along the element edges and no interior nodes. Therefore, the wedge elements have 15 nodes, and the hexagonal elements have 20 nodes. Care must be taken in finite-element discretization such that neighboring elements with coincident element edges have the same number of nodes (same order of interpolation) and that they too are coincident. For example, one such coincident element edge cannot be described by both linear and quadratic interpolating polynomials. Wedge and hexagonal elements must be given characteristic material properties, although no additional geometric properties need be assigned. Each node has three translational degrees of freedom only.

The spring elements were used in this paper to model stereocilia interconnections (e.g. tip-links and subapical bands). These elements describe the force-displacement behavior between two nodes and, therefore, are prescribed a characteristic stiffness. Spring stiffness values were determined from basic mechanics of materials formulas developed in the next chapter. The elements have three translational degrees of freedom only. The force in the spring acts along the line of action between the two nodes. This line of action remains constant, or in the same direction, in linear analysis, but in large deformation theory the line may rotate, remaining between the displaced nodes.

2.3.3 Preprocessing Considerations

Two- and three-dimensional model descriptions were used in modeling the hair bundle stereocilia. In each case, model length units were scaled by 10^6 such that 1 length unit was equal to 1 micrometer. In the 2-D cases, general beam elements were used with

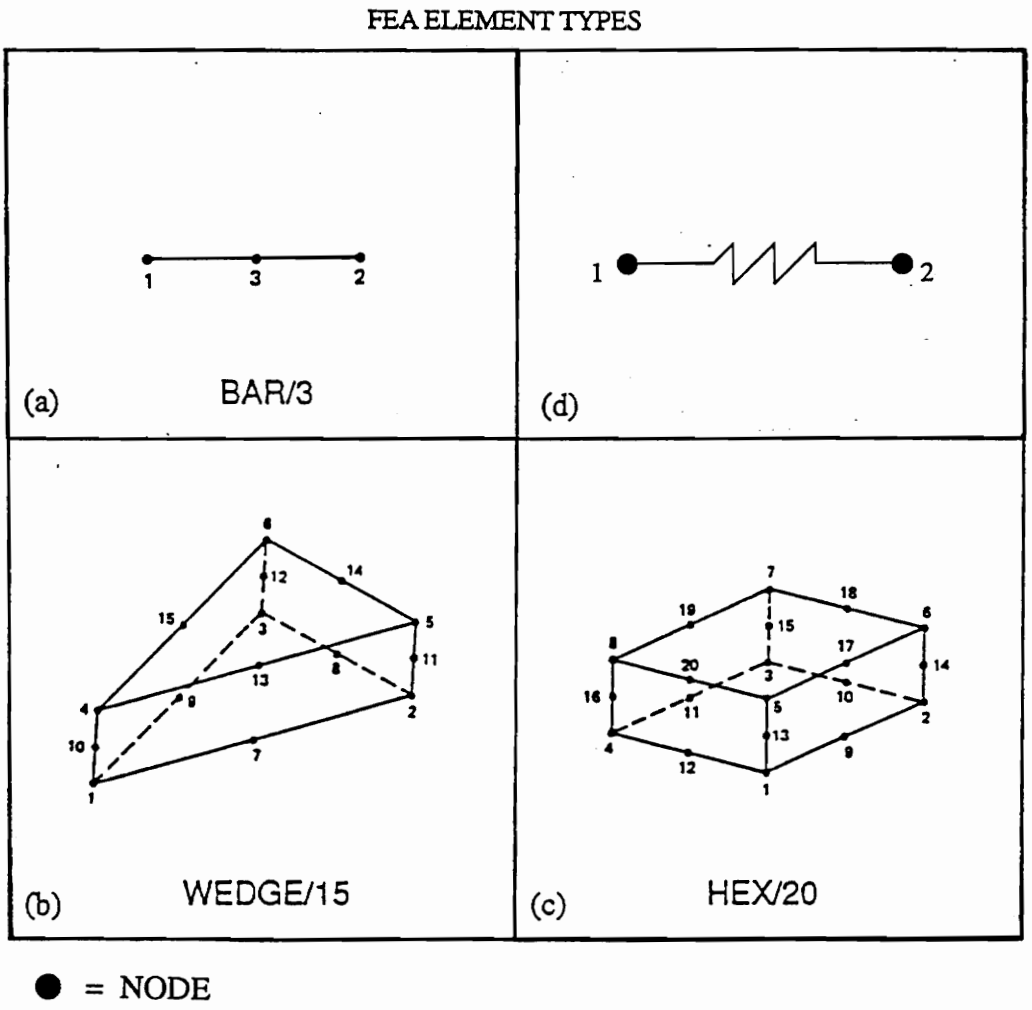

Figure 14. Illustration of element types used in FEA models (PATRAN Manuals, 1990). (a) 3-node beam element. (b) 15-node wedge element. (c) 20-node hexagonal element. (d) 2-node spring element.

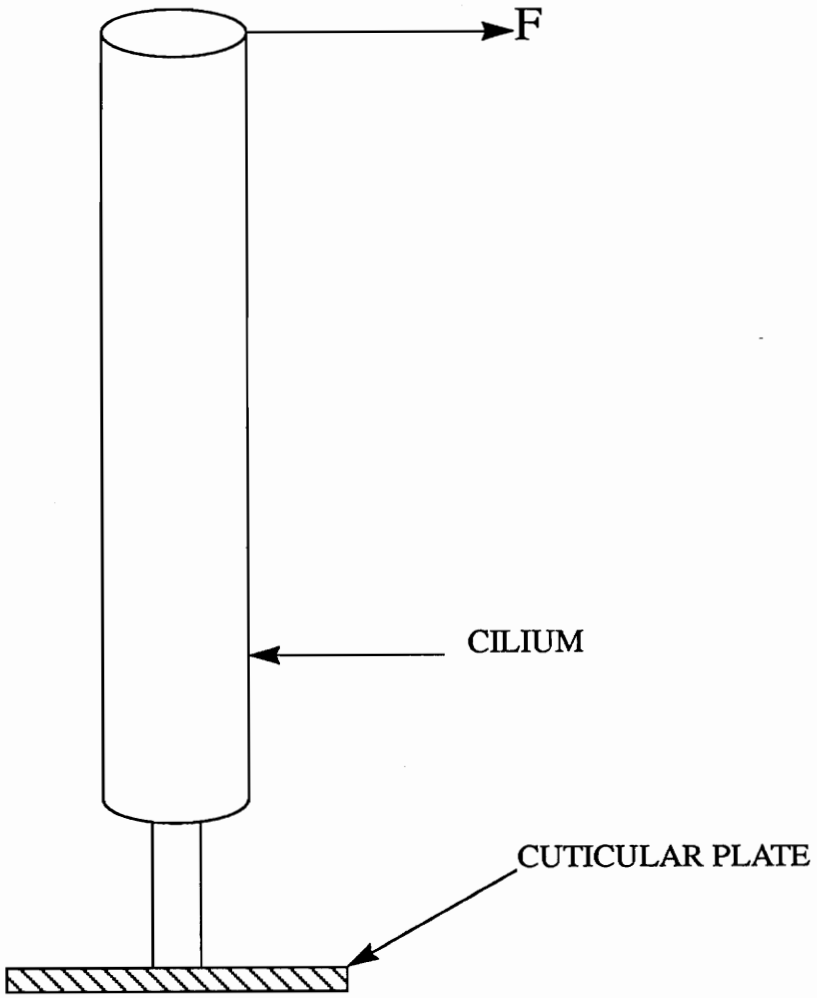

Figure 15. Illustration of stepped cross-section model.

The stepped cross-section assumption simplifies the tapered base by a uniform cylinder with a diameter equal to the diameter of the stereocilium at the point of insertion into the cuticular plate. The cuticular plate is modeled as a rigid structure such that the stereocilium is cantilevered.

circular cross-sections. Each 2- or 3-node element was given a characteristic radius, Young's modulus, and Poisson's ratio. ABAQUS internally calculated the cross-sectional area and moments of inertia from the given radii. A stepped cross-section was used to approximate the gradual tapering that actually occurs over 1 μm at the stereocilia base as shown in Figure 15. The base node of each stereocilia was translationally and rotationally constrained such that the beam was cantilevered. The force was applied to the top node of the stereocilia in order to cause deflection and, therefore, determine stiffness.

In the 3-D cases, cylinder and cone geometries were used to better approximate the tapering at the base of the stereocilia. Discretizing, or meshing, a 3-D structure is much more difficult than that for a 2-D one. Three-dimensional geometric entities called hyperpatches were drawn in PATRAN to form the cylinder and cone shape of the stereocilia. The circular cross-section of the hyperpatches was easily approximated by the sector cross-section of the wedge elements as shown in Figure 16. The quadratic interpolating polynomials could accurately describe the curved nature of the circular cross-section. As in the 2-D cases, the base of the stereocilia was cantilevered (remember that 3-D elements have translational degrees of freedom only) and the force was applied to a node at the top of the stereocilia along the line of symmetry so no torsion was applied.

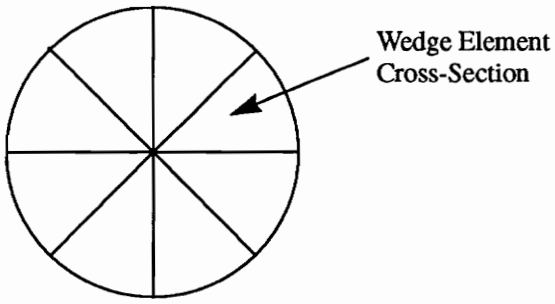

Figure 16: Hyperpatch circular cross-section divided into eight pieces, each representing a wedge element cross-section.

2.3.4 Method Of Analysis

The conversion program PATABA was used to translate the PATRAN preprocess geometry description into an ABAQUS input file. This input file includes element definitions, node connectivity, material property data, load history, and postprocessing information. The deformation theory to be used and results variables to be reported were also declared in PATABA for translation. The results variables reported were displacement for each node in the direction of the three global axes and in some cases the force in the spring elements. The deformation theory that was used was either static-linear for small displacements or static-nonlinear for large displacements. A modified Newton's method is generally used by ABAQUS for the solution of nonlinear equilibrium equations. It is an incremental technique that iterates for a convergent solution at each small load increment. Many factors determine solvability and solution time in large deformation analysis such as number of increments, number of iterations, force and moment tolerances, and the positive definiteness of the system matrix.

Displacement files for postprocessing enabled the determination of overall bundle stiffness and the graphical representation of stereocilia deformation. The graphical output and computed stiffness could then be compared with experimental observations.

3.0 MODEL FORMULATION

Analytical and computational models are effective if they are simple, yet accurate. Therefore, modeling often begins with over-simplified structures which get progressively more complex. This chapter will describe models for the deformation behavior of a single stereocilium and will determine the best method for modeling the stereocilia bundle interconnections. The analytic solutions will determine the reliability of the finite-element technique and suggest dimensions on which to base later finite-element models. Before presenting the results, the energy method equations must be developed.

3.1 ENERGY METHODS DISPLACEMENT EQUATIONS

Figure 17 illustrates the model geometry for a single stereocilium. The stereocilium model has a circular cross-section which tapers at the base resembling a pencil. The parameters r_1, r_2, L_1, and L will represent the minimum radius at the base of the stereocilium, the radius of the upper uniform region, stereocilium taper height, and total stereocilium height, respectively. The force, F, is applied to the tip, or free end, of the stereocilium which is cantilevered at its base. The following table gives characteristic model material properties and typical dimensional values (unless otherwise stated in the analysis):

TABLE 2: Typical Model Parameter Values

PARAMETER	VALUE
Young's Modulus, E	3×10^9 N/m^2
Poisson's Ratio, ν	0.4
Base Radius, r_1	0.06 μm
Uniform Radius, r_2	0.18 μm
Taper Height, L_1	1.00 μm
Total Height, L	10.0 μm

The dimensional values were obtained from Howard and Ashmore (1986).

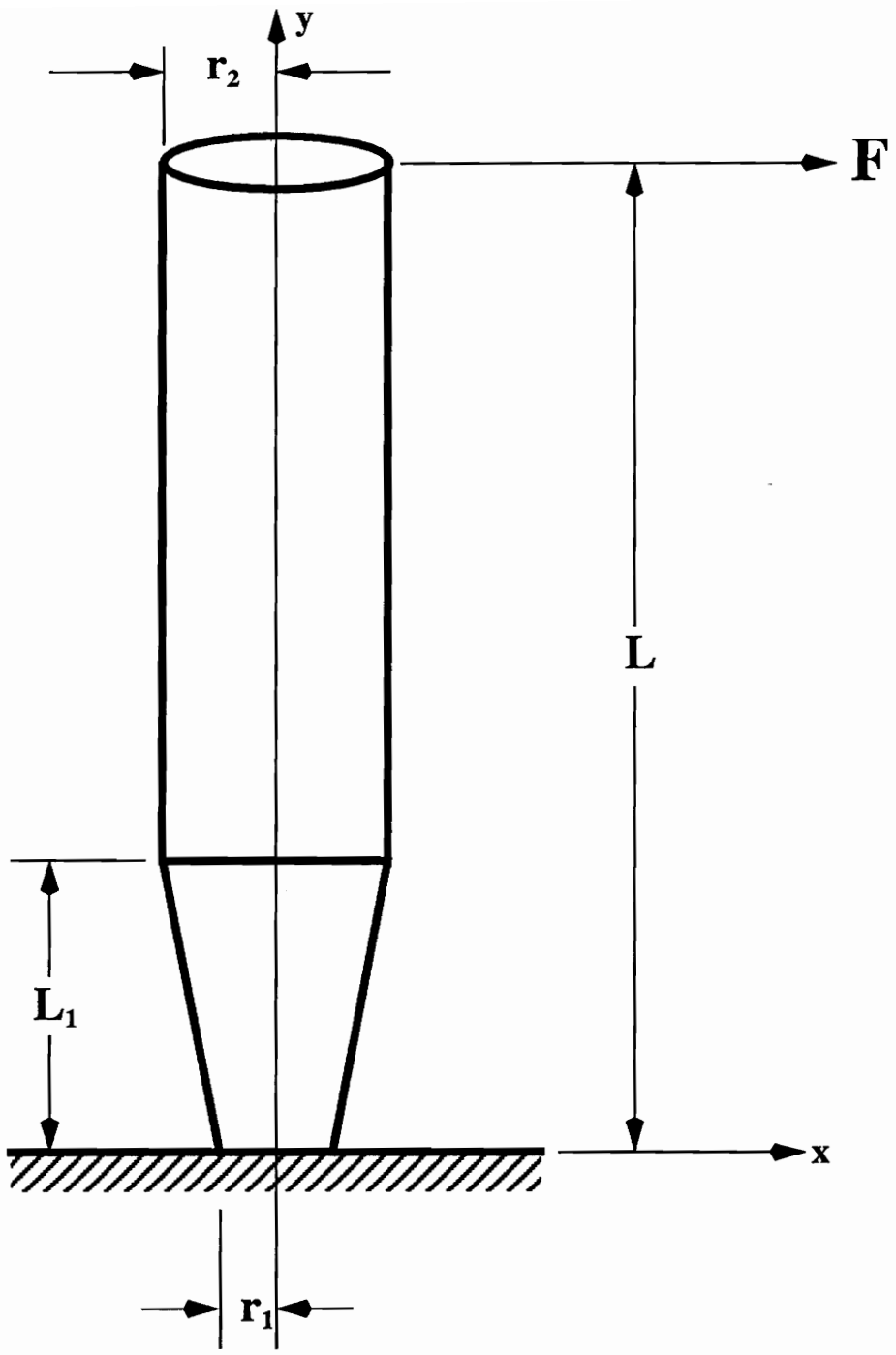

Figure 17. Dimensionalization of the solid geometric model of a single stereocilium. This illustration shows the dimensional variables used for the exact analytic (mathematical) solution and the FEA (computational) solution of single stereocilium stiffness. The x and y coordinate system is utilized in the analytic solution for stereocilium stiffness. F is the applied force causing the stereocilium to bend.

The strain energy in the case of pure bending results from bending and shear terms such as

$$U = U_B + U_S \tag{1}$$

The strain energy due to bending is given by

$$U_B = \int_0^L \frac{M^2}{2EI} dy \tag{2}$$

where M is the internal bending moment, E is the Young's modulus, and I is the area moment of inertia. The internal bending moment M at any height y (refer to Figure 17) is given by

$$M = -F(L-y) . \tag{3}$$

The strain energy due to shear is given by

$$U_S = \int_0^L \frac{kF}{GA} dy \tag{4}$$

where F is the shear force (equal to the applied load in this case), G is the shear modulus, A is the cross-sectional area, and k is a shape factor equal to 1.33 in the case of circular cross-sections. It is customary in engineering practice to neglect shear in computing strain energy when the beam is considered slender, or $d/L < 0.1$. Since the geometry variables would vary over a wide range, the shear terms were included in the analysis.

Castigliano's theorem from mechanics of materials then gives the deflection x at the top of the beam (y=L) as

$$x = \frac{\partial U}{\partial F} = \frac{\partial U_B}{\partial F} + \frac{\partial U_S}{\partial F} \tag{5}$$

Therefore, the deflection can be considered the sum of deflection due to bending and

deflection due to shear. The deflection due to bending is given by

$$x_B = \frac{\partial U_B}{\partial F} = \int_0^L \left[\frac{-M(L-y)}{EI} \right] dy \tag{6}$$

The integral for the two regions becomes

$$x_B = \int_0^{L_1} \left[\frac{F(L-y)^2}{EI_1} \right] dy + \int_{L_1}^{L} \left[\frac{F(L-y)^2}{EI_2} \right] dy \tag{7}$$

where:

$$I_1 = \frac{\pi}{4} \left[r_1 + \left(\frac{r_2 - r_1}{L_1} \right) y \right]^4 \tag{8}$$

and

$$I_2 = \frac{\pi}{4} [r_2]^4 \tag{9}$$

The deflection for the two regions due to shear is given by

$$x_S = \frac{\partial U_S}{\partial F} = \int_0^{L_1} \frac{kP}{GA_1} dy + \int_{L_1}^{L} \frac{kP}{GA_2} dy \tag{10}$$

where

$$A_1 = \pi \left[r_1 + \left(\frac{r_2 - r_1}{L_1} \right) y \right]^2 \tag{11}$$

and

$$A_2 = \pi [r_2]^2 \tag{12}$$

The total deflection for the cilium would be

$$x = x_B + x_S \tag{13}$$

The deflection expression was then integrated using MATHEMATICA. The stereocilium stiffness K was determined by the equation

$$K = \frac{F}{x} \tag{14}$$

3.2 STEPPED CROSS-SECTION MODEL

The stepped cross-section model (Figure 15) used by Howard and Ashmore (1986) is easily analyzed by mechanics of materials techniques. However, the finite-element model is useful when this model is interconnected with others. The resulting deformation of three connected stereocilia will show that this model does characterize experimentally observed bending behavior.

3.2.1 Energy Methods Results

The stepped cross-section assumption dramatically simplifies the integration of Equations 7 and 10 since I_1 and A_1 are no longer functions of the integration variable y. The new relations for these two variables are

$$I_1 = \frac{\pi}{4}[r_1]^4 \tag{15}$$

and

$$A_1 = \pi[r_1]^2 \tag{16}$$

The resulting equation for stiffness is a function of E, G, r_1, r_2, L_1, and L. Some of these parameters may be varied while others are held constant in order to determine the effect on stiffness of a certain variable over a specific range. The variables r_1, r_2, and L were varied over a range of +/- 50% of their values in Table 2. Physical data in this range has

been verified from observations of various micrographs. The taper height L_1 was varied from 0.2 to 1.0 μm according to micrograph observations. For this wide range of geometric data, the maximum error in stiffness if shear was neglected was less than 1%. Therefore, deformation due to shear was neglected for the remainder of the stepped cross-section analysis since this assumption greatly simplifies the stiffness equations. The computed value of stiffness (neglecting shear) for the data in Table 2 was 3.27×10^{-4} N/m.

If Young's modulus, E, is assumed to be constant throughout the stereocilium, a linear relationship between K_B and E can immediately be concluded from the deformation equations above. This conclusion is consistent with the assumption of a linear elastic, isotropic, homogeneous material under small deformations while neglecting the effects of shear. A linear relationship should not be concluded under different assumptions, namely during large deformations.

Figure 18 shows the variation of stiffness K with the two height parameters L_1 and L while the radius parameters are held constant ($r_1 = 0.06$ μm and $r_2 = 0.18$ μm). Stiffness decreases with an overall height increase as well as with increasing taper height. Therefore, shorter single stereocilia have a greater stiffness than do taller ones with the same radii. SEM micrographs indicate that taper height appears to decrease with decreasing overall height which compounds the increase in stiffness with equivalent radii. If taper height is assumed to be very small compared to overall height ($L_1 << L$), then the deflection equation for x simplifies to

$$x = \frac{4F}{\pi E}\left[\frac{L^3}{3r_2^4} + L^2 L_1\left(\frac{1}{r_1^4} - \frac{1}{r_2^4}\right)\right] \qquad (17)$$

This equation shows an approximate linear relationship between deflection x and taper height L_1. Figure 19 shows a comparison of stiffness versus taper height from Equations 7 and 17. The maximum error in the simplification of Equation 17 is approximately 9%.

Figure 20 shows the variation in stiffness K with the two radii parameters r_1 and r_2 while the height parameters are held constant ($L_1 = 1.0$ μm and $L = 10.0$ μm). Stiffness

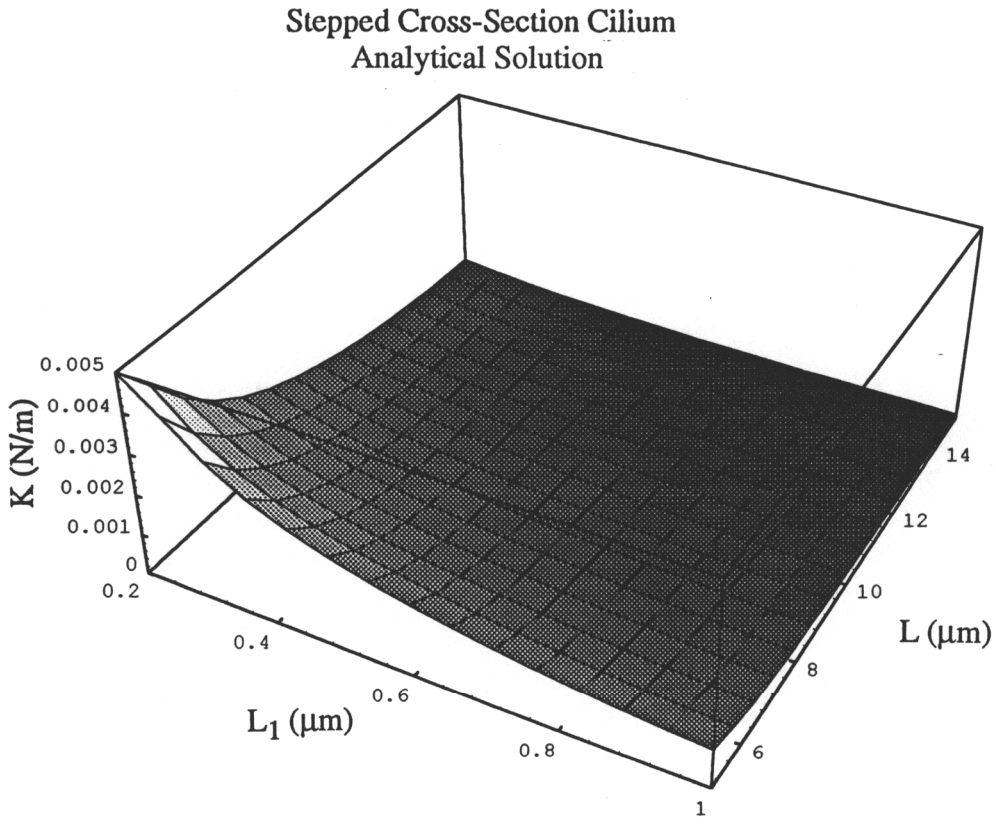

Figure 18. Stiffness versus characteristic stereocilium heights for the stepped cross-section analytical solution.
All other model parameters (i.e. stereocilium radii and Young's modulus) are held constant.

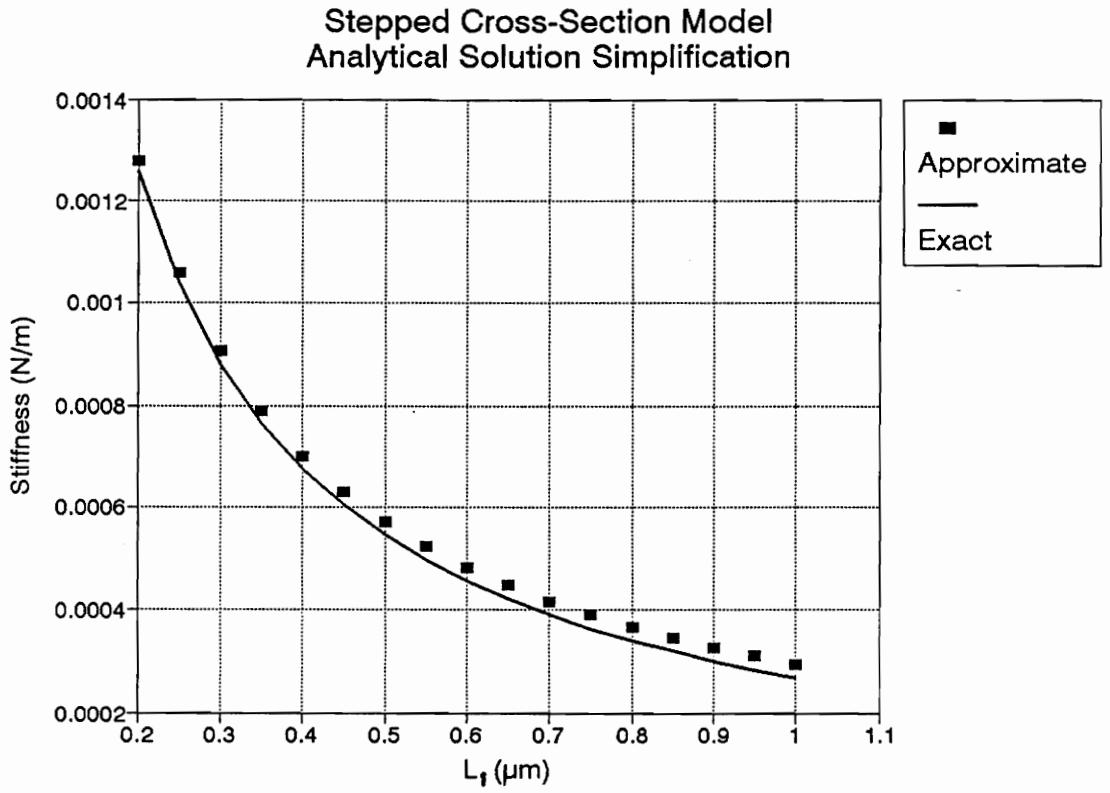

Figure 19. Stiffness versus stereocilium taper height for stepped cross-section analytical solution: a comparison of exact and approximate solutions.
All other parameters are held constant. The maximum error of the approximate solution is less than 9%.

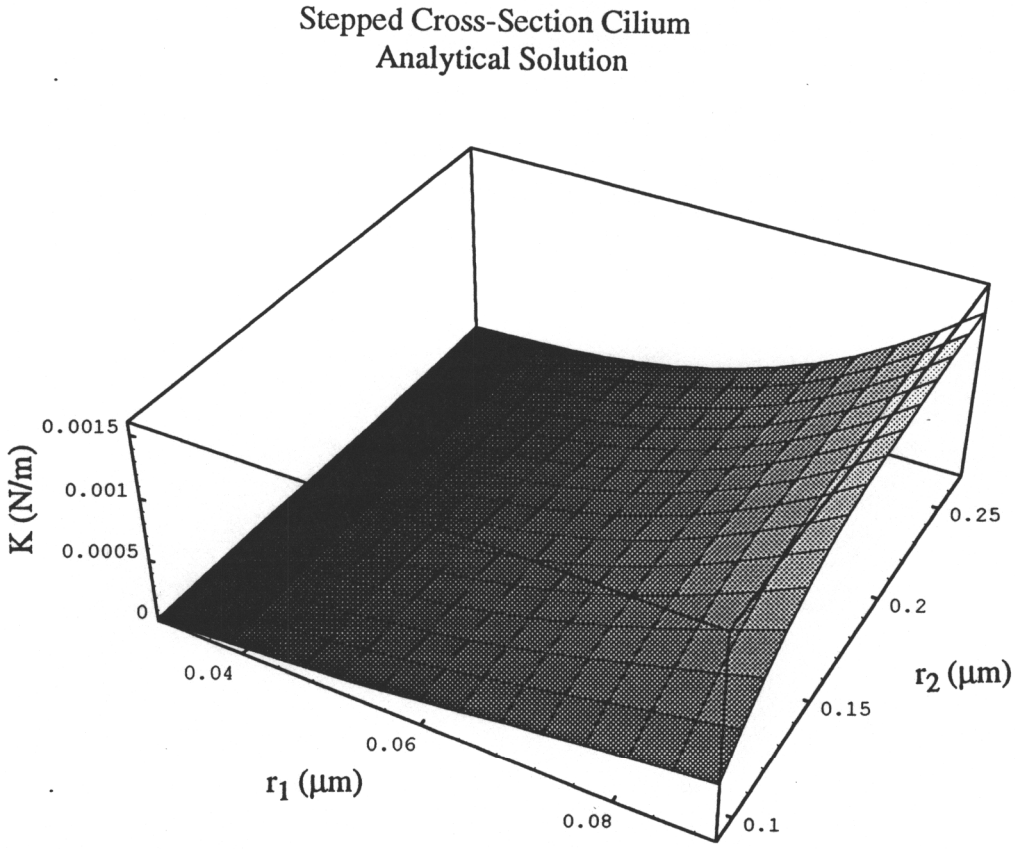

Figure 20. Stiffness versus characteristic stereocilium radii for the stepped cross-section analytical solution.
All other parameters are held constant.

increases with increasing shaft radius r_2 as well as with increasing base radius r_1. However, the relationship between K and r_1 is quite different from that between K and r_2. These relationships are illustrated in Figure 21 a and b. As in Figure 21a, if r_2 is held constant at any value, stiffness increases more rapidly as r_1 increases. As in Figure 21b, if r_1 is held constant at any value, stiffness begins to approach some asymptotic value as r_2 is increased, whereas at lower values of r_2, stiffness dramatically decreases with decreasing r_2.

In considering the deformation behavior of the single stereocilium, the analytic solution must be adjusted greatly to include factitious forces at each point where deflection is to be determined. This complication is a result of the nature of energy methods. Characterization of the single stereocilium deformation behavior will be left for FEA models.

3.2.2 Finite-Element Results

The finite-element model for the stepped cross-section, single cilium was constructed with beam elements. This 2-D representation was cantilevered at the base and forced by 200 pN at the free end. A force of 200 pN was chosen so that a deflection of approximately 1 μm would produce a stiffness in the range of the experimental values in Table 1. This force is also an average value of those used in experiments. In order to insure comparable deformations, this load case will be used consistently for each of the later models. The geometry of the cilium was constructed according to the values listed in Table 2.

Physiologic evidence indicates that most of the bending occurs in the tapered region and the extending uniform region remains approximately linear (Howard and Ashmore, 1986). Most of the bending of the stepped cross-section model as shown in Figure 22 occurs in the lower region as expected physiologically. Thus, this model does adequately characterize the physical bending of a single stereocilium. The top node was displaced 0.611 μm which gives a stiffness value of 3.27×10^{-4} N/m. This value for

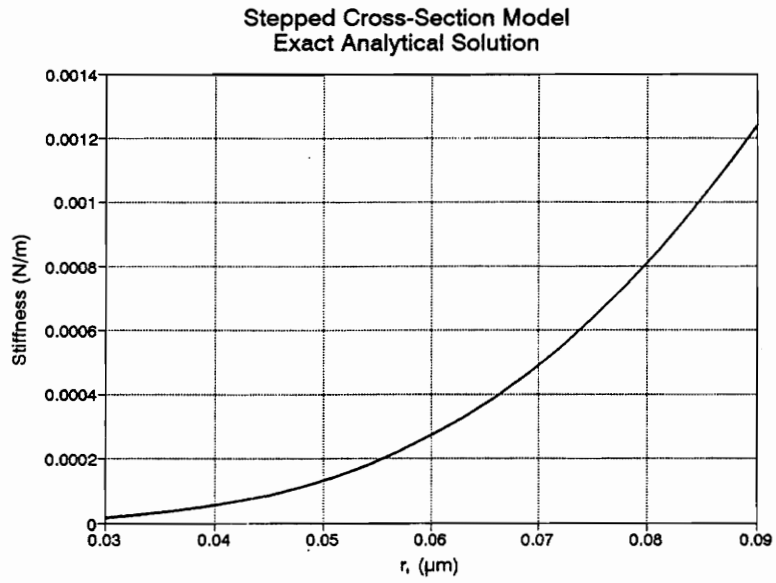

(a)

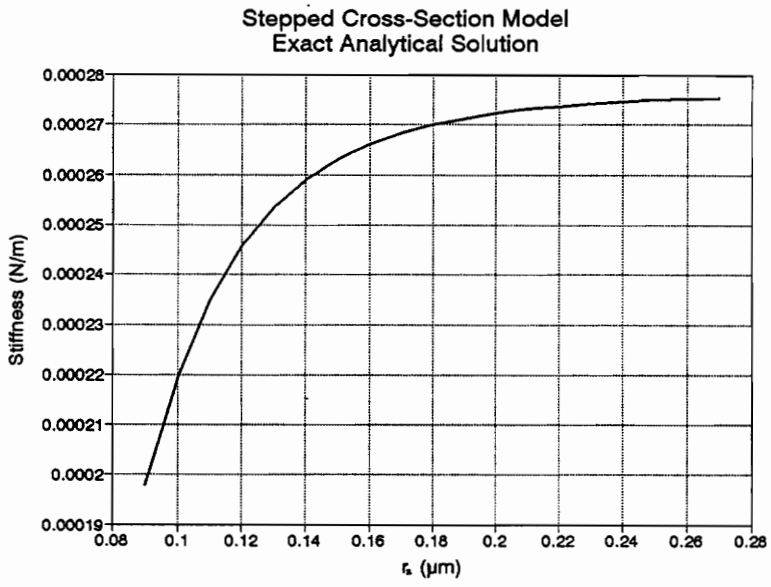

(b)

Figure 21. Stepped cross-section model stiffness trends with stereocilium radii.
(a) r_2 is held constant, while r_1 is varied. (b) r_1 is held constant, while r_2 is varied. All other model parameters are held constant in both cases.

Figure 22. FEA deformation results for single stepped cross-section stereocilium model. The bar elements used in the model are given a characteristic radius which is not a graphical attribute. Therefore, all elements appear the same size. Note that the model deforms as expected physiologically (bends at the base; straight in the uniform region). $K = 3.27 \times 10^{-4}$ N/m.

stiffness is exactly the value calculated from the analytical solution above. The following 2-D investigation uses this model in a coupled arrangement.

3.2.3 2-D Stereocilia Bundle Coupled By Tip-Links

The next step in adding complexity to the model is to include the tip-links. The tip-link tethers are easily modeled by springs with the material properties of actin. For the finite-element description, three stepped cross-section beams, increasing in height from 8 to 10 μm, were coupled together by attaching springs to the tips as shown in Figure 23a. The stereocilia were separated by a distance of 0.5 μm. This value was taken as an average of various micrograph observations. The spring constant k was calculated using the mechanics of materials formula

$$k = \frac{EA}{L_S} \tag{18}$$

where E is the Young's modulus for actin ($E = 3 \times 10^9$ N/m^2), A is the cross-sectional area, and L_S is the length of the spring. The cross-section of the tip-link was assumed to be uniformly circular with a diameter of 6 nm. The length of the spring was determined by the geometry of the model such that

$$L_S = \frac{d}{\cos\theta} \tag{19}$$

where d is the distance between the stereocilia (taken as 0.14 μm) and θ is the angle the tip-link makes with the horizontal. The calculated value for k was 4.2842×10^{-7} N/μm.

The top node of the tallest stereocilium was forced by 200 pN in the positive x-direction. The smaller two stereocilia displace as a result of the coupling springs. Figure 23b shows the results of this load case. Again, the stereocilia bend mostly in the tapered region as expected from physiologic evidence. The top node of the tallest stereocilium is displaced 0.18 μm which results in a bundle stiffness value of 1.11×10^{-3} N/m, an increase by a factor of 3.39 from the single stereocilium case. This model concludes the 2-D

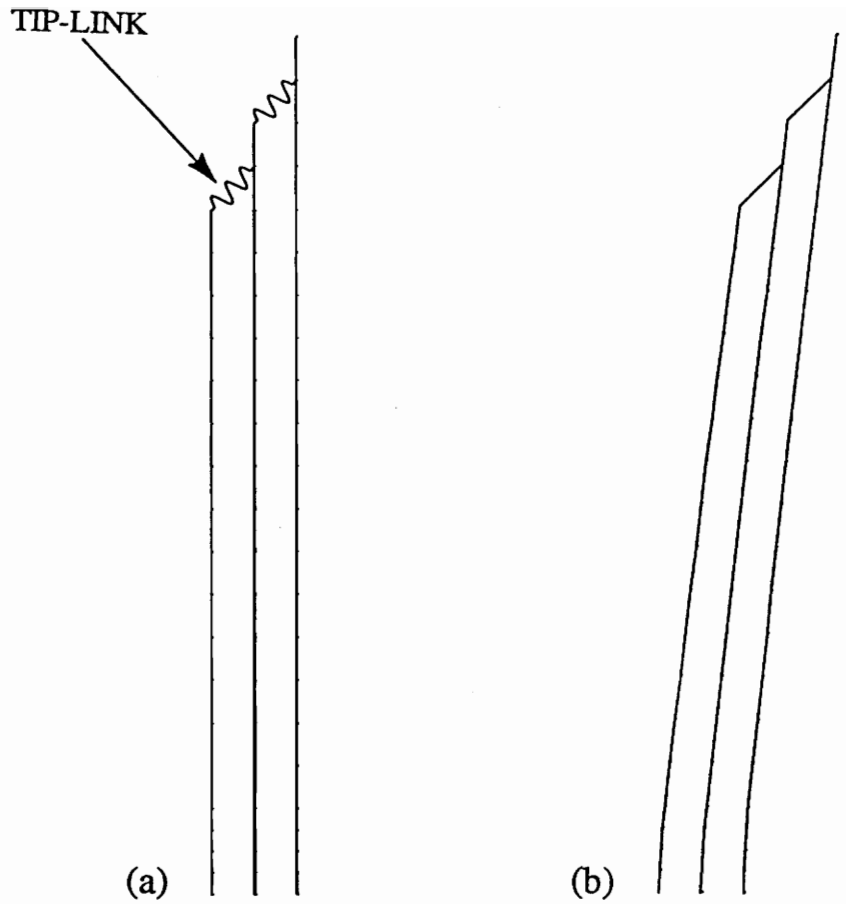

Figure 23. FEA stepped cross-section stereocilia bundle model linked by tip-links.
(a) Undeformed structure. Spring elements represent tip-links. (b) Deformation results. Tip-links are represented by straight lines, however, they are still spring elements. The deformed structure bends as expected physiologically. $K = 1.11 \times 10^{-3}$ N/m.

analysis. Three-dimensional models will now be analyzed in order to more accurately model shear effects, taper geometry, and increased stiffness resulting from the taper.

3.3 TAPERED BASE MODEL

The stiffness results of the stepped cross-section model should not be relied upon heavily. The increase in area when modeling the taper as a cone rather than a small cylinder will increase both the cross-sectional area and area moment of inertia calculations in Equation 7 and 10. This will result in decreasing the deflection of the free end and therefore increasing stiffness. A more accurate representation of the tapered region is necessary to determine the taper's effect on stiffness.

3.3.1 Energy Methods Results

Equations 7, 8, 9, and 14 were integrated by MATHEMATICA resulting in an equation for stiffness as a function of E, G, r_1, r_2, L_1, and L. As in the stepped cross-section analysis, the variables r_1, r_2, and L were varied over a range of +/- 50% of their values in Table 2, whereas the taper height L_1 was varied from 0.2 to 1.0 μm according to micrograph observations. For this wide range of geometric data, the maximum error in stiffness if shear was neglected again fell below 1%. Therefore, deformation due to shear was neglected for the remainder of the analyses since this assumption greatly simplifies the stiffness equations. The computed value of stiffness (neglecting shear) for the data in Table 2 was 1.66×10^{-3} N/m, which is five times the value for the stepped cross-section model. Although the stepped cross-section model adequately characterizes the general bending behavior of a single cilium, it does not give accurate estimates of stiffness. Therefore, the tapered base model will be used in the remaining analyses. Before constructing the finite-element model, it is necessary to further develop the analytical solution.

Figure 24 shows the variation of stiffness K with the two height parameters L_1 and L while the radius parameters are held constant ($r_1 = 0.06$ μm and $r_2 = 0.18$ μm). As in the

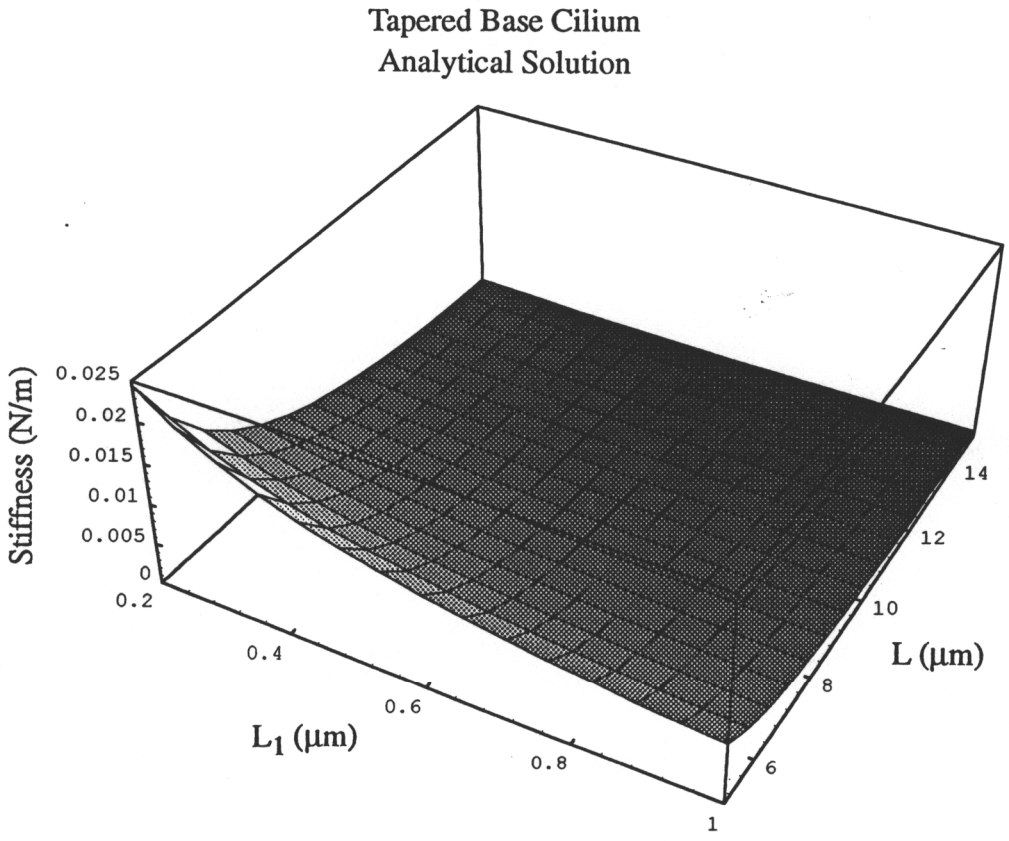

Figure 24. Stiffness versus characteristic stereocilium heights for the tapered base model analytical solution.
All other model parameters are held constant.

stepped cross-section model, stiffness decreases with an overall height increase as well as with increasing taper height. Therefore, shorter single stereocilium will have a greater stiffness than do taller ones with the same radii. If only higher order terms are retained in the stiffness equation (i.e. taper height is assumed to be very small compared to overall height), then the deflection equation for x simplifies to

$$x = \frac{4F}{3\pi E}\left[\frac{L^3}{r_2^4} + L^2 L_1\left(\frac{1}{r_1 r_2^3} + \frac{1}{r_1^2 r_2^2} + \frac{1}{r_1^3 r_2} - \frac{3}{r_2^4}\right)\right] \qquad (20)$$

There is an obvious similarity between this equation and the simplified stepped cross-section equation (Equation 17). First, the L^3 term is exactly the same in each equation. Second, both equations show an approximately linear relationship between deflection x and taper height L_1. However, the coefficient multiplying the L_1 term in each equation is markedly different. The maximum error in the simplification of Equation 20 over the complete data range is approximately 10%.

Figure 25 shows the variation in stiffness K with the two radii parameters r_1 and r_2 while the height parameters are held constant (L_1 = 1.0 μm and L = 10.0 μm). As in the stepped cross-section model, stiffness increases with increasing shaft radius r_2 as well as with increasing base radius r_1. The approximate linear change in stiffness with both radii is surprising since the radii are raised to the fourth power. One might expect results similar to the stepped cross-section model in Figure 21, but the integrated stiffness expression for the tapered model contains multiple terms which produce the approximate linear behavior in the range of the data. An extrapolation of the curve in Figure 25 will begin to resemble fourth order polynomial behavior.

3.3.2 Finite-Element Results

The finite-element model for the single cilium with a tapered base was constructed with wedge elements as illustrated in Figure 26a. Eight wedge elements were meshed into the circumference of the cilium. Along the length of the cilium in the uniform region the elements were 1 μm in length, whereas in the tapered region the elements were 0.5 μm in

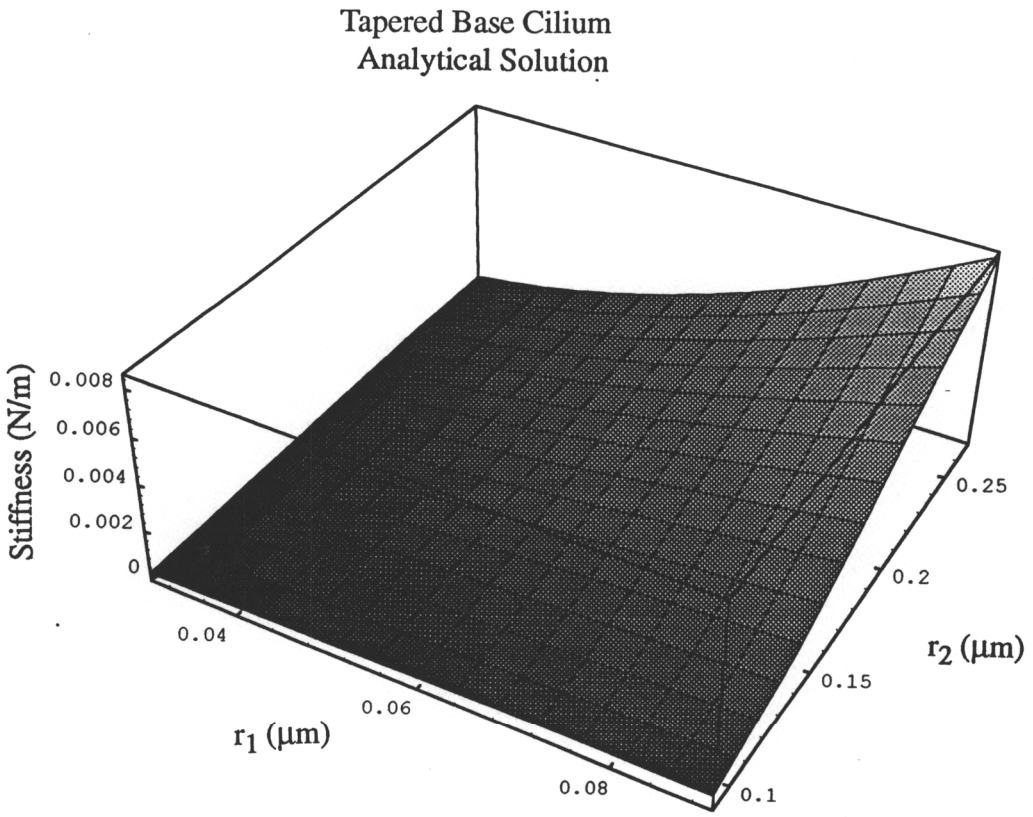

Figure 25. Stiffness versus characteristic stereocilium radii for the tapered base model analytical solution.

All other model parameters are held constant. Note that there is an approximately linear relationship between these variables over the plotted range. This trend would not be expected to continue over a larger range of data.

length. More elements are required in the tapered region since most of the bending occurs there. This 3-D representation of a single stereocilium was cantilevered at the base and forced by 200 pN at the free end as in previous models. Most of the bending of the tapered model as shown in Figure 26b occurs in the lower region as expected physiologically. Thus, this model adequately characterizes the physical bending of a single stereocilium. The stiffness value for this model was 2.28 x 10^{-3} N/m, which is a factor of 1.37 times greater than the analytical solution.

In hopes of achieving a model stiffness value closer to the analytical solution, two more finely meshed models were developed as pictured in Figure 27 a and b. The first of these models (Figure 27a) was a mesh of 8 wedge elements in the circumference, located at every 0.5 μm along the length. This mesh created twice as many elements in the uniform region as before. The resulting stiffness was 1.81 x 10^{-3} N/m, which is a factor of 1.09 times greater than the analytical solution. The second of these models (Figure 27b) was a mesh of 8 wedge elements in the circumference, located at every 0.25 μm along the length in the uniform region and at every 0.125 μm in the tapered region. The resulting stiffness was 1.26 x 10^{-3} N/m, which is a factor of 1.31 times lower than the analytical solution. This result seems quite surprising since the finite-element solution should be stiffer than the actual structure, or analytical solution. The anomaly would suggest that a physical parameter such as internal shear is not being modeled correctly by this configuration.

The possibility of inaccurately modeling shear was investigated by creating models with concentric cylinders and cones. The first model pictured in Figure 28a corresponds to the model in Figure 27a. All elements were distributed over 0.5 μm sections along the entire length of the cilium. However, 8 wedge elements and 8 hexagonal elements were meshed into the circumference of the cilium resembling two concentric sectioned circles. The resulting value for stiffness was 2.04 x 10^{-3} N/m, which is greater than its analog in Figure 27a (K = 1.81 x 10^{-3} N/m). It would initially appear that a greater distribution of elements along the model cross-section would increase

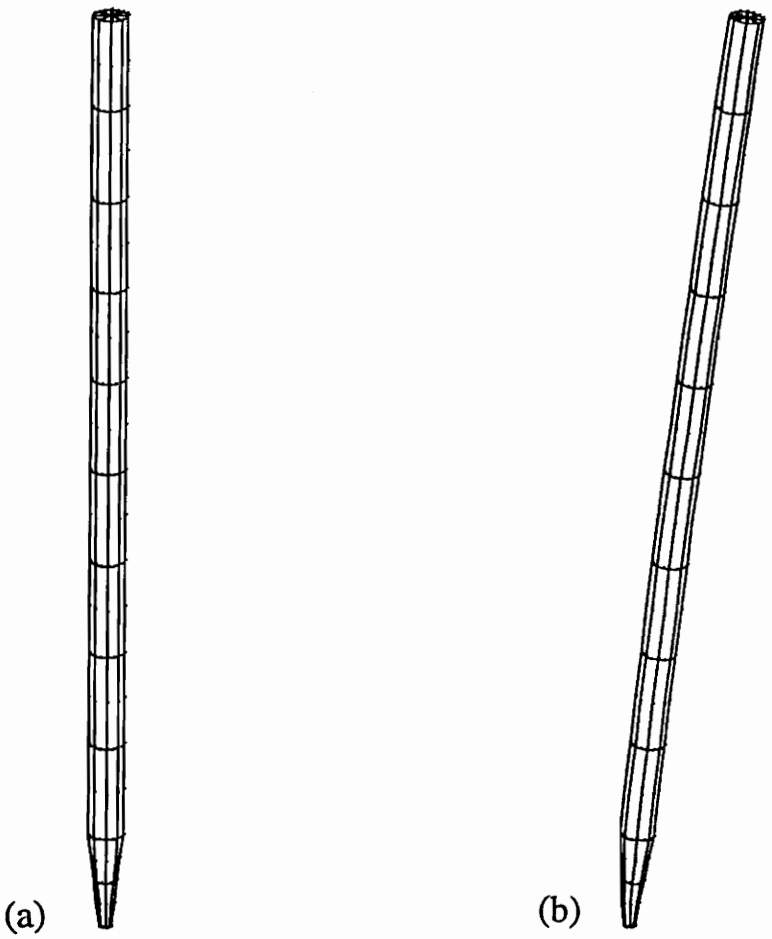

Figure 26. FEA single stereocilium, tapered base model.
(a) Undeformed structure. (b) Deformation results. The deformed structure bends as expected physiologically. $K = 2.28 \times 10^{-3}$ N/m.

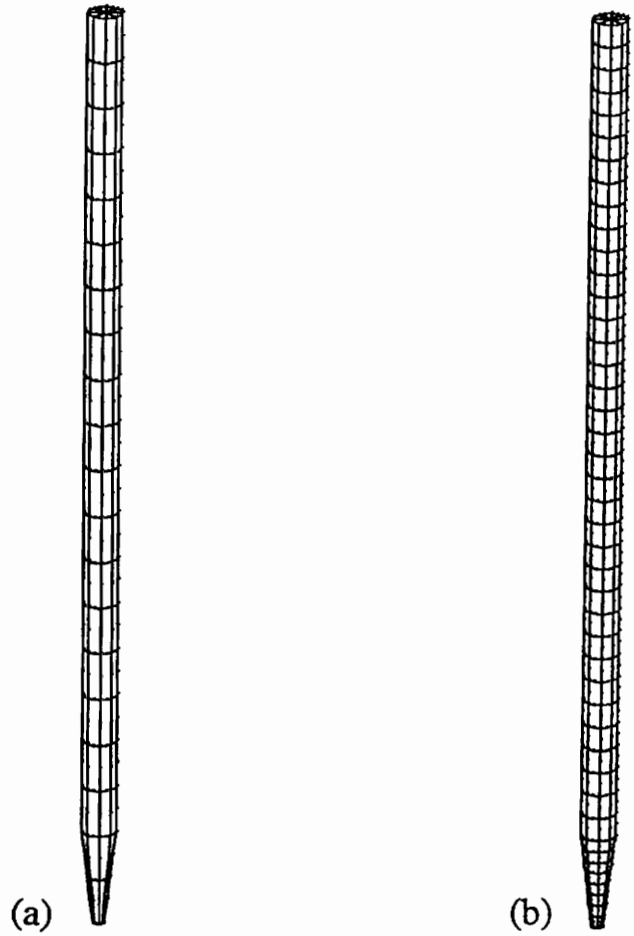

Figure 27. FEA meshing alternatives: finer uniform meshes.
(a) Elements meshed at every 0.5 μm. This configuration is used in most of the following models. (b) Elements meshed at every 0.25 μm in the uniform region and at every 0.125 μm in the tapered region. This configuration resulted in a stiffness below the value predicted by the analytical solution. FEA models should always be stiffer than the exact solutions. This deviant case may suggest other unaccounted for interactions such as internal shear.

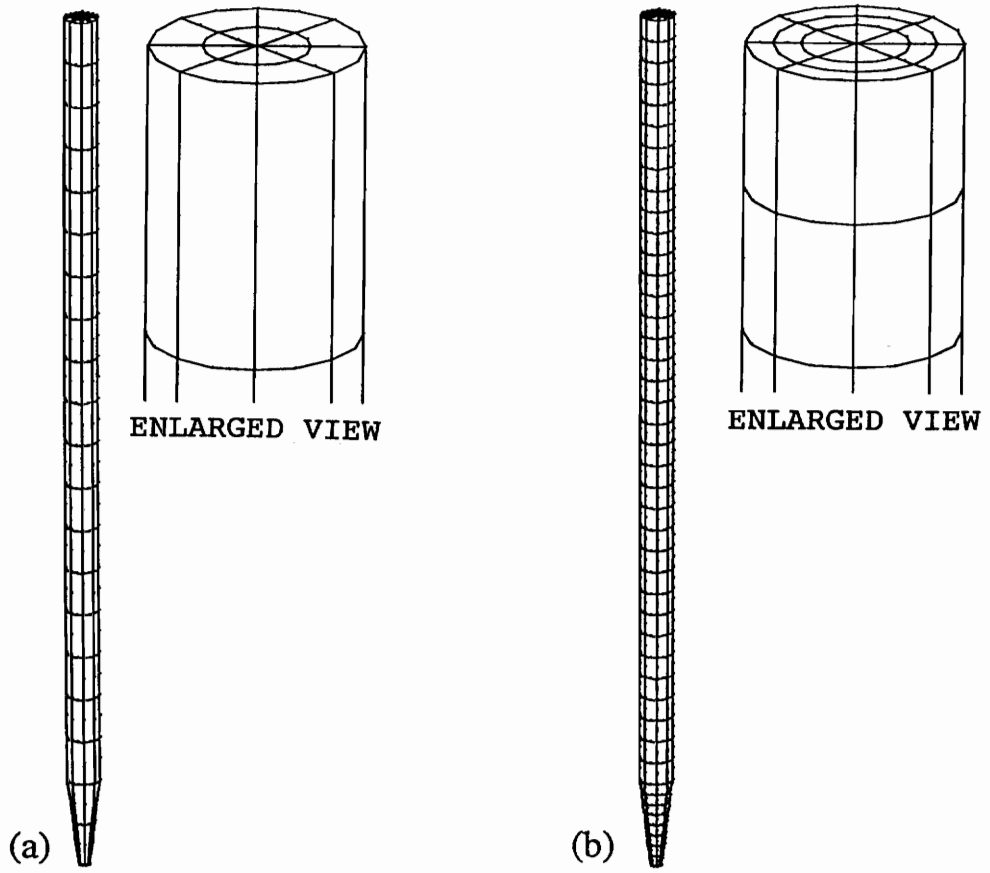

Figure 28. FEA meshing alternatives: internal shear evaluation.
(a) One concentric shell of elements around a cylindrical core. (b) Two concentric shells of elements around a cylindrical core. The results suggested that there was some internal shear, however, no trends could be determined. Therefore, a previous cylindrical model was used (Figure 27a) since it best approximated the analytical solution.

stiffness. However, this increase did not occur when the model in Figure 28b was meshed corresponding to the model in Figure 27b. All elements were distributed over 0.25 μm sections along the cilium length in the uniform region and 0.125 μm sections in the tapered region. Eight wedge elements and sixteen hexagonal elements were meshed into the circumference of the cilium resembling three concentric sectioned circles. The resulting value for stiffness was 1.22×10^{-3} N/m, which is lower than its analog in Figure 27b ($K = 1.26 \times 10^{-3}$ N/m). The reason for such differences in stiffness has not been determined. Nevertheless, it would seem that shear does play a role in determining model stiffness. The following analysis uses the model of Figure 27a in a coupled arrangement.

3.3.3 3-D Stereocilia Bundle Coupled By Tip-Links

As in the stepped cross-section model, the next step in adding complexity to the tapered model is to include the tip-links. The tip-link tethers are modeled in a similar fashion as with the coupled stepped cross-section bundle. For the finite-element description, three 3-D tapered base stereocilia, increasing in height from 8 to 10 μm, were coupled together by attaching springs to the tips as shown in Figure 29a. The stereocilia were separated by a center-to-center spacing of 0.5 μm. The spring constant k was calculated using the mechanics of materials formulas in Equations 18 and 19. The cross-section of the tip-link was assumed to be uniformly circular with a diameter of 6 nm. The length of the spring was determined by the geometry of the model such that the distance between the stereocilia was 0.14 μm. The calculated value for the spring constant k was 4.2842×10^{-7} N/μm.

The top node of the tallest stereocilium was forced by 200 pN in the positive x-direction. Figure 29b shows the results for this load case. Again, the stereocilia bend mostly in the tapered region as expected from physiologic evidence. The top node of the tallest stereocilium is displaced 0.033 μm which results in a bundle stiffness value of 6.08×10^{-3} N/m, an increase by a factor of 3.36 from the single stereocilium case. This value for stiffness is also a factor of 12 greater than average experimental values (taken as 5×10^{-4} N/m). This factor is not surprising considering the assumptions inherent in the

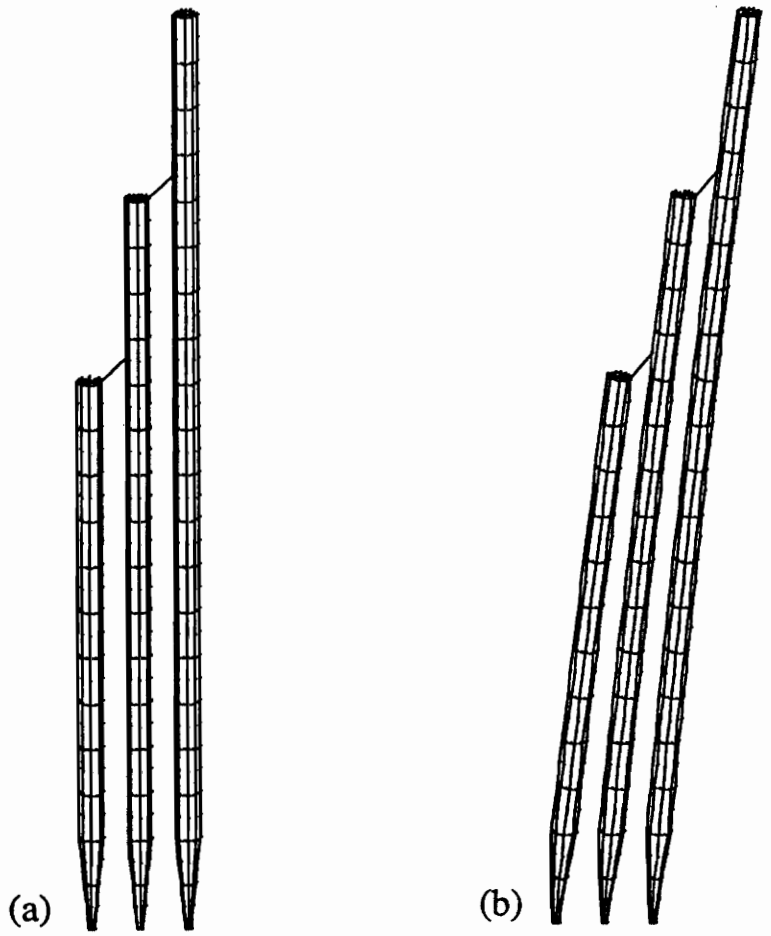

Figure 29. FEA tapered base stereocilia bundle model coupled by tip-links.
(a) Undeformed structure. (b) Deformation results. The deformed structure bends as expected physiologically. $K = 6.08 \times 10^{-3}$ N/m.

model: linear, elastic, isotropic, homogeneous material under linear deformation theory. Coarse element discretization, the cantilevered boundary conditions, and the point-load application of the force could also contribute to greater stiffness values. With these assumptions and conditions taken into account, the model approximation of experimental stiffness favors continuing the analysis.

With the stiffness of an individual stereocilium determined, a cilium geometry can be chosen that is below the experimentally measured stiffness values while keeping within the range of acceptable dimensions. The values chosen for an individual stereocilium that were incorporated into the bundle models were: $r_1 = 0.03$ μm, $r_2 = 0.125$ μm, $L_1 = 1.0$ μm, and L = 6 to 10 μm. The stiffness value for the tallest stereocilium would then be approximately 3.5×10^{-4} N/m from the analytical solution. This value is well within the experimentally reported values listed in Table 1. The center-to-center spacing will remain at 0.5 μm making the distance between the stereocilia in the upper region 0.25 μm. The change in distance between the stereocilia results in a change in the spring constant for the tip-link tethers. However, the spring constant was not adjusted for three main reasons. First, the new model geometry represents the actin core without the surrounding membrane, therefore the distance between the stereocilia is actually less than 0.25 μm. Second, micrograph observations indicate that the shorter stereocilia are actually pulled towards the taller stereocilia by the tip-link, therefore decreasing the tip-link's actual length. And third, the adjusted spring constant is approximately a factor of 2 lower than the true value. This will be shown in later analyses to result in an insignificant change in overall bundle stiffness.

3.4 MODELING OF SUBAPICAL BANDS

The next step in modeling the bundle interconnections is to include the effects of the subapical bands. The first method of modeling these dense areas of interconnections was a solid piece of material connecting two adjacent stereocilia just below the tip-link. This type of configuration was chosen due to evidence of bleb like structures that seemed

to interconnect bundled stereocilia as in Figure 30. The finite-element model for the solid connection is shown in Figure 31a. The applied load at the tip of the tallest stereocilium produced the deformed structure shown in Figure 31b. The solid interconnection produced deformation of the stereocilia which was inconsistent with observed deformation where the bending takes place at the tapered base while the upper region remains straight. The solid interconnecting elements create high levels of shear along the edges parallel to the long axis of the stereocilia. This shear creates a torque resulting in the twisting behavior in the vicinity of the solid connection. In addition to the obvious inconsistency in deformation behavior, this type of connection produced large increases in the overall bundle stiffness (approximately 254 x 10^{-4} N/m) which were about 2 orders of magnitude above the experimentally measured values. Literature obtained during the analysis phase of this project indicated that these structures were probably artefacts (see Chapter 1 discussion on SEM and TEM). The results of the solid interconnection model seem to confirm that such a structure would not enable the observed deformation behavior. For these reasons, this type of interconnection was considered incorrect.

Micrograph observations, presumably not artefacts, have shown the subapical bands to be tip-link like filaments running between adjacent stereocilia parallel to the cuticular plate. The finite-element model shown in Figure 32a consisted of simple beam elements interconnecting the stereocilia in the subapical region. The beam elements were modeled as 6 nm diameter actin filaments which were free to pivot at their termination points. This configuration produced a very dense region of interconnections as is observed in SEM micrographs. The resulting deformation shown in Figure 32b was consistent with observed deformation behavior. The stiffness value for this model was 2.12 x 10^{-3} N/m, which is approximately a factor of 4 greater than average experimental values and well within the full range of experimental values.

Unfortunately, I was not aware of a problem in the construction of this model until most of the work in this project was completed. The beam elements have three rotational degrees of freedom, whereas the 3-D wedge and hexagonal elements have no rotational

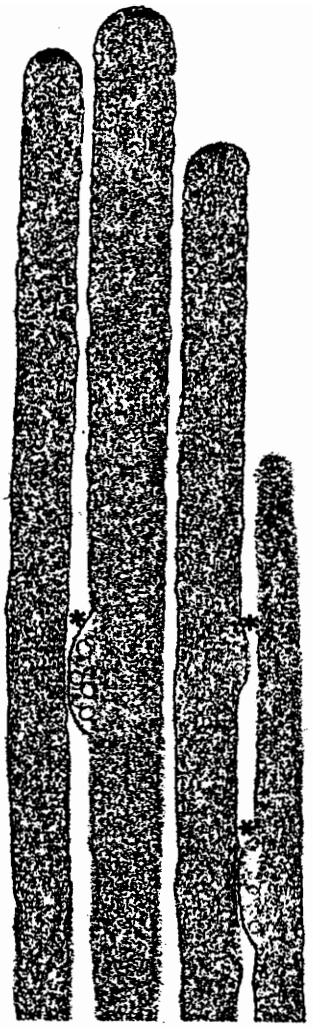

Figure 30. Bleb-like structures that seemingly interconnect bundled stereocilia (Friedmann and Ballantyne, 1984).

Although recent evidence suggests that these bleb-like structures are arefacts due to fixation, micrographs such as this one lead to the inclusion of a solid subapical connection in the FEA model.

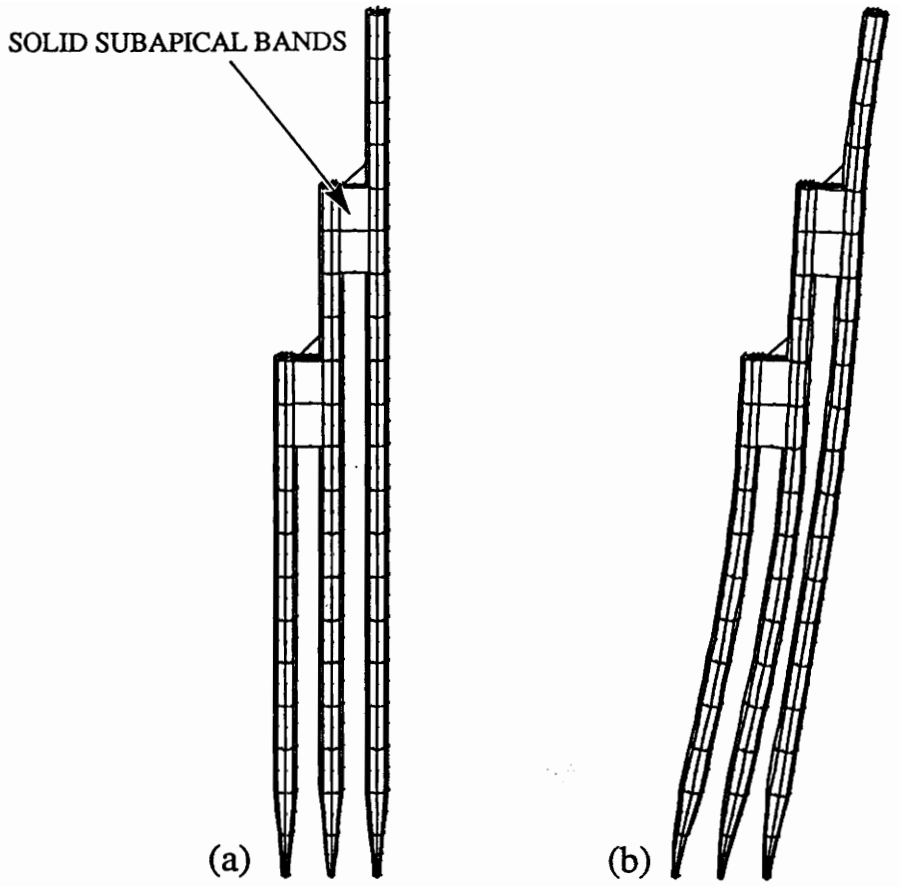

Figure 31. FEA tapered base stereocilia bundle model coupled by tip-links and solid, subapical interconnections.

(a) Undeformed structure. (b) Deformation results. The solid interconnection produced deformation of the stereocilia which was inconsistent with observed deformation. The solid interconnecting elements create high levels of shear along the edges of the stereocilia which results in the S-shape twisting behavior shown. The stiffness value for this model, $K = 2.54 \times 10^{-2}$ N/m, is about 2 orders of magnitude greater than experimentally measured values. The results confirm that such a bleb-like structure does not model experimentally observed behavior. Note also that in this and following models the stereocilia characteristic lengths have been reduced effectively reducing the stiffness of each single stereocilium.

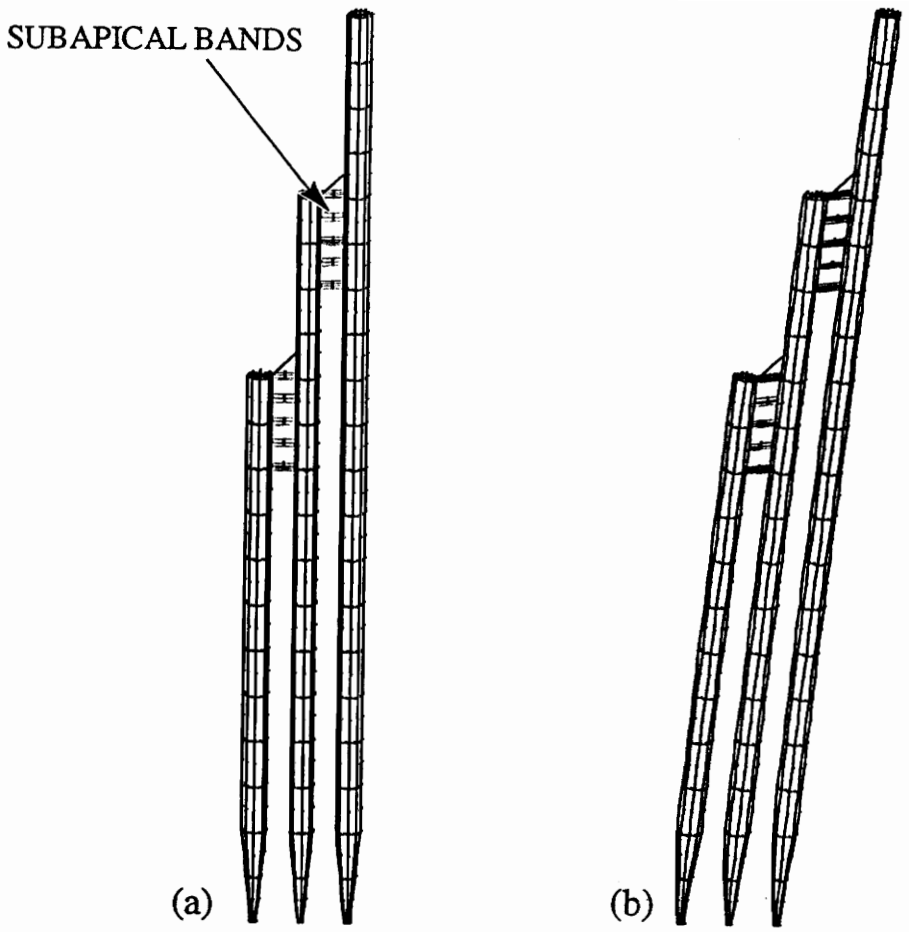

Figure 32. FEA tapered base stereocilia bundle model coupled by tip-links and bands of subapical beam elements.

(a) Undeformed structure. (b) Deformation results. Micrograph observations have shown bands of subapical filaments running between adjacent stereocilia parallel to the cuticular plate. These 'subapical bands' were modeled by dense areas of beam elements connecting adjacent stereocilia. The deformation behavior was consistent with experimental observation. The stiffness value, $K = 2.12 \times 10^{-3}$ N/m, is a factor of 4 greater than average experimental values, yet falls within the range of reported stiffnesses.

degrees of freedom. Since the nodes at the termination points of the beam elements are shared with 3-D elements, an inconsistency occurs in the formulation of the finite-element equations. The results output file from ABAQUS warned of possible errors due to this inconsistency. To correct the problem, spring elements having no rotational degrees of freedom replaced the beam elements in modeling the subapical bands as illustrated in Figure 33a. The value for the spring constant computed from Equation 18 was 3.40×10^{-7} N/μm. The resulting deformation shown in Figure 33b was consistent with observed deformation behavior. The stiffness value was computed as 2.08×10^{-3} N/m, which was very close to the model using beam elements (2.12×10^{-3} N/m). In fact, other spring element models varying geometry, load magnitudes, and moduli all produced stiffness values within a 5% error of models using beam elements. The reason for such a small error lies in the linear deformation theory which assumes small deformations, small rotations. The linear models included in the following chapters consist of both beam and spring subapical band configurations. Since the error between the two elements was very small, they were considered interchangeable in the linear analyses. All models using large deformation theory were constructed using spring subapical bands. The model size is broken down as follows: 1,707 nodes, 44 spring elements, 384 wedge elements, 5,121 total model variables, and 213 degrees of freedom. This model will be considered the standard, or control if you will, for the following parameter studies. It has shown to be a valid approximation of experimental stiffness and deformation behavior.

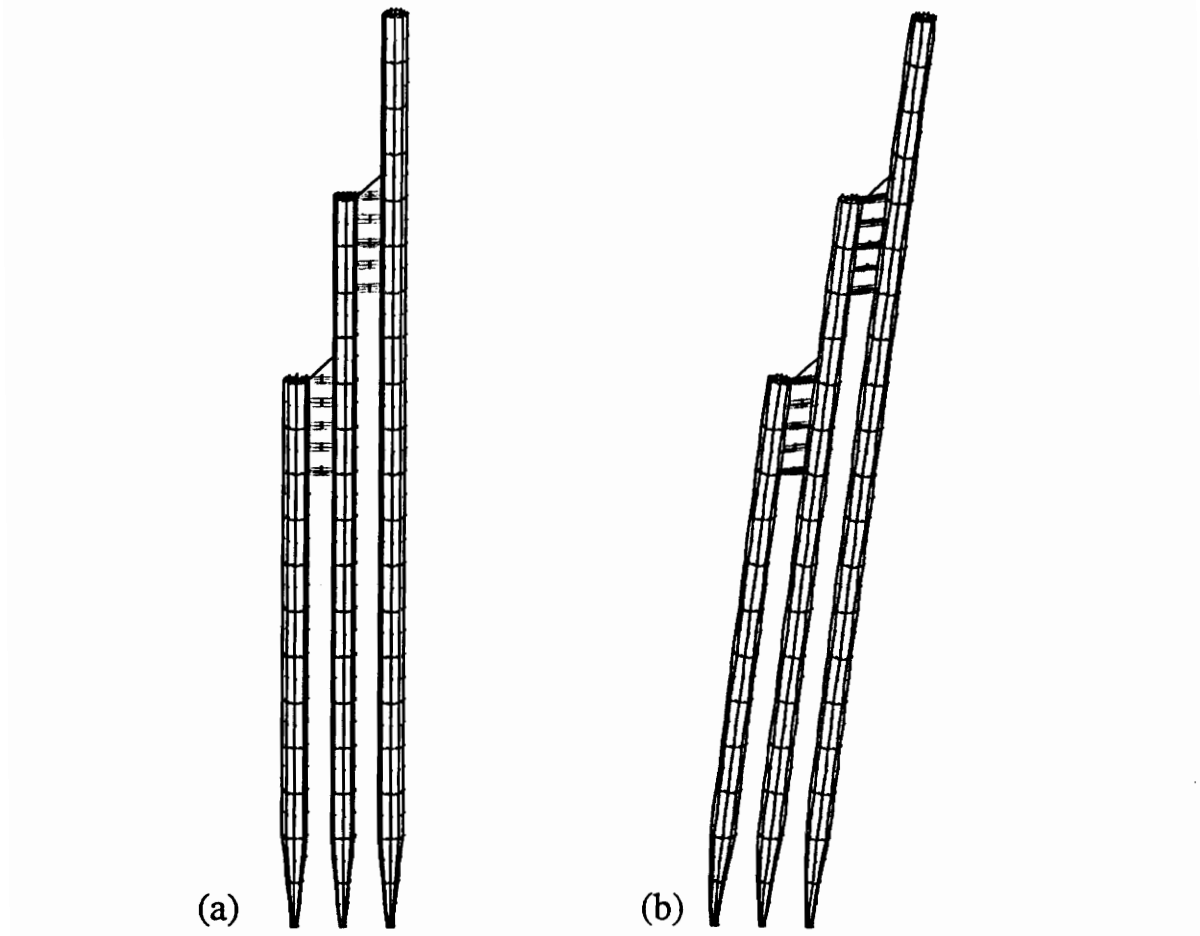

Figure 33. FEA tapered base stereocilia bundle model coupled by tip-links and bands of subapical spring elements.

(a) Undeformed structure. (b) Deformation results. During the analysis phase of this project, it was discovered that an inconsistency in elemental degrees of freedom had occurred between the 3-D wedge elements (3 translational degrees of freedom) and the beam elements (3 translational and 3 rotational degrees of freedom). In order to eliminate this error, spring elements (3 translational degrees of freedom only) were used in place of the beams. Although the error seems significant in theory, the error between this model with springs and the previous model with beam elements in linear analyses was less than 5%. Deformation results from both models are also extremely similar. Spring elements were used in all nonlinear analyses.

4.0 FEA MODEL PARAMETRIC STUDIES

The three stereocilia model interconnected with tip-links and subapical bands was used to determine the effects of geometric and material parameters on stiffness. The stiffness contributed by the subapical bands and tip-links has been established by comparing models including these structures to models without these structures. Parametric studies were performed on subapical bands, tip-links, and the interconnected stereocilia bundle. Models concentrating on the stiffness effects of the subapical bands varied the density of interconnections and moduli, whereas tip-link parametric studies varied orientation angle and moduli. Stiffness effects of the total number of stereocilia, center-to-center spacing of stereocilia, and step in height between stereocilia were also determined. These parameter studies will enable researchers to determine to what extent each structure contributes to bundle stiffness.

Small displacement theory will be used in all models in this chapter. The criterion for considering a displacement small will be based relative to the largest stereocilium diameter in the model. This would correspond to a value of 0.25 μm for the following models. In Chapter 5 large deformation analysis will be used to determine possible nonlinearities.

4.1 LOAD-DEFLECTION CURVES

Applied load versus deflection curves were generated for the single cilium and cilia bundle models. Mechanics of materials small displacement theory predicts a linear relationship between load and displacement giving rise to a constant stiffness. Finite-element small displacement theory also resulted in a linear relationship between load and displacement as shown in Figure 34 a and b. The slope of the line in Figure 34a is 1.26 x 10^{-3} N/m, which is the constant value of stiffness for the single cilium model. For the cilia bundle, the loads were applied in excitatory (positive loads) and inhibitory (negative loads) directions. As shown in Figure 34b for the cilia bundle, the relationship between

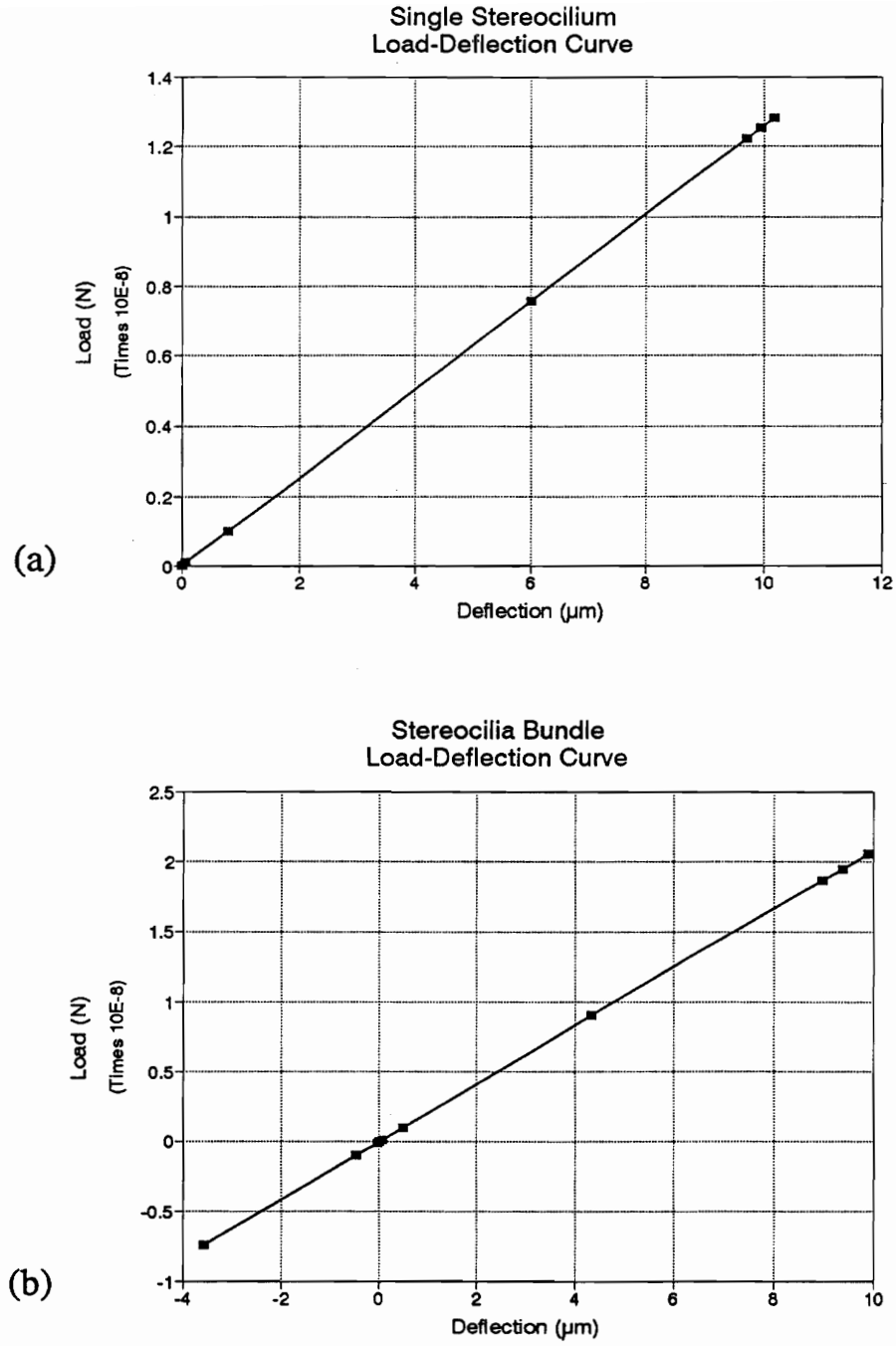

Figure 34. Linear load-deflection curves.

Load-deflection curves were generated for (a) a single stereocilium and (b) a stereocilia bundle. Each curve is a straight line with a constant slope equal to the characteristic stiffness for that particular model.

load and displacement is a straight line whose slope is 2.08×10^{-3} N/m, which is the constant value of stiffness for the stereocilia bundle model. Obviously, the stiffness in the excitatory direction is equal to the stiffness in the inhibitory direction. This result is consistent with experimental data (Crawford and Fettiplace, 1985; Howard and Hudspeth, 1987) obtained at displacements of 1 to 100 nm, which is well below the small displacement criterion of 0.25 μm. Large displacement theory is not expected to give similar linear results.

4.2 TIP-LINKS

Hair cell tip-links are central to any discussion of mechanoelectrical transduction and, therefore, hair bundle stiffness. Tip-links have been implicated as the gating-spring structure in the predominant transduction model (Pickles, 1985). These filaments are ideal for transferring the necessary force to open the transduction channels via the displacement of the bundle by surrounding media. The upper end of the link is connected to the central actin core of the stereocilium, whereas the lower end of the link is often seen pulling the stereocilia membrane up to a point (Pickles and Corey, 1992). While this latter observation is possibly due to fixation shrinkage, it suggests that the link is not directly attached to the actin core.

The pulling action of the tip-link on the stereocilia membrane is also indicative of tip-link pretension. Experiments on bullfrog sacculi have shown that the stereocilia bundle displaces approximately 133 nm in the excitatory direction when the tip-links are removed (Assad et al., 1991). However, the elimination of tip-links and the loss of bundle tension may only be coincidental. Tip-link removal is achieved through biochemical treatment with the calcium chelator BAPTA. Therefore, bundle relaxation may be a result of stereocilium and/or subapical band degradation, as well as tip-link removal. Inclusion of these mechanical events into the finite-element model is extremely difficult. For this report, the tip-link is simply modeled as a spring which is connected to two stereocilia. Future models should adapt present concepts to include the possibility of additional

compliance in the stereocilia membrane and pretension in the tip-links. The purpose of the following analysis is to determine the effect of the tip-links on bundle stiffness. The results will provide insight into the mechanical function and molecular structure of the tip-links.

4.2.1 Tip-Link Contribution To Overall Bundle Stiffness

When the tip-links were removed, the bundle stiffness value became 9.61 x 10^{-4} N/m, which is a reduction of approximately 55%. When the tip-links were broken experimentally by the BAPTA solution the experimental stiffness reduced by approximately one-half (J. W. Grant, personal communications). This reduction in stiffness is also consistent with the gating-spring model of Howard and Hudspeth (1988). If the gating-spring stiffness term is removed from the bundle stiffness equation, then the reduction in stiffness is approximately one-half. These results seem to suggest that the tip-links may be the gating-springs.

4.2.2 Tip-Link Orientation Effects On Stiffness

Hair cell degradation during microscopy preparation can cause the tip-links to appear at various orientation angles. The orientation angle is defined by the angle the lower tip-link end makes with the horizontal. The links are most often seen as almost vertical, yet some micrographs have shown them to extend from the stereocilium at angles as low as 45°. Figure 35 shows the four angles chosen for this analysis: 45°, 63.4°, 71.6°, 76°. These angles were chosen such that no adjustment in the finite-element mesh was necessary. The graph in Figure 36 shows the FEA results. The relationship between stiffness and tip-link orientation is approximately linear in this range, with stiffness increasing as orientation angle increases. This relationship also suggests that increasing the orientation angle will increase the tension in the spring for a given deflection.

Some recent experiments (Pickles and Corey, 1992) have shown that large stimuli easily saturate hair cell transduction. Consequently, hair cells have developed an apparent adaptation mechanism which controls tip-link tension during excitation. The current adaptation model proposes an active motor element which allows the upper end of the tip-

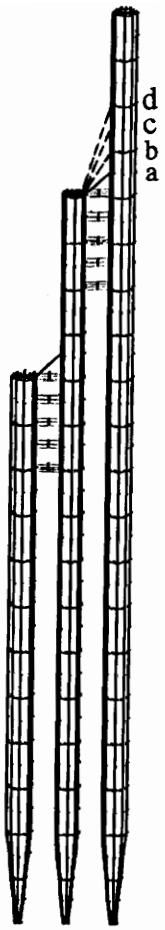

Figure 35. FEA stereocilia bundle models varying tip-link orientation angle: model configuration.

Without any adjustment to the FEA mesh, the variation of stiffness with tip-link orientation could be determined for the angles (a) 45°, (b) 63.4°, (c) 71.6°, and (d) 76°.

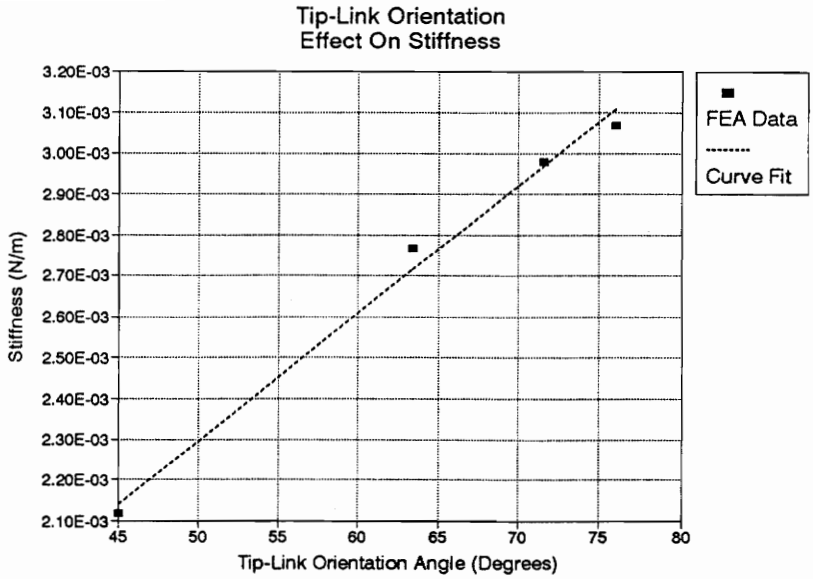

Figure 36. Stiffness versus tip-link orientation angle.
Stiffness increases approximately linearly with increasing tip-link orientation angle. Linear regression gives $K = 3.12 \times 10^{-5}\ \theta + 7.36 \times 10^{-4}$ N/m as the curve fit equation.

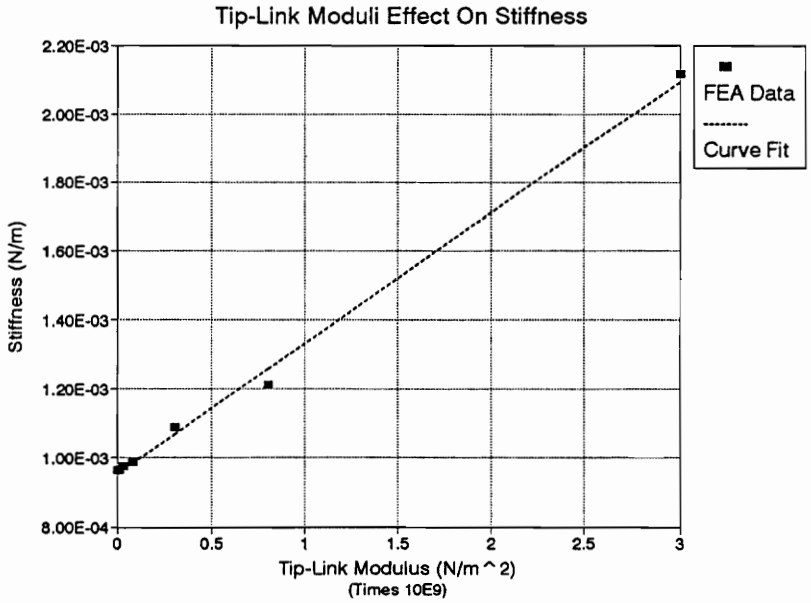

Figure 37. Stiffness versus tip-link Young's modulus.
Stiffness decreases approximately linearly with decreasing tip-link Young's modulus. Linear regression gives $K = 3.8 \times 10^{-13}\ E + 9.5 \times 10^{-4}$ N/m as the curve fit equation.

link to slide along the side of the stereocilium during displacement. The linear relationship between stiffness and orientation angle could provide such dramatic adjustments in tension. Future finite-element models should include the possible sliding of the upper tip-link attachment. This would also increase the compliance in the FEA model, thereby more closely approximating the average experimental stiffness values.

4.2.3 Tip-Link Modulus Effects On Stiffness

Experiments performed by Howard and Hudspeth (1988) on the bullfrog sacculi were applied to the gating-spring model. The results enabled the spring constant for the gating-spring to be determined. If the tip-link is assumed to be the gating-spring structure, then a Young's modulus for the tip-link can be determined with mechanics of materials formulas. The Young's modulus was found to be 4 MPa, which is characteristic of the protein elastin. This modulus is approximately three orders of magnitude less than the value for actin (3 GPa). In order to determine the effect of tip-link modulus on overall bundle stiffness, an array of models were developed varying the tip-link modulus in a range of 3 MPa to 3 GPa. The graph in Figure 37 shows an approximately linear relationship between bundle stiffness and tip-link modulus. A dramatic decrease in stiffness is seen between tip-link moduli of 3 GPa to 800 MPa. Decreasing the tip-link modulus below 800 MPa has less of a dramatic effect. If the tip-link Young's modulus is approximately that of elastin, then the resulting bundle stiffness is about 9.6×10^{-4} N/m. This value for stiffness is remarkably close to the experimental value of 9.3×10^{-4} N/m obtained by Howard and Hudspeth (1988) for the bullfrog sacculi.

4.3 SUBAPICAL BANDS

The presence and structure of the subapical bands is another controversial topic in hair cell physiology. The presence of solid, bleb like interconnections has been accepted as artefacts, while filamentous connections are believed to occur in the subapical regions of the stereocilia and possibly along the stereocilia's entire length. But even the presence of these filamentous links has been disputed. The purpose of the following analysis is to

determine the effect of bands of subapical links on bundle stiffness. The results will provide insight into the mechanical function of such bands and a basis for further investigations.

4.3.1 Subapical Band Contribution To Overall Bundle Stiffness

When the subapical bands were removed, the value of stiffness became 1.11×10^{-3} N/m, which is a reduction of approximately 50%. This result suggests that the subapical bands could also be the gating-spring structure allowing transduction. Unfortunately, the wealth of experiments on tip-link function have not been applied to the subapical bands as well. Therefore, the suggestion that the tip-links are indeed the gating-springs should be considered inconclusive. Similar removal of the subapical bands may too eliminate transduction and result in bundle relaxation consistent with the gating-spring model.

4.3.2 Subapical Band Density Effect On Stiffness

The subapical bands are generally seen in SEM and TEM micrographs as a dense region of interconnections. In previous models, twenty-one elements in a 1 μm region characterized the many interconnections. The effect of a decrease in the density of interconnections was determined by analyzing the model illustrated in Figure 38. The number of interconnections has been reduced from 21 to 11, or roughly half. The resulting stiffness was 2.09×10^{-3} N/m, which is a reduction of approximately 1%. Therefore, the density of interconnecting subapical bands is relatively insignificant in determining bundle stiffness as long as a few are present.

4.3.3 Subapical Band Height Effect On Stiffness

Most investigators have limited the bands of horizontal linkages to the upper, subapical, regions of the stereocilia (Pickles, 1985; Furness and Hackney, 1985). However, some researchers have noted that these links may occur along the entire length of the stereocilia (Assad et al., 1991). The effect on stiffness of linkages occurring in the lower regions of the stereocilia was determined by increasing the band height through a range of 0 to 5 μm as in Figure 39. Band height is defined as the length along the long axis of the stereocilia where the bands occur as measured from the tip of the shorter

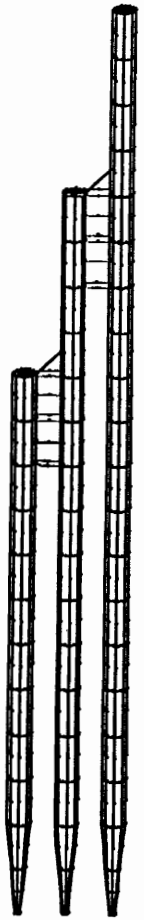

Figure 38. FEA stereocilia bundle model interconnected with few subapical bands.

The number of subapical band elements was reduced from 21 to 11 elements to determine its effect on stiffness. This reduced stiffness by less than 1%.

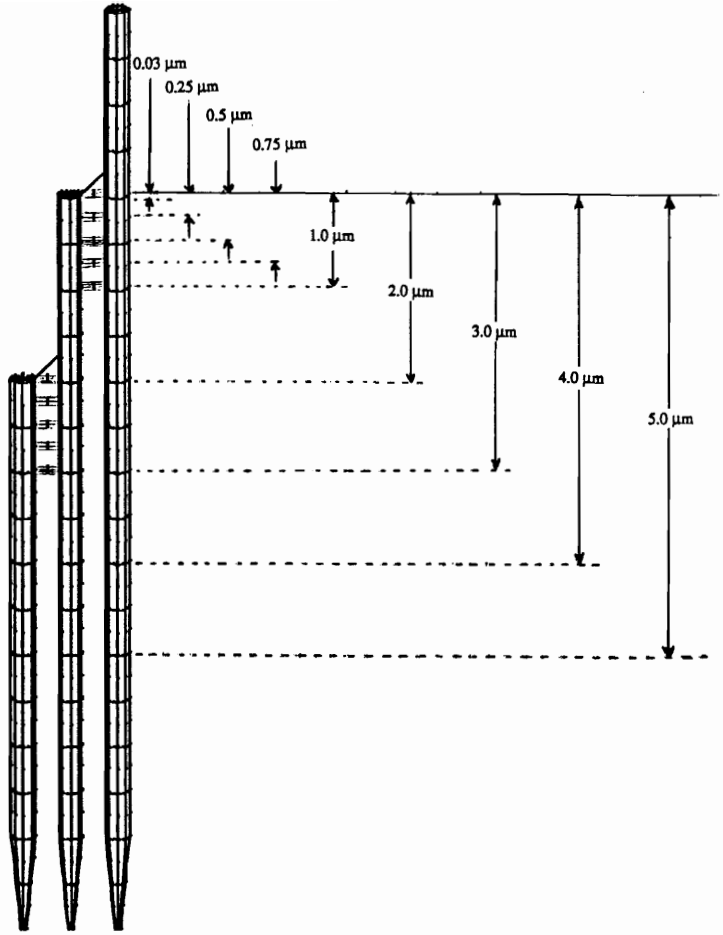

Figure 39. FEA stereocilia bundle models varying band height: model configuration.

Band height was defined as the length along the long axis of the stereocilium where the bands occur as measured from the tip of the shorter stereocilium. Zero band height refers to the model coupled by tip-links only (i.e. subapical bands are not present). Small increases in stiffness with increasing band height are seen after the first row of elements.

stereocilium. Zero band height indicates the absence of the subapical bands; the stereocilia are connected by tip-links only. The first row of subapical bands at the tip of the shorter stereocilium is given a band height of 0.03 μm, which is the radius used in the spring constant equation. As shown in Figure 40, stiffness almost doubles as band height increases from 0 to 0.03 μm, or as one row of subapical links is added to the tip-links only model. Beyond this first row of links, stiffness remains approximately constant. In recent experiments (Assad et al., 1991), the lower links were found to be highly susceptible to degradation in enzyme treatment where other linkages (subapical bands and tip-links) remained intact. Also, removal of the lower links does not effect the mechanoelectrical transduction of the hair cell (Jacobs and Hudspeth, 1990). The results of this finite-element analysis seem to support the insignificance of lower links in determining stiffness. Therefore, these links would not be expected to be strong, load bearing structures, nor would they play a role in transduction. However, if the bases of the stereocilia were allowed to move relative to one another, the lower links would then play a role in stiffness. This would occur in the event of bowing of the cuticular plate, which has been recently observed (J. W. Grant, personal communications).

4.3.4 Subapical Band Modulus Effect On Stiffness

The material structure of the subapical bands has yet to be determined. In order to determine the effect of elastin bands rather than actin formed bands, the Young's modulus for this structure was varied over a range of 3 MPa to 3 GPa. Contrary to the results of tip-link modulus effect on stiffness, there is not a linear relationship between subapical band modulus and stiffness as shown in Figure 41. Over the full range of band moduli, bundle stiffness dropped by less than half. In fact, reducing the band modulus from 3 GPa to 3 MPa achieved the same reduction in stiffness as reducing the tip-link modulus from 3 GPa to 800 MPa. More accurate tip-link and subapical band material definitions will be necessary in future finite-element studies.

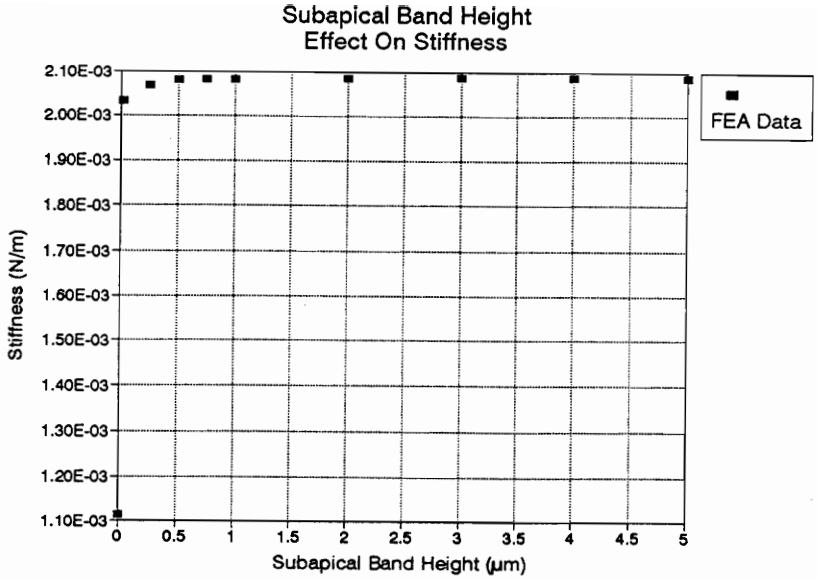

Figure 40. Stiffness versus subapical band height.
Adding one row of subapical elements to the tip-links only model results in a dramatic increase in stiffness. Small increases in stiffness with increasing band height are seen after the first row of elements.

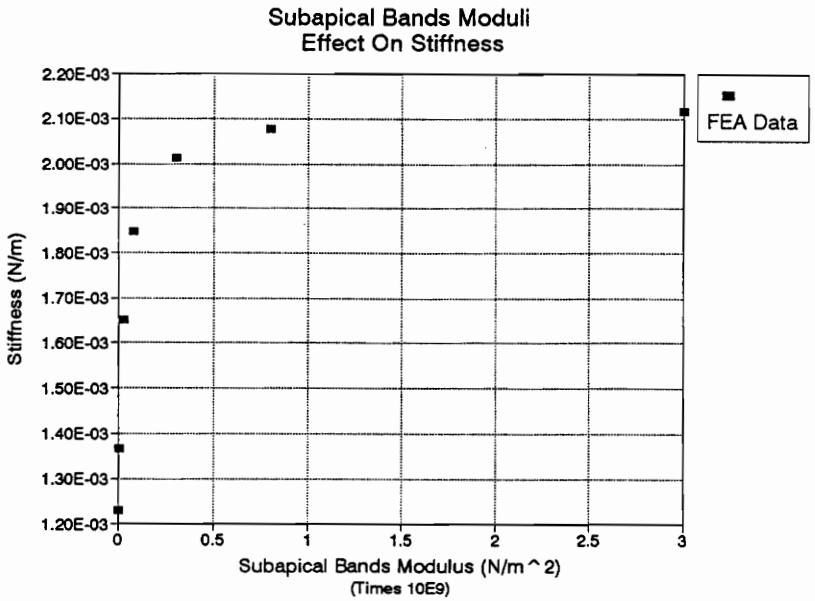

Figure 41. Stiffness versus subapical band Young's modulus.
Reducing subapical band Young's modulus by 3 orders of magnitude resulted in a reduction in stiffness by less than 50%.

4.4 STEREOCILIA MODULUS

The material description of the stereocilia is a major assumption in this work. Model material assumptions include linear elastic, homogeneous, isotropic, nearly incompressible behavior. Most, if not all, of these assumptions are invalid, some to more of a degree than others. In this fundamental work, the prescribed material properties adequately characterize the physical nature of the hair cell stereocilia for the purpose of establishing the feasibility of finite-element modeling and performing basic parameter studies. However, a rudimental effect can be studied by simply varying the value for Young's modulus for the stereocilia. As was done for the tip-links and subapical bands, the stereocilia modulus ranged in this analysis from 3 MPa to the original value of 3 GPa.

The results shown in Figure 42 describe an interesting behavior. By considering the upper most three points and the lower most three points, two straight lines (power law relationships) can be drawn through these two regions. An investigation of the resulting deformation behavior at each of the points in Figure 42 reveals the reason for such a curve. The six panels of Figure 43 show the deformed cilia bundle corresponding to each modulus in Figure 42 (except for E = 3 GPa presented earlier) in descending order (800 MPa to 3 MPa). There is a definite transition in deformation behavior beyond 300 MPa. Below this value, the stereocilia bundle begins to twist into an S-shape as in the solid subapical band models presented previously. The displacement results have been normalized for comparison; the deformation is actually much greater than shown for the models below 300 MPa. This behavior is inconsistent with expected physiologic behavior. Therefore, a lower limit of stereocilia modulus in this particular model can be established at approximately 300 MPa. This type of analysis would prove most useful when more accurate material definitions can be made.

4.5 BUNDLE GEOMETRY

So far, the bundle models have consisted mostly of three interconnected stereocilia ranging in height from 6 to 10 μm at a center-to-center spacing of 0.5 μm. The preceding

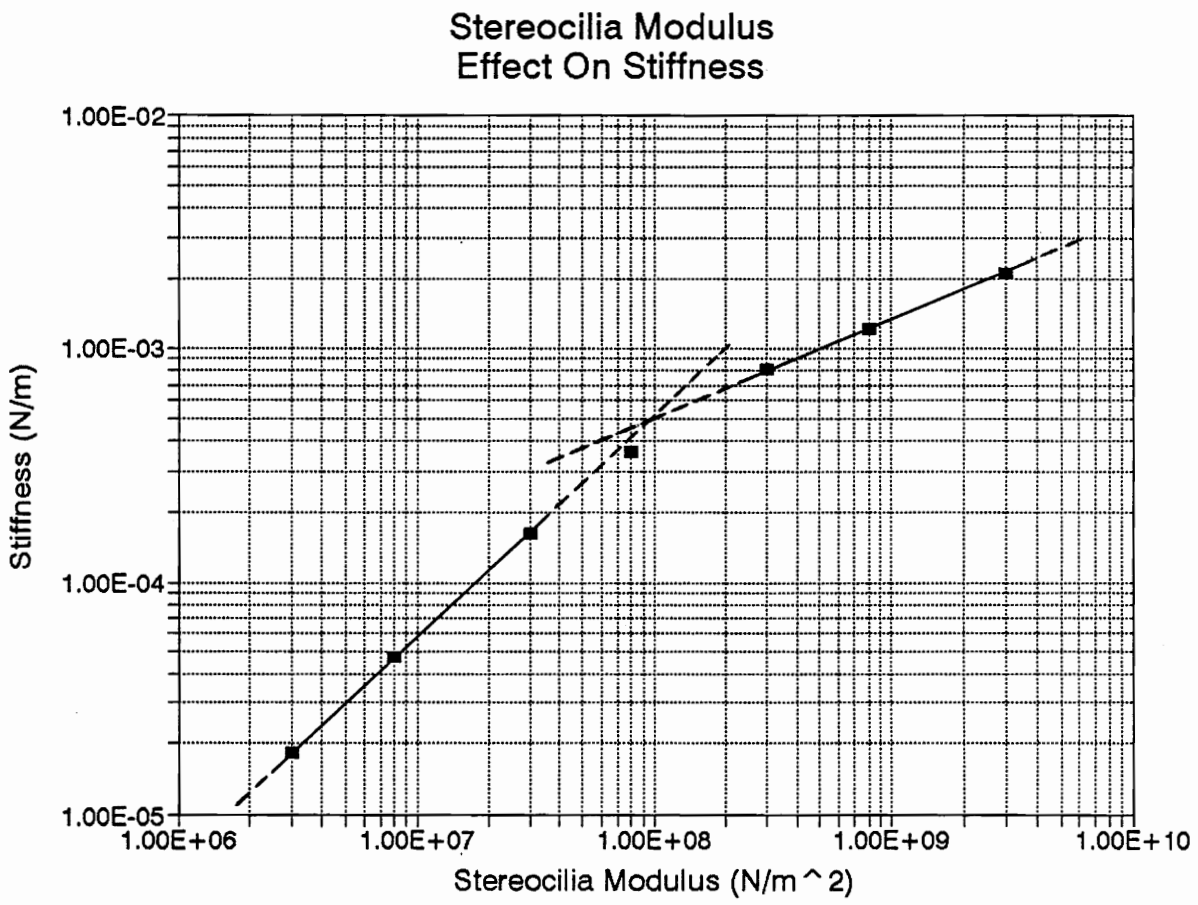

Figure 42. Stiffness versus stereocilium Young's modulus.

Two distinct linear regions are shown by the two straight lines. These regions mark a transition point in deformation behavior. The bundle bends as expected in the upper region, while it twists and distorts in the lower region. This analysis would seem to suggest a limit of 300 MPa as a possible stereocilium Young's modulus.

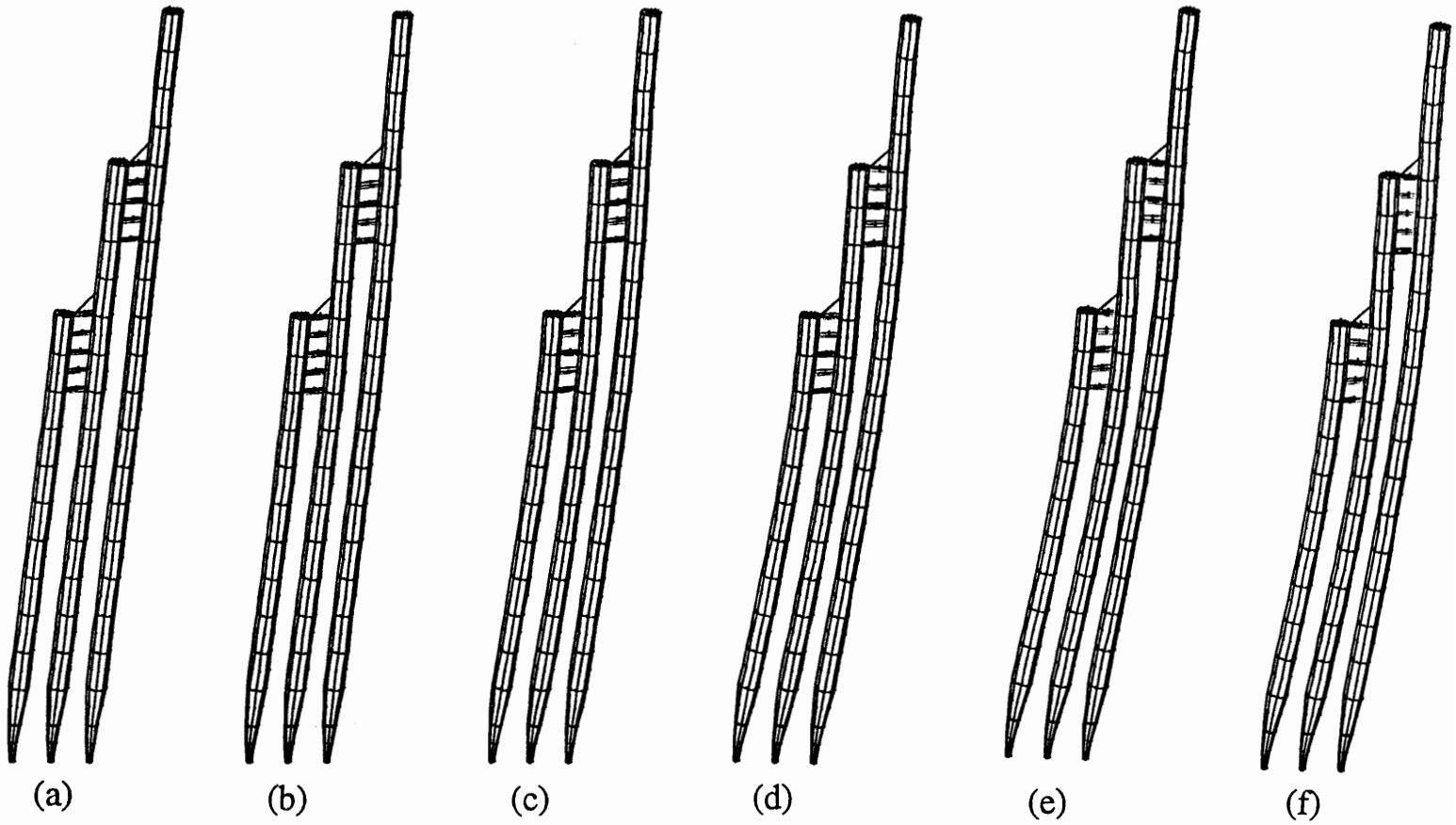

Figure 43. FEA stereocilia bundle deformation results for varied stereocilium Young's modulus.

Deformed structures corresponding to the data in Figure 42 in decending order of modulus. The model corrseponding to a Young's modulus of E = 3 GPa (the standard model) was presented in Figure 33 and is not shown again here. The models shown are for: E = (a) 800 MPa, (b) 300 MPa, (c) 80 MPa, (d) 30 MPa, (e) 8 MPa, (f) 3 MPa. Unrealistic physiologic response occurs below E = 300 MPa. The deformations have been normalized for comparison.

models have varied bundle component moduli, orientation, and location so that we may understand each component's effect on overall bundle stiffness. On a more macroscopic level, the following analysis will model stiffness dependence on bundle geometry. The geometric factors presented here include bundle width (i.e. number of stereocilia and center-to-center spacing), height variations (i.e. uniform and nonuniform changes in height), and the effect of nonparallel stereocilia.

4.5.1 Stereocilia Bundle Width Effect On Stiffness

The three stereocilia bundle represents the inner hair cell bundles of mammalian cochlea typically found as three straight rows. In other regions of the cochlea and in the vestibular apparatus, hair bundles generally have more than three rows of graded stereocilia. The models pictured in Figure 44 were analyzed to determine the effect on stiffness of increasing the number of rows in the bundle. The model in Figure 44a has added a 4 μm tall cilium to the previous three cilia model, whereas the model in Figure 44b added a 4μm and a 2 μm tall cilium to the three cilia model. The cilia heights were chosen to keep a constant 2 μm gradation in stereocilia height. The stiffness of the four cilia model was computed as 2.91×10^{-3} N/m, which is an increase of 38% from the three cilia model. The stiffness of the five cilia model was computed as 3.62×10^{-3} N/m, which is an increase of 72% from the three cilia model. These moderate increases in stiffness, while not orders of magnitude above the three cilia model, may suggest differences in cell function. Stiffness differences between cell location are compounded by other dimensional and geometric variables sited in previous sections.

Another way that cells even with the same number of stereocilia can alter bundle width is to change the center-to-center spacing between the individual stereocilia. The model pictured in Figure 45 has a reduced center-to-center spacing of 0.375 μm. This value results in a reduction by one-half of the space between the stereocilia in the upper region. The resulting stiffness was 3.31×10^{-3} N/m, which is an increase of 54% from the previous three cilia model. This increase in stiffness results from an increase in shear between the stereocilia. For a given bundle deflection, the spring elements would be more

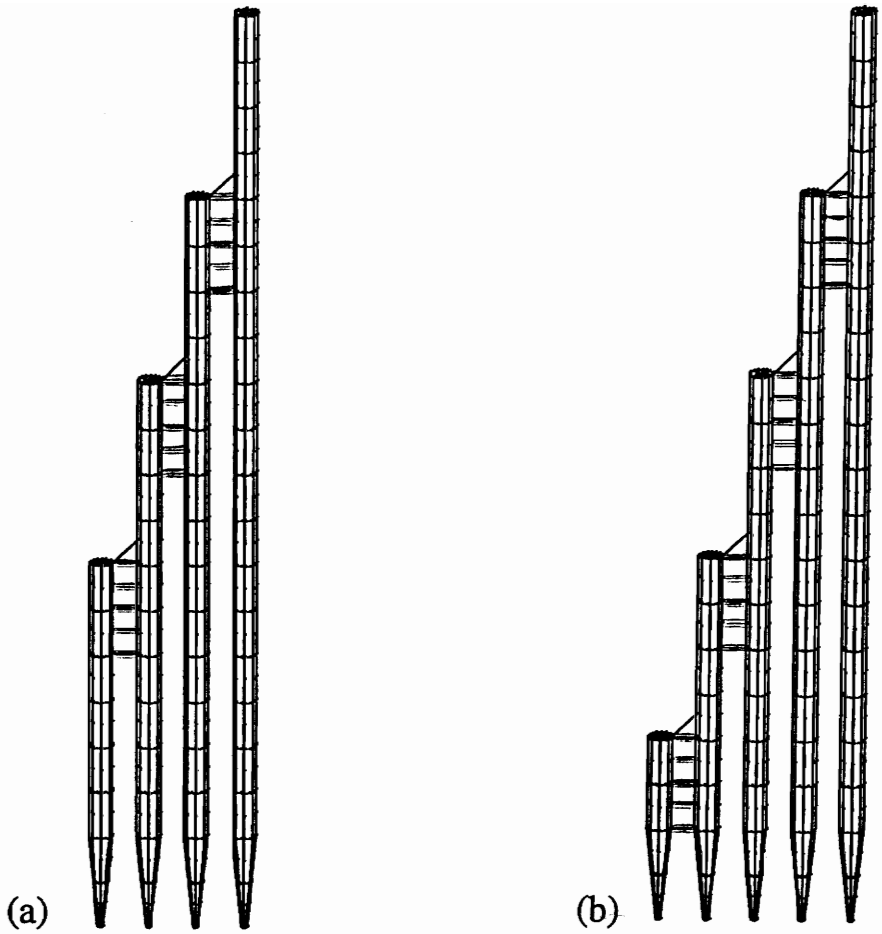

Figure 44. FEA stereocilia bundle models with increased bundle width.
(a) Four stereocilia model. K = 2.91 x 10^{-3} N/m. (b) Five stereocilia model. K = 3.62 x 10^{-3} N/m. Each model has a uniform increase in stereocilium height equal to 2 μm.

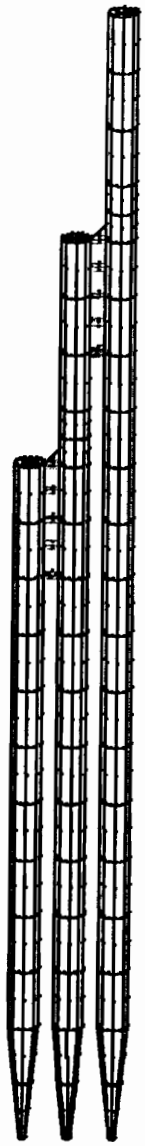

Figure 45. FEA stereocilia bundle model with decreased center-to-center spacing.
The center-to-center spacing was reduced from 0.5 μm to 0.375 μm. $K = 3.31 \times 10^{-3}$ N/m, an increase of 54%.

stretched the closer the stereocilia. This results in an increased tension in the spring elements effectively increasing the shear between the stereocilia.

4.5.2 Stereocilia Incremental Height Variation Effect On Stiffness

The height difference between neighboring stereocilia was increased from 2 μm in the standard model to 3 μm and to 4 μm as shown in Figure 46 a and b, respectively. The resulting stiffnesses were 1.98 x 10^{-3} N/m and 1.81 x 10^{-3} N/m for the 3 μm and 4 μm height variations, respectively, which is a maximum reduction in stiffness of approximately 15%. This would seem to indicate that the slope of increasing height, in the case of uniform height differences, is not as important to overall bundle stiffness as is number of stereocilia, stereocilium geometry, and interconnection effects.

Some investigations (E. H. Peterson, personal communications) have revealed a pattern of exponentially increasing in height stereocilia bundles. The five cilia model pictured in Figure 47a represents such a bundle with the following cilia heights: 2, 2.5, 3.5, 6, and 10 μm. These numbers are arbitrary and do not reflect any specific experimental data. The model simply serves to indicate a trend in stiffness with respect to uniform verses nonuniform height variations. The resulting stiffness was found to be 2.95 x 10^{-3} N/m, which is a decrease of approximately 20% from the uniformly graded five cilia model. While this decrease is not extremely significant, bundles with more dramatic height differences should not be simplified as having a constant slope. The deformed structure shown in Figure 47b gives reason for the reduction in stiffness. Since the subapical bands are connected at a lower point on the taller stereocilia, a moment is produced sufficient to result in bending in the uniform region of the stereocilium, and thus decreasing the overall bundle stiffness.

4.5.3 Stereocilia With Convergent Axes Effect On Stiffness

As discussed in Chapter 1, stereocilia bundles in general do not have uniformly spaced, parallel axes. Instead, their axes are often convergent as depicted by the three cilia model in Figure 48. The resulting stiffness for this model was 3.54 x 10^{-3} N/m, which is an increase of 40% from the standard three cilia model with parallel axes. It is interesting

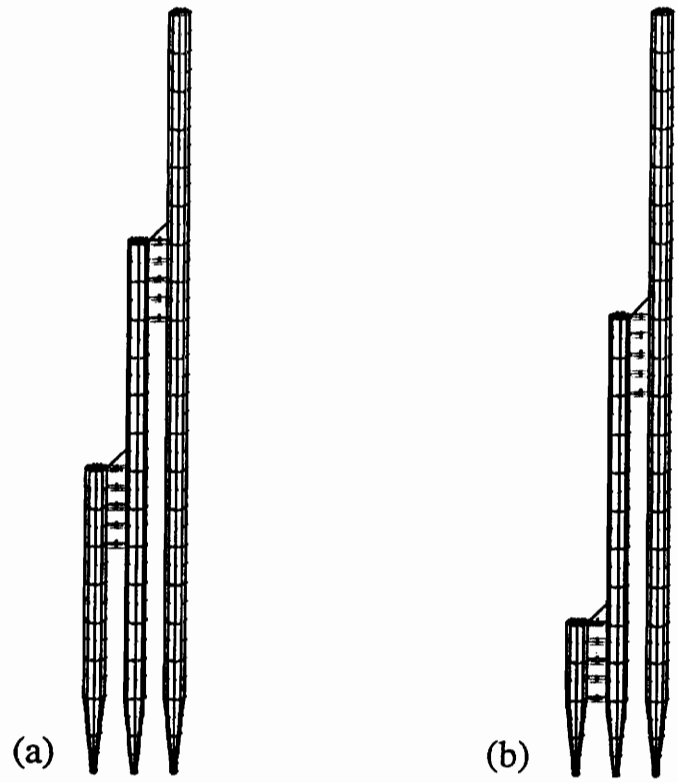

Figure 46. FEA stereocilia bundle models with increased stereocilia height differences.
The height difference between neighboring stereocilia was increased from 2 μm in the standard model to (a) 3 μm (K = 1.98 x 10^{-3} N/m) and (b) 4 μm (K = 1.81 x 10^{-3} N/m).

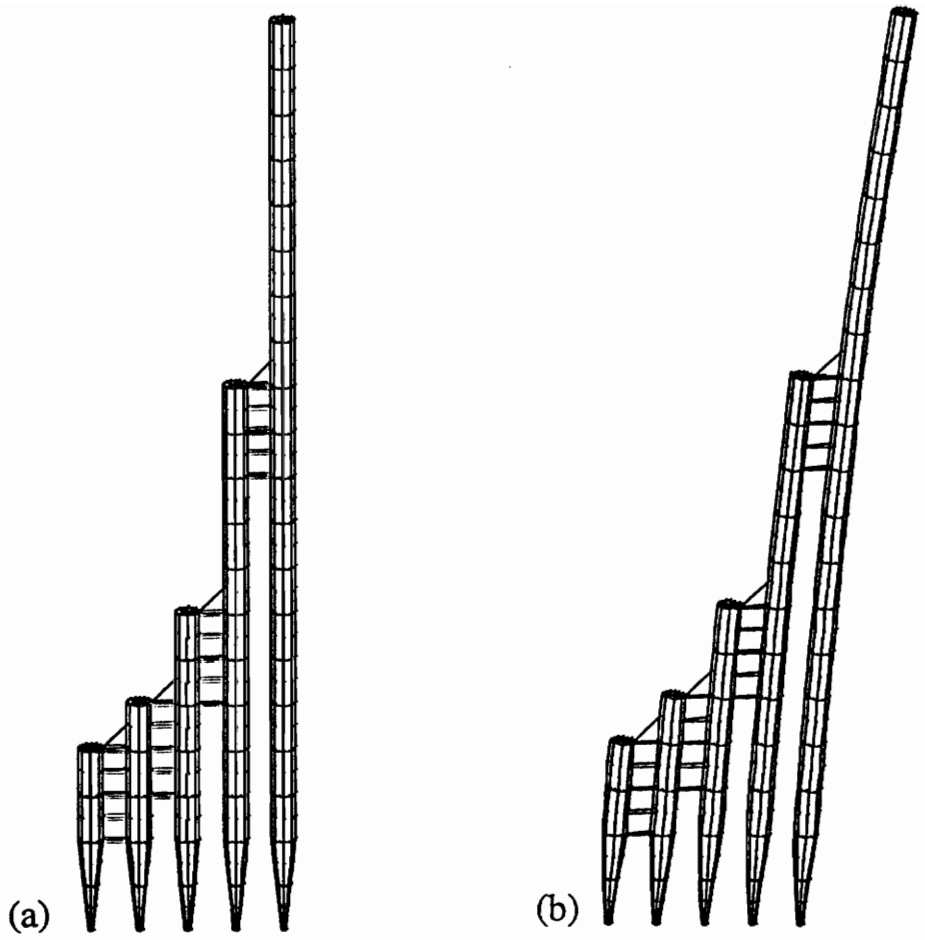

Figure 47. FEA stereocilia bundle model with exponentially increasing stereocilia heights.

(a) Undeformed structure. The shown heights do not reflect any specific experimental data. (b) Deformation results. $K = 2.95 \times 10^{-3}$ N/m. The nonuniform height differences allows for bending in the uniform region of the taller stereocilia.

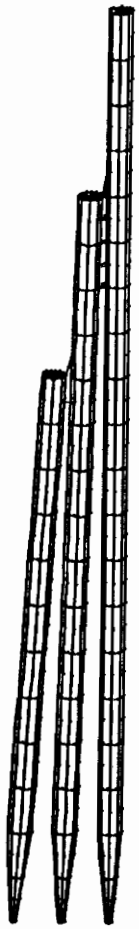

Figure 48. FEA stereocilia bundle model with convergent stereocilia axes.
This model resulted in a 40% increase in stiffness from the parallel model. The increase is due to the leaning stereocilia's resistance to extension since the force can be resolved into two components for these stereocilia, one normal to the stereocilia (extension) and one perpendicular (bending).

to note that this resulting value of stiffness is close to the value for the five cilia model discussed previously. The convergence of stereocilia axes is an important model characteristic and should be further developed in future work.

However, there is an inherent problem in the construction of this model. Experimental analyses using the calcium chelator BAPTA have indicated that the tip-links carry a pretension which results in the characteristic convergent axes (see Section 4.2). The stereocilia of Figure 48 were constructed to lean in on each other; their configuration did not result from prestress in the tip-links. The inclusion of tip-link pretension in the model would greatly increase bundle stiffness. This pretension should be considered in any future work.

4.6 CUTICULAR PLATE

In previous models, the cuticular plate was considered a rigid structure such that the stereocilia resembled cantilevered beams. The possibility of reducing bundle stiffness by relaxing this constraint was evaluated by modeling the cuticular plate. The cuticular plate consists of actin filaments from stereocilia rootlets, the actin-binding protein spectrin, and tropomyosin (Tilney et al., 1992). Since data is not available for characterizing this complex filamentous structure, the cuticular plate was modeled as isotropic actin material. The overall height of the plate was taken from an aspect ratio of 5:1, height of tallest stereocilium to height of plate. A three cilia model with the cuticular plate is illustrated in Figure 49. The applied boundary conditions were constrained nodes at the base of the plate. This allowed for shear deformation to occur in the thick plate. It was found that the plate in this configuration acted as a rigid foundation for the stereocilia bundle. No significant deformation of the plate took place, therefore no compliance was added to the overall bundle stiffness.

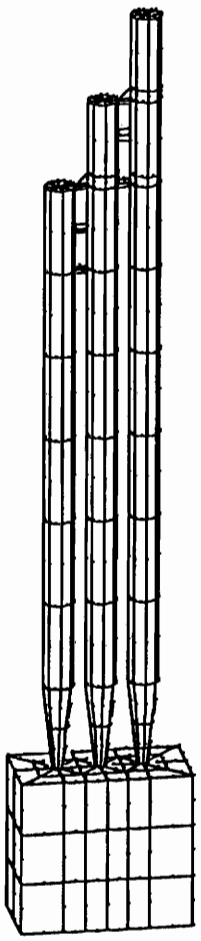

Figure 49. FEA stereocilia bundle model including the cuticular plate.
If the material structure of the plate is assumed to be that of the stereocilia, the plate acts as a rigid foundation adding negligible compliance to the model. The cantilevered assumption is valid for these models.

5.0 NONLINEAR ANALYSIS

Large deformation analysis was used to determine to what extent, if any, nonlinear theory impacts bundle stiffness at large displacements. The criterion for displacements to be considered large was a maximum deflection of the tallest stereocilium greater than 0.25 μm, which is equivalent to the stereocilium's upper diameter. The previously studied models that this criterion would impact are the stepped cross-section, load-deflection curve, and stiffness versus stereocilium Young's modulus models. The stepped cross-section model was excluded from nonlinear analysis since that particular model was rejected based on other considerations.

5.1 LOAD-DEFLECTION CURVES

Since no failure criteria was prescribed for the models, linear analysis resulted in a linear relationship between applied load and deflection with a constant slope *ad infinitum*. For the linear results in Figure 34 a and b, maximum displacements exceeded hundreds of micrometers. Considering that the tallest stereocilium is only 10 μm in height, deflections of this magnitude are obviously impossible. At large forces (above 10 nN), unrealistic deformation behavior occurred so that large displacements could be achieved. Single stereocilium models were characterized by increased diameters as in Figure 50, whereas the individual stereocilia in bundle models were distorted and even impacted each other as in Figure 51. Due to the type of elements chosen, more than one element is allowed to occupy the same space (Figure 51). Boundary elements may be applied to the stereocilia surfaces in order to prevent this from occurring. However, the use of boundary elements would not preclude the excessive buckling and distortion shown in Figure 51. In fact, experimental observations have shown the stereocilia to be quite brittle. Therefore, we would expect maximum stereocilia deflections to be of the order of a few micrometers. Nonlinear analysis should result in asymptotic behavior, limiting the maximum deflections to some reasonable value.

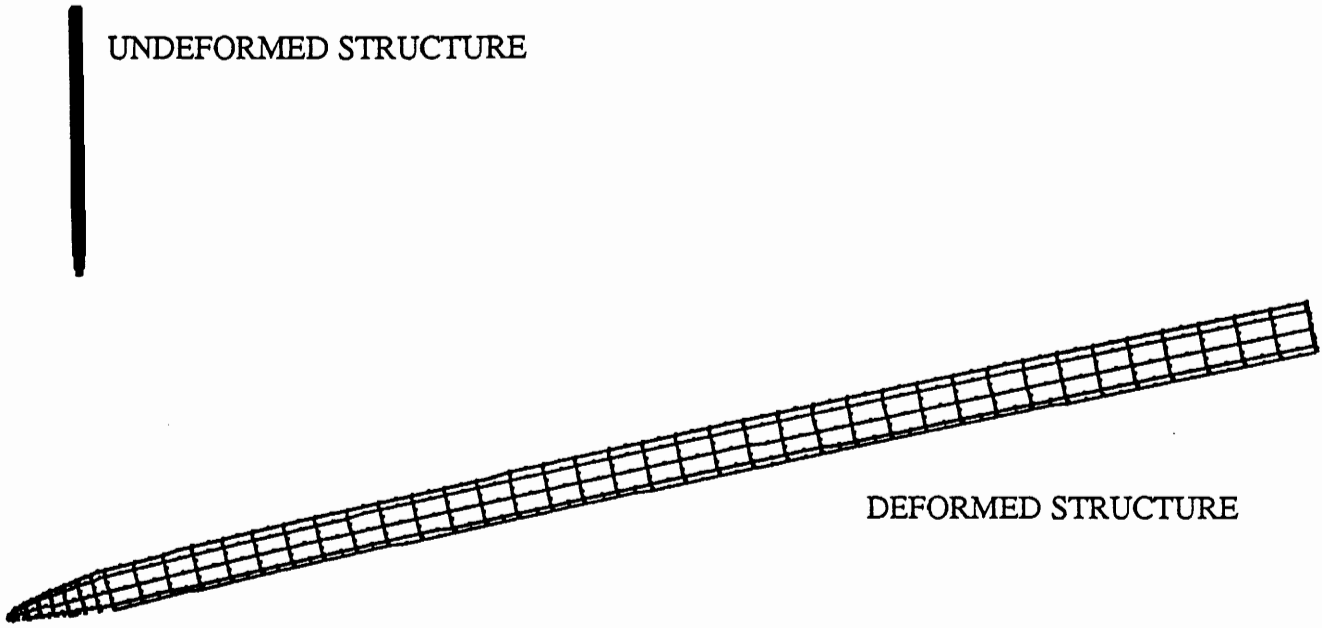

Figure 50. Increased diameter for large deformation of single stereocilia using linear analysis.

The deformed structure is shown with the original undeformed structure at the same scale. The deformed structure increased in diameter and length demonstrating the failure of linear theory to produce realistic results for large deformations.

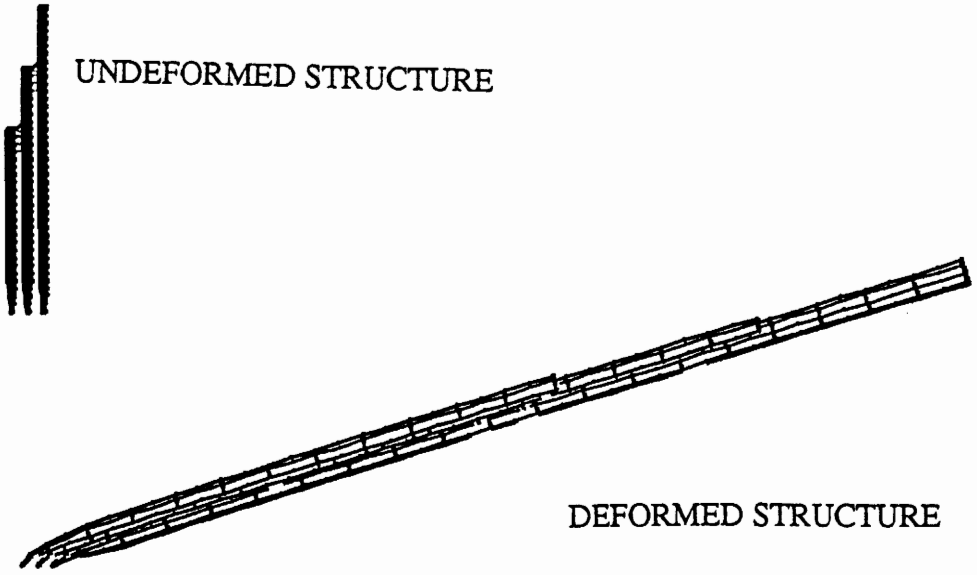

Figure 51. Increased dimensions and physical impossibilities for large deformation of a stereocilia bundle using linear analysis.

The deformed structure is shown with the original undeformed structure at the same scale. The deformed structure increased in size and is shown with the stereocilia lying within each other demonstrating the failure of linear theory to produce realistic results for large deformations.

Nonlinear analysis was first performed on the single stereocilium in order to demonstrate this asymptotic behavior. The results are shown in Figure 52, where the data points indicate the nonlinear solution and the straight line represents the constant linear solution. The nonlinear solution approaches a limiting maximum deflection of approximately 10 μm. In the range of this limiting value, the deformed stereocilium is practically horizontal, yet does not exhibit the increase in diameter evident in linear analysis. The brittle nature of the stereocilium would suggest that this magnitude of deformation is not possible. The point at which the nonlinear solution begins to diverge from the linear solution is at approximately 5 μm. It is in this range that we find the maximum possible deformation of the real structure.

Similar nonlinear analysis was performed on the stereocilia bundle model. The results shown in Figure 53 demonstrate asymptotic behavior with a limiting excitatory deflection of about 10 μm, as in the single stereocilium case. In the inhibitory direction, the finite-element solution would not converge beyond approximately 10 nN, or about -3.5 μm. Attempts at producing convergent solutions will be discussed later in this chapter. The deformation behavior at and below an applied 10 nN force (excitatory or inhibitory) was as expected physiologically as illustrated in Figure 54 a and b. Beyond this force (excitatory data only; inhibitory not available), the stereocilia buckle and impact one another. The point at which the nonlinear solution began to diverge from the linear solution was at approximately 5 μm as in the case of the single stereocilium. It is interesting to take a closer look at the load-deflection curve in the 0 to 5 μm range as shown in Figure 55. The deviation between nonlinear and linear solutions actually occurs at approximately 3.5 μm. Immediately before this deviation, between 1 and 3 μm deflections, a small fluctuation between solutions occurs where the linear solution actually underestimates the nonlinear value. This small difference in solutions may represent the real physical nature of the problem, or computation aberrations built into the solution algorithms. Nevertheless, the difference is negligible, and the structure should be considered linear up to a deflection of approximately 3.5 μm.

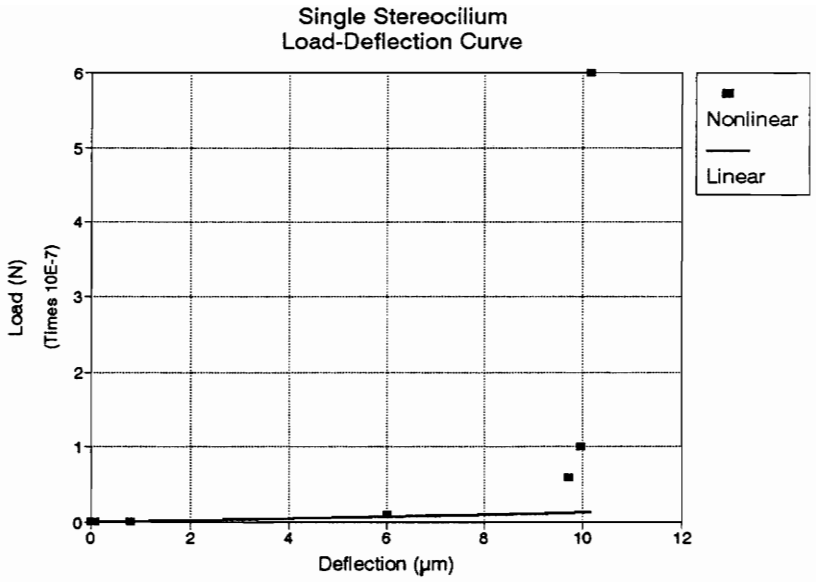

Figure 52. Nonlinear load-deflection curve for a single stereocilium.
Note a dramatic increase in stiffness at large deflections.

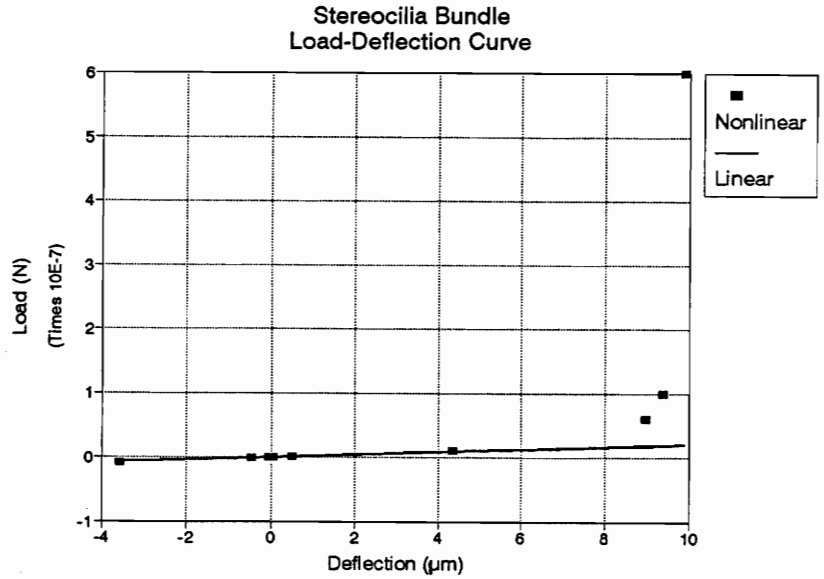

Figure 53. Nonlinear load-deflection curve for a stereocilia bundle.
Note a dramatic increase in excitatory stiffness at large deflections. Inhibitory results are also shown down to F = -10 nN. For greater inhibitory forces, the models would not converge.

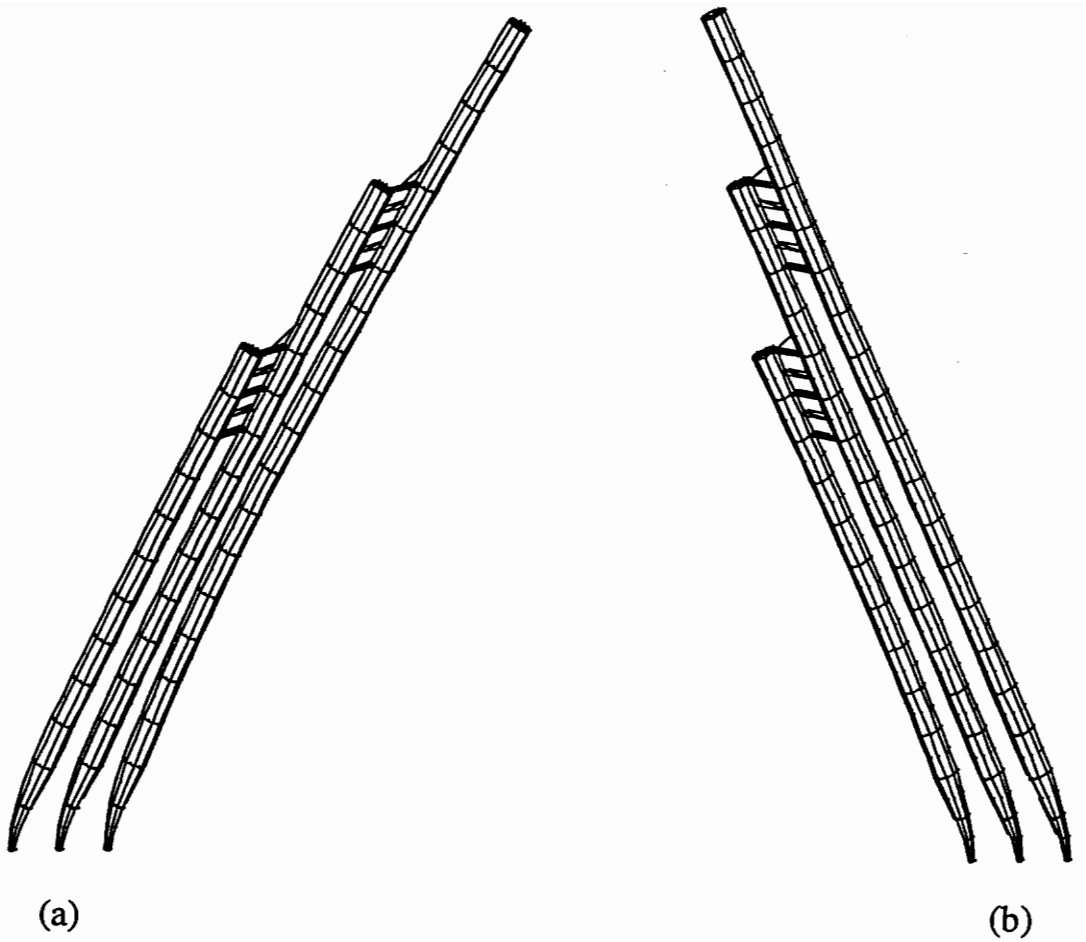

Figure 54. FEA nonlinear deformation results: F = ± 10 nN.
(a) Excitatory deformation. (b) Inhibitory deformation. The deformation behavior at and below an applied 10 nN force (excitatory or inhibitory) was as expected physiologically. Beyond this force the stereocilia buckle, distort, and impact one another.

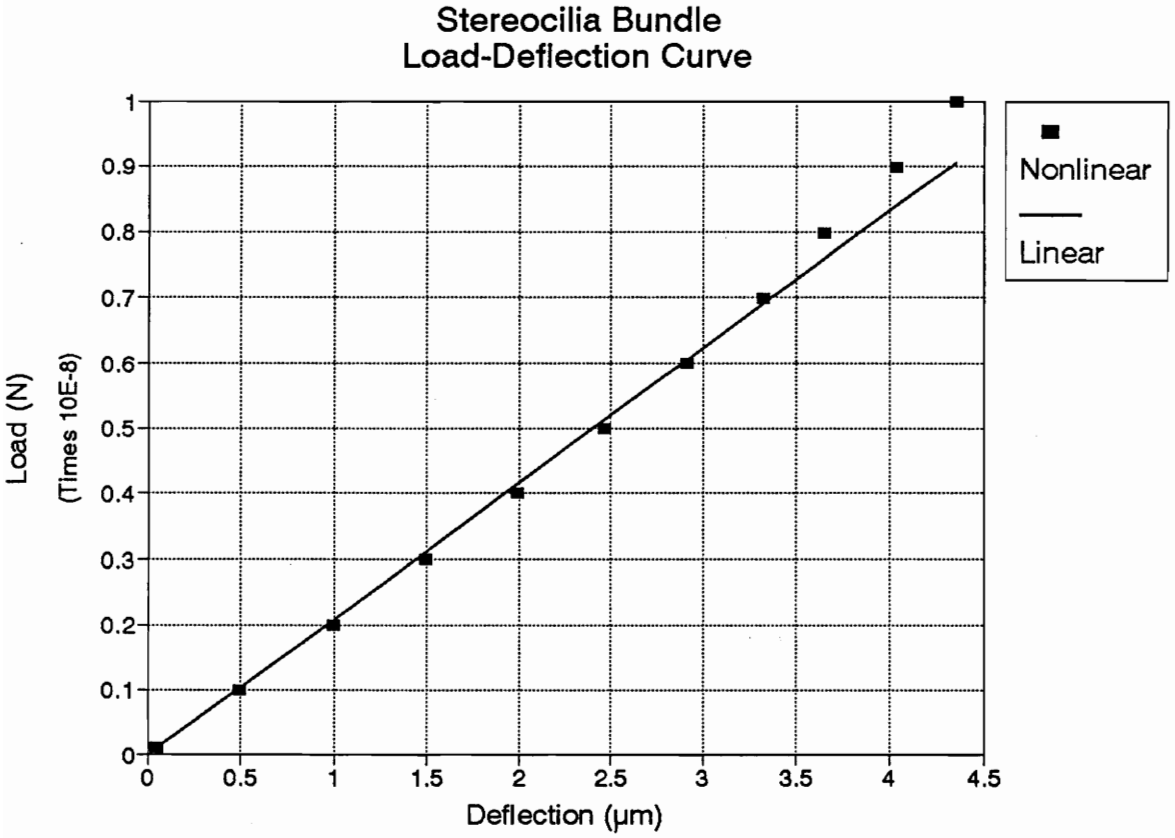

Figure 55. Nonlinear load-deflection curve for a stereocilia bundle: 0 - 5 μm deflection range.

The deviation between nonlinear and linear solutions occurs at approximately 3.5 μm. Note that between 1 and 3 μm deflections, a small fluctuation between solutions occurs where the linear solution actually underestimates the nonlinear value.

As discussed in Chapter 4.1, the linear analysis produced equal values for excitatory and inhibitory stiffness. This result was found to be consistent with experimental observations with deflections in the range of 1 to 100 nm which is well into the linear range of our model. However, some investigators (Flock and Strelioff, 1984) have observed that the stiffness is greater in the excitatory direction than in the inhibitory direction at large deflections. Some ratios of excitatory to inhibitory stiffness were as great as 2.5, however, they were obtained at greater than normal physiological deflections. In the finite-element analysis, the reverse occurred; the inhibitory stiffness was greater than the excitatory stiffness at large deflections. For example, at an applied load of 10 nN, the ratio of excitatory to inhibitory stiffness was 0.78. There are many possible explanations for this difference between computation and experimental results. Computationally, the model does not include the possibility of plastic deformations which may occur at large deflections. Also, the tip-links are thought to be flaccid in the inhibitory direction (Howard and Hudspeth, 1988). In other words, the tip-links carry little or no compressive loads. This important physiological characteristic was not included in the finite-element model. Additional degrees of complexity will be required in the FEA model in order to demonstrate this effect.

5.2 STEREOCILIA MODULUS

In the linear analysis in Chapter 4.4, the stereocilia Young's modulus was decreased over a range from 3 GPa to 3 MPa to determine its effect on stiffness. A distinct transition in deformation behavior was shown to occur at 300 MPa. Above this value, the stereocilia bundle deformed as expected physiologically. Below this value, the bundle began to twist into an S-shape in the region of the subapical bands. A Young's modulus of 300 MPa also marked the transition from small to large deformations. Above this value, the maximum stereocilium deflection was considered small, and linear analysis could be considered reliable. Below this Young's modulus, the maximum deflection was greater

than the 0.25 μm criterion. Therefore, nonlinear deformation theory was used to determine possible deviations from the linear solution.

As in the inhibitory direction of the load-deflection analysis above, problems occurred in obtaining convergent solutions. All models converged down to a Young's modulus of 10 MPa. Below this value the solutions appeared divergent, resulting in the cessation of the finite-element analysis. The data that I was able to obtain followed the linear solution almost exactly. The deformation behavior below a Young's modulus of 300 MPa again twisted and buckled suggesting that the 300 MPa lower limit of the stereocilia's Young's modulus was still applicable.

The nonlinear analysis uses an incremental approach where the loads are applied in 'increments' and at each increment the equilibrium equations must be satisfied. The time axis ranges from 0 to 1 since this is a static operation. In other words, one unit in time represents the fully loaded model, whereas fractional increments in time indicate the fraction of the load step completed. Figure 56 shows the displacement versus increment in time for the 10 MPa Young's modulus model. This data provides possible insight into the reasons for obtaining nonconvergent solutions. The buckling behavior characteristic of models with stereocilia Young's modulus below 300 MPa began to occur at 40% of the load step competed. After this point, warnings of excessive element distortions occurred at almost every increment. These warnings indicate that small increments in time resulted in extremely large increments in displacement. In this case, the step in time would have to be decreased in order to obtain a convergent solution at that increment. If the step in time had to be decreased more than five times for any one increment, the solution was considered to be diverging, and the analysis stopped.

5.3 NONCONVERGENT SOLUTIONS

For nearly incompressible materials, ABAQUS has specialized elements called hybrid elements. Small changes in displacement in incompressible materials produce large changes in pressure. Therefore, a displacement based solution is too sensitive to be

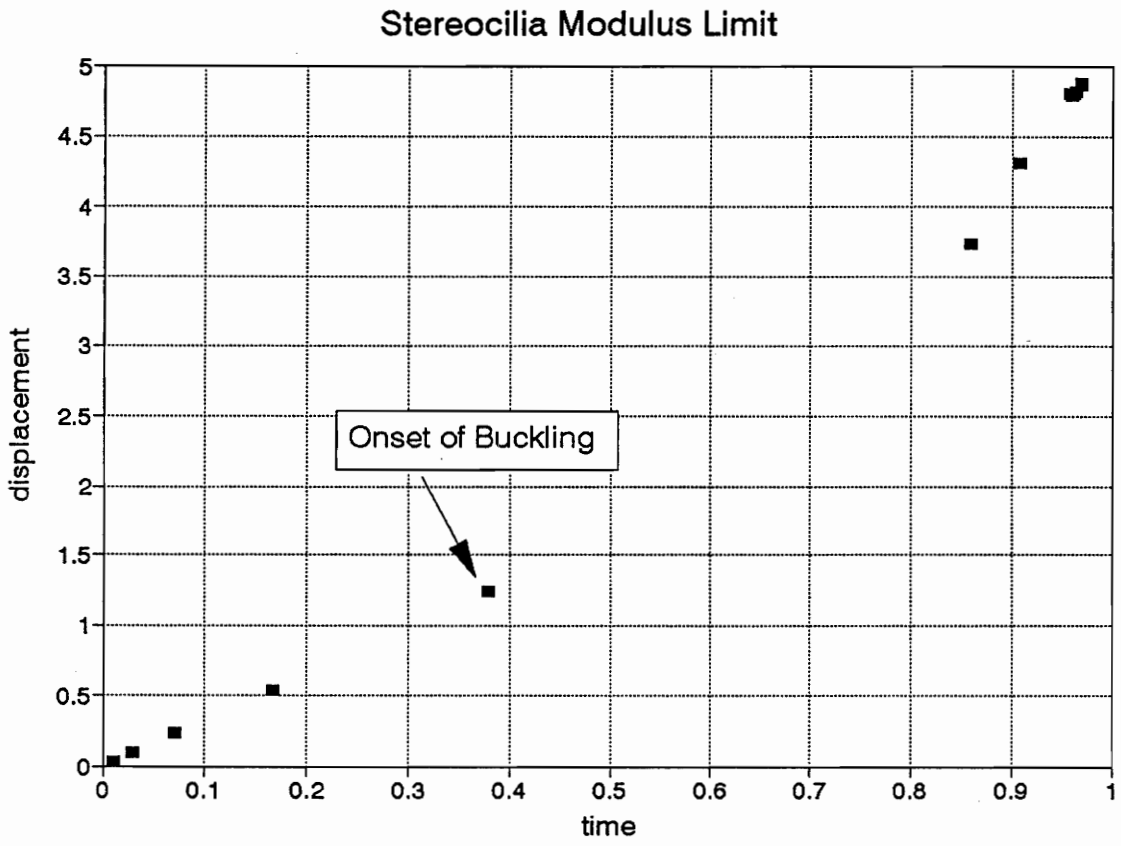

Figure 56. Bundle displacement versus increment in time for a stereocilia Young's modulus of 10 MPa.

At this value for stereocilia Young's modulus, the model solution would not converge past 97% of the load step completed. At 40% of the load step completed, the model began to buckle similar to the linear solution. Beyond this point, the solution algorithm warned of excessive element distortions. This point corresponds to small increments in time which resulted in large increments in displacement. The solution was then determined to be divergent.

useful. To remove this sensitivity, the pressure stress variables are coupled to the displacement solution by a Lagrange multiplier. Therefore, the hybrid elements are considered "mixed formulation" elements. Since the stereocilia material was considered nearly incompressible and the displacement solution is most sensitive at large strains, hybrid elements were used in the case of large deformations to determine their effect on stiffness.

In all cases where the nonlinear solution converged using general elements, the solution also converged when using hybrid elements. The reduction in stiffness was less than 2% and was considered negligible. For models that previously did not converge, the use of hybrid elements also did not result in convergence. In fact, analyses using hybrid elements terminated (diverged) at earlier increments than those using general elements.

Other suggestions to increase the chances of convergence could include the use of rigid boundary elements to reduce the freedom to buckle, an increase in the number of attempts at convergence for each increment, and the use of smaller steps in time throughout the incremental time history.

6.0 BUNDLE NATURAL FREQUENCIES

Traditionally, the frequency response of the human auditory system has been determined to have a bandwidth ranging from 20 to 20,000 Hz. Recently, it has been reported that human hearing well beyond 20 kHz (ultrasonic range) has been achieved through ultrasonic bone conduction (Lenhardt et al., 1991). In fact, frequencies up to 108 kHz transmitted through stimulation of the skull have induced perceptions of sound. In the past scientists have attributed ultrasonic hearing phenomenon as a by-product of cochlear processing. Ultrasonic perception in sensori-neural deaf subjects tends to counter this argument.

Tests conducted at the Medical College of Virginia support the idea of bone-conducted ultrasonic hearing in normal, older hearing-impaired, and profoundly deaf human subjects (Lenhardt et al., 1991). The profoundly deaf subjects incurred their hearing loss due to highly damaged cochlea (sensori-neural deafness). Ultrasonic frequencies ranging from 25 to 32 kHz were presented to each of these subject groups. To determine the ability of sound perception, frequency discrimination and speech detection tests were performed. The frequency discrimination tests involved the use of pure tones at discrete intervals. An electronic circuit was built to step audio frequencies up to the ultrasonic range. The subject could then be tested for the ability to discriminate between different tones. The speech detection tests involved the subject discriminating between a given word and other phonically similar words. An encouraging range of 20 to 30% accuracy was demonstrated in word recognition for the profoundly deaf subjects.

Current thinking (J. W. Grant, personal communications) has proposed a resonance model for ultrasonic hearing. Although the objectives of this paper are directed towards better understanding hair bundle mechanics, stiffness, and mechanoelectrical transduction processes, the ultimate goal of and financial support for this project comes from this idea of modeling human ultrasonic hearing.

As a preliminary effort towards this goal, the ten lowest modes of vibration were determined for the finite-element model. The density of the model material was prescribed in order to obtain the vibration modes. The density of protein is 1300 kg/m^3. Adding mass units to the finite-element model required particular caution. The force units were previously prescribed as newtons (N), whereas the length units were prescribed as micrometers (μm). The correct units for density can be determined by considering Newton's Law of Motion in the form

$$F = \rho V a \tag{21}$$

where F is force, ρ is density, V is volume, and a is acceleration. By performing simple dimensional analysis on the above equation, density with the correct units becomes 1300 x 10^{-24} $kg \cdot m/\mu m^4$. This value for density was used for all materials in the finite-element model.

The ten lowest modes of vibration are shown in Figure 57. Interestingly, the lowest two modes primarily bend out of the plane of increasing stereocilia height, however, these modes have not been observed in nature. Mode 3 most closely resembles the deformation behavior of the stereocilia bundle. The natural frequency corresponding to this mode is 382 kHz. This value is within an order of magnitude of the value predicted by lumped parameter models (J. W. Grant, personal communications). The lumped parameter model was based on average experimental bundle stiffnesses and included damping to obtain a damped natural frequency. Both of these factors would reduce the natural frequency above to within expected ranges. Many of the resulting modes (e.g. mode 10) are physically inadmissable at the magnitudes shown, however, the eigenvalues could be adjusted to allow such modes. As a preliminary result, the finite-element method seems feasible for further study of bundle resonance.

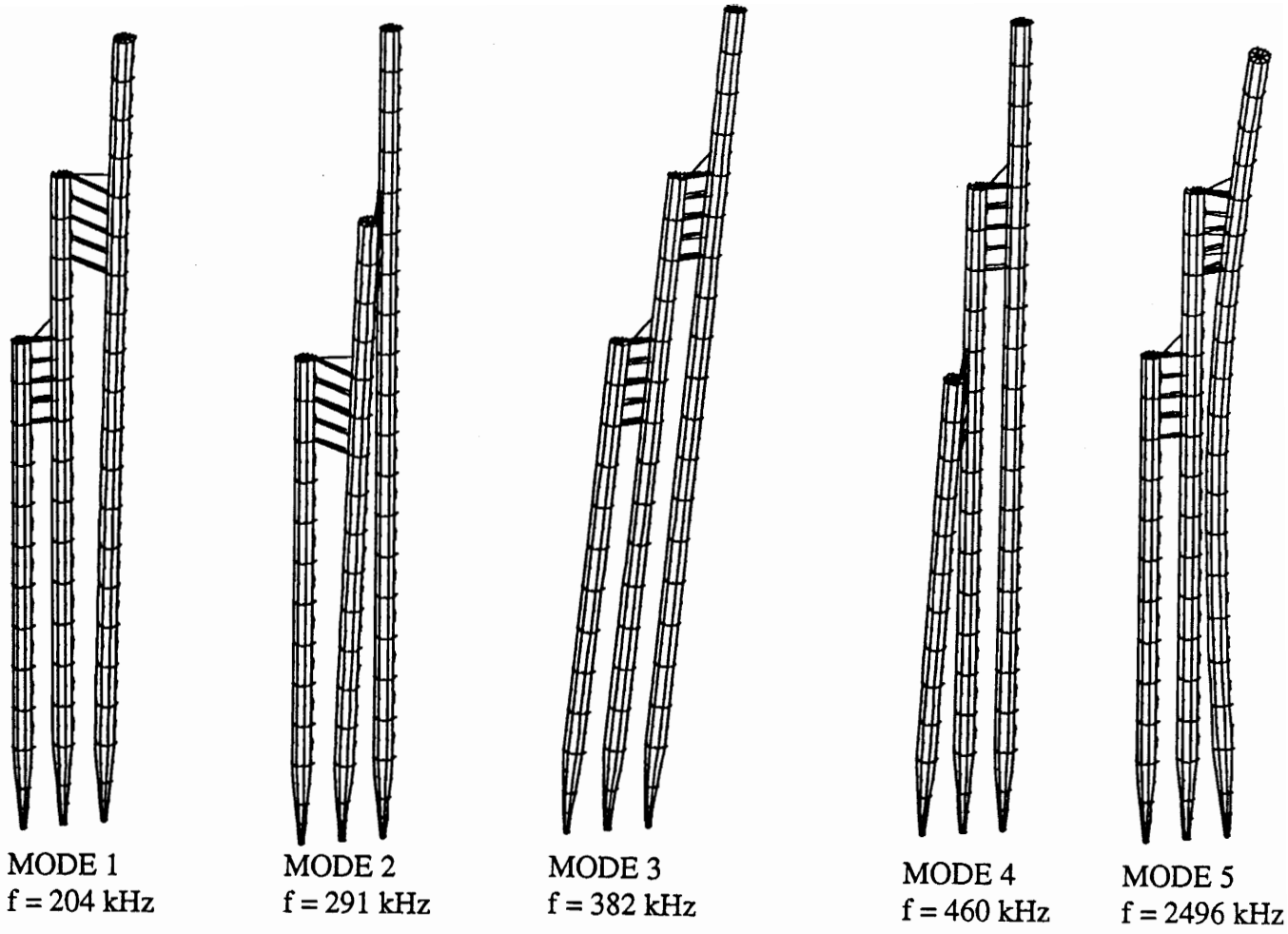

Figure 57. FEA stereocilia bundle model vibration modes.
The above deformation plots correspond to the ten lowest modes of oscillation. The mode shape similar physical deformations is mode 3 corresponding to a natural frequency of 382 kHz.

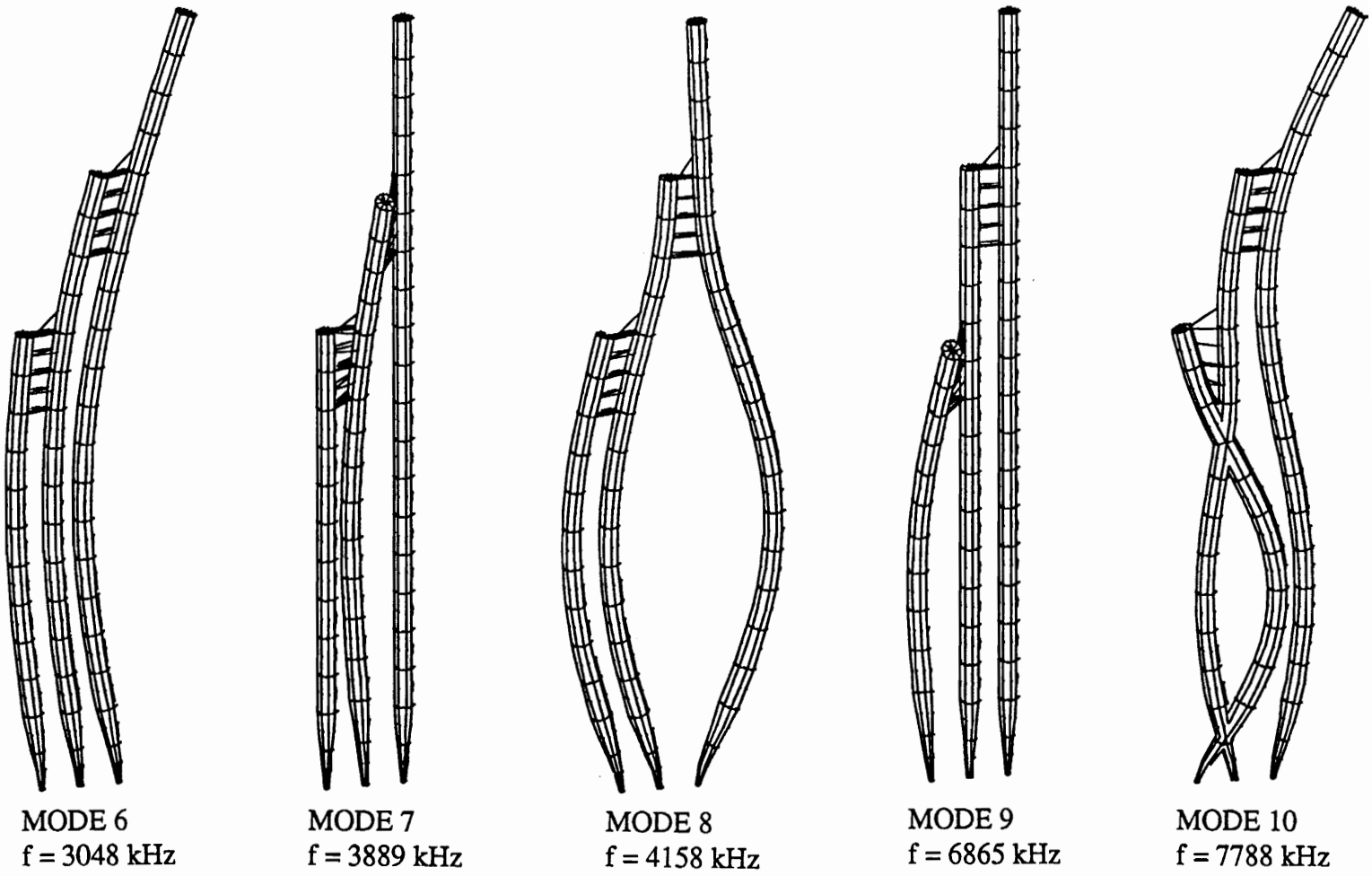

Figure 57. FEA stereocilia bundle model vibration modes (CONTINUED).

7.0 SUMMARY AND CONCLUSIONS

The inner ear is a labyrinth of sensory organs containing specialized hair cells responsible for sensing hearing and motion. The mechanoelectrical transduction from these mechanical events to nerve impulse responses is achieved by the deflection of ciliary bundles on the hair cells by surrounding media. The magnitude of bundle deflection, proportional to nerve spike train frequency, is controlled by bundle stiffness. The aim of this research was to adequately characterize bundle geometry producing reliable estimates of overall bundle stiffness. Geometric and material model parameters were then manipulated in a computational environment in order to determine their contributions to stiffness.

An analytical solution formed the basis by which to validate the finite-element (computational) solution. Model formulation began by representing a single stereocilium by a stepped cross-section model. In this configuration, the tapered stereocilium base was considered to be a cylinder of constant radius. This analysis provided several conclusions.

- From the analytical solution, the maximum error in stiffness if shear effects were neglected was less than 1%.
- Stereocilium stiffness decreases with increasing uniform and taper heights.
- Stereocilium stiffness increases with increasing radii.
- FEA and analytical solutions gave stiffness as 3.27×10^{-4} N/m for the stepped cross-section model.

In order to determine the reliability of the stepped cross-section assumption, a 3-D model was constructed including a cone-shaped taper at the base of the stereocilium. The resulting analysis indicated the following:

- The stiffness trends established by the stepped cross-section model continued with the tapered base model.

- However, the analytical values of stereocilium stiffness were five times greater than the stepped cross-section model. Therefore, the tapered base model should be uses as the basis for constructing a FEA stereocilia bundle model.

A stereocilia bundle model was constructed by coupling three, increasing in height tapered base stereocilia. The coupling mechanisms were of two types: (1) subapical linkages and (2) tip-links.

- The subapical linkages were first modeled as a solid interconnection which was found to produce large increases in stiffness and physiologically inconsistent deformation behavior.
- The subapical linkages, as well as the tip-links, are best modeled with spring elements.
- A standard model was constructed using this configuration. The stiffness for this model was 2.1 x 10^{-3} N/m, which is within the range of experimental data.

The development of a standard, linear theory model provided a basis for comparing the effect on stiffness of specific model parameters. These parameters included the density of interconnections and Young's modulus for the subapical bands, the orientation angle and Young's modulus for the tip-links, and bundle width, stereocilia height variations, and stereocilia Young's modulus for the overall bundle geometry. The following conclusions could be made:

- Stiffness depends most strongly on:
  (1) individual stereocilium geometry and material description,
  (2) tip-link orientation angle and material description,
  (3) total number of stereocilia, and
  (4) stereocilia center-to-center spacing.

- Stiffness also depends strongly on parallel versus non-parallel stereocilia. Convergent stereocilia axes increased stiffness 40% from the standard, parallel model.
- Stiffness depends least on:
    (1) stereocilia height variations,
    (2) subapical band height as long as at least one row is present, and
    (3) subapical band material description.

Nonlinear analysis was performed on models exceeding deflections of 0.25 μm. The results indicated the limit up to which linear analysis would provide reliable estimates of stiffness. The analysis indicated:

- Linear theory was reliable up to deflections of 3.5 μm. Beyond this value the response is nonlinear resulting in dramatic increases in stiffness. However, experimental evidence and the brittle nature of the stereocilia would suggest that deflections past this limit do not occur in nature.
- Some analyses failed to obtain convergent solutions. However, these models did converge up to some fraction of the load step completed. In each case, the completed load step produced deflections beyond physical reality.

The motivating force behind this work, beyond simple academic endeavor, is the possibility of providing some insight into the dynamic response of the hair cell for use in the ultrasonic hearing resonance model. Preliminary dynamic response indicates a natural frequency of 382 kHz for the vibration mode resembling physical deformation behavior.

This model has proven to give stiffness values, deformation behavior, and natural frequencies within expected experimental data ranges and consistent with previous modeling efforts. Therefore, it should be considered a reliable tool for describing trends in stereocilia bundle stiffness.

8.0 FUTURE WORK

The preceding work should be considered preliminary. There are possibly no instances when modeling the human anatomy that linear, elastic, isotropic, homogeneous assumptions can be reliably made. The modeling of inner ear hair cells is no exception. Although the model produced adequate estimates of stereocilia bundle response, assumptions as those above should be relaxed to determine any significant effects on stiffness, which inherently effects dynamic response. This chapter will highlight specific areas that would most strongly impact bundle stiffness and the validity of the model. These areas include experimental and mathematical corroboration, viscoelastic behavior and pretension in the tip-link, transversely isotropic stereocilia material descriptions, and hexagonal bundle arrangements.

8.1 MODEL CORROBORATION

A disadvantage in the current model is inherent in the accumulation of experimental data. This data (see Table 1) was obtained from a variety of species and locations in the sensory organs. Geometric and stiffness data varied over a wide range. In order to further validate the model, experimental data from the same cell or neighboring cells should be obtained. This method would allow the results of a FEA model to be compared with the cell from which it was constructed. One such approach is being developed at Virginia Tech (J. W. Grant, personal communications).

Another possible method of model corroboration is the use of a mathematical analog such as that proposed by Howard and Hudspeth (1988). Figure 58a illustrates the spring-damper configuration with the upper region of the stereocilium considered to be a rigid lever arm and the tapered base, a torsional spring. Howard and Hudspeth condensed this structure into a spring-damper analog as shown in Figure 58b. However, this representation of the model is oversimplified. The actual connectivity is shown in Figure 58c. Mass, stiffness, and damping matrices can be obtained from this representation.

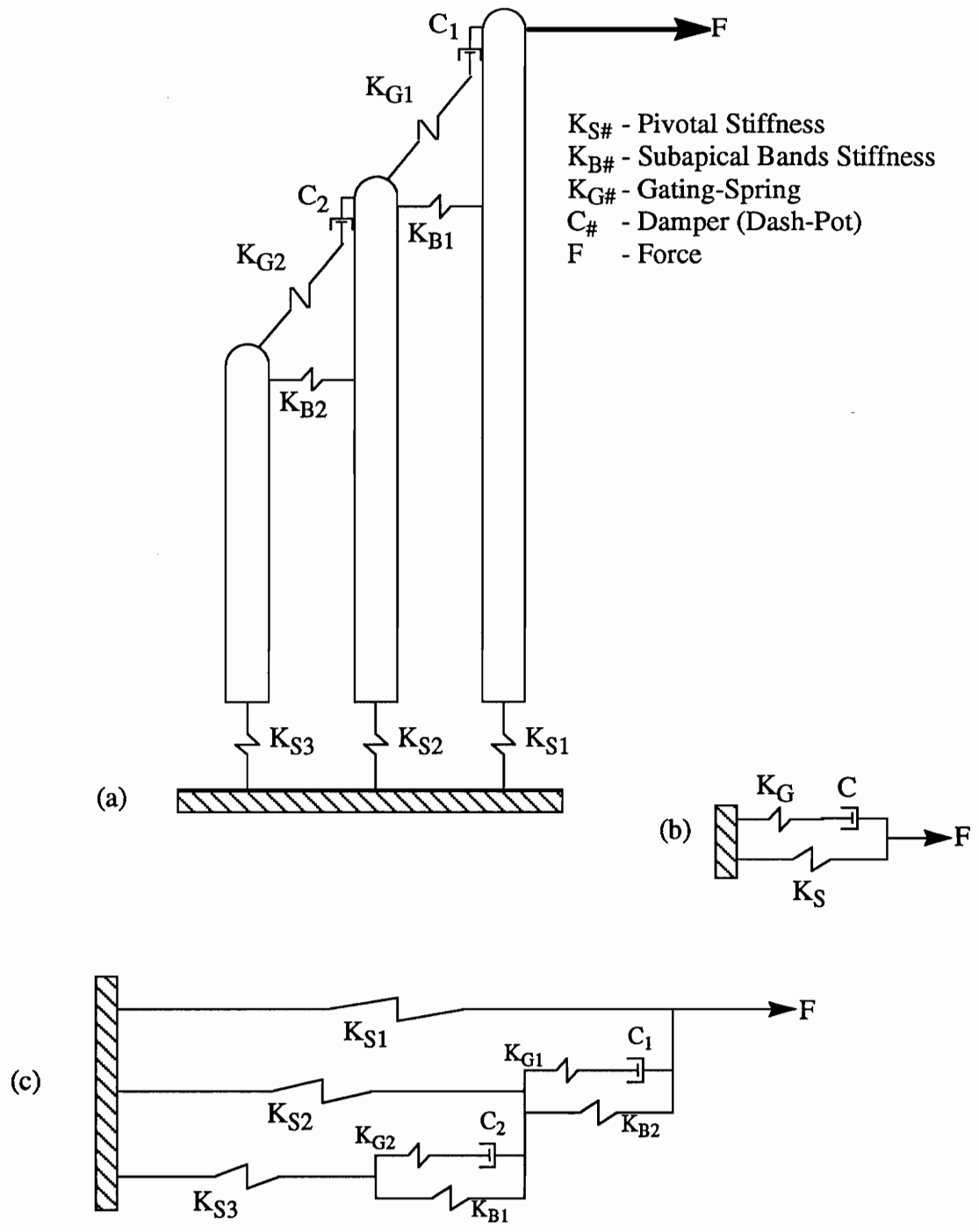

Figure 58. Spring-damper analog model.
(a) Stereocilia bundle spring-damper configuration. (b) The traditional gating-spring model analog (Howard and Hudspeth, 1988). (c) An expanded spring-damper analog model.

Modal analysis and dynamic responses can be obtained from the resulting matrix equations of motion. The natural frequencies could then be compared with FEA analysis.

8.2 TIP-LINK MODEL

The illustration of Figure 58a shows a damping action in the tip-link. This element is a result of adaptation in the stereocilia bundle. Constant bundle deflection has been associated with a shift in the sensitivity curve (Pickles and Corey, 1992). This shift represents an active mechanism involved in the adjustment of tip-link tension during deflection. The adjustment mechanism is represented as the damping element in Figure 58a. The finite-element model should include such viscoelastic behavior because of its obvious implications in dynamic analysis. Another important aspect of the tip-link is apparent pretension believed to cause the leaning behavior of the stereocilia (Assad et al., 1991).

8.3 STEREOCILIA MATERIAL DESCRIPTION

Tilney et al. (1983) showed that the actin filaments within the stereocilium slide across one another during deflection (see Figure 9), such that the actin cross-bridges remain parallel to the cuticular plate. This type of behavior is obviously inconsistent with the plane-sections-remain-plane assumptions inherent in the linear, elastic, isotropic, homogeneous stereocilia material description. Research into the biochemical nature of the actin cross-bridge bonding sites should be made. Also, a material description for the cross-bridges (possibly the protein fimbrin) should be obtained. This information would allow transversely isotropic stereocilia material descriptions to be incorporated into the FEA model.

8.4 HEXAGONAL BUNDLE ARRANGEMENTS

Although the three stereocilia bundle used in this paper would adequately model the three parallel rows of cochlear inner hair cells, other stereocilia bundles in the inner ear

do not have such a symmetric nature. Vestibular hair bundle (see Figure 11) could better be approximated by a hexagonal array of stereocilia. Side-to-side as well as row-to-row subapical bands would then play a role in determining stereocilia bundle stiffness. The resulting stiffness would be expected to increase dramatically. Therefore, it is important that future work include such a complex geometry.

The above suggestions represent four distinct areas where the FEA stereocilia bundle model could be greatly enhanced. The ensuing computational model would serve as a powerful tool in the understanding of hair cell bundle mechanics.

REFERENCES

ABAQUS Manuals. 1989. Hibbitt, Karlsson, and Sorenson, Inc.

Ashmore JF. 1984. The stiffness of the sensory hair bundle of frog saccular hair cells. *Journal of Physiology* 350:20P.

Assad JA, Shepherd GMG, Corey DP. 1991. Tip-link integrity and mechanical transduction in vertebrate hair cells. *Neuron* 7:985-994.

Bagger-Sjoback D, Takumida M. 1988. Geometrical array of the vestibular sensory hair bundle. *Acta Otolaryngologica* 106:393-403.

Corey DP, Hudspeth AJ. 1979. Response latency of vertebrate hair cells. *Biophysics Journal* 26:499-506.

Crawford AC, Fettiplace R. 1985. The mechanical properties of ciliary bundles of turtle cochlear hair cells. *Journal of Physiology* 364:359-379.

Denk W. Webb WW, Hudspeth AJ. 1989. Mechanical properties of sensory hair bundles are reflected in their Brownian motion measured with a laser differential interferometer. *Proceedings of the National Academy of Sciences, USA* 86:5371-5375.

Duncan RK, Grant JW. 1993. Finite element analysis of stereocilia bundle stiffness: interconnection effects. *ARO Conference* (Abstract #324).

Flock A, Strelioff D. 1984. Graded and nonlinear mechanical properties of sensory hairs in the mammalian hearing organ. *Nature* 310:597-599.

Friedmann I, Ballantyne J. 1984. *Ultrastructural Atlas of the Inner Ear.* Butterworths, London.

Furness DN, Hackney CM. 1985. Cross-links between stereocilia in the guinea pig cochlea. *Hearing Research* 18:177-188.

Grant JW. Associate Professor, Department of Engineering Science and Mechanics, Virginia Polytechnic Institute and State University. Personal communications.

Hackney CM, Furness DN, Benos DJ. 1991. Localization of putative mechanoelectrical transducer channels in cochlear hair cells by immunoelectron microscopy. *Scanning Microscopy* 5(3):741-746.

Hackney CM, Furness DN, Benos DJ, Woodley JF, Barratt J. 1992. Putative immunolocalization of the mechanoelectrical transduction channels in mammalian cochlear hair cells. *Proceedings of the Royal Society* 248:215-221.

Howard J, Ashmore JF. 1986. Stiffness of sensory hair bundles in the sacculus of the frog. *Hearing Research* 23:93-104.

Howard J, Hudspeth AJ. 1987. Mechanical relaxation of the hair bundle mediates adaptation in mechanoelectrical transduction by the bullfrog's saccular hair cell. *Proceedings of the National Academy of Sciences, USA* 84:3064-3068.

Howard J, Hudspeth AJ. 1988. Compliance of the hair bundle associated with gating of mechanoelectrical transduction channels in the bullfrog's saccular hair cell. *Neuron* 1:189-199.

Hudspeth AJ. 1992. Extracellular current flow and the site of transduction by vertebrate hair cells. *Journal of Neuroscience* 2:1-10.

Hudspeth AJ, Corey DP. 1977. Sensitivity, polarity, and conductance change in the response of vertebrate hair cells to controlled mechanical stimuli. *Proceedings of the National Academy of Sciences, USA* 74(6):2407-2411.

Jacobs RA, Hudspeth AJ. 1990. Ultrastructural correlates of mechanoelectrical transduction in hair cells of the bullfrog's internal ear. *Cold Spring Harbor Symposium on Quantitative Biology* 55:547-561.

Lenhardt ML, Skellett R, Wang P, Clarke AM. Human ultrasonic speech perception. *Science* 253:82-85.

Ohmori H. 1988. Mechanical stimulation and FURA-2 fluorescence in the hair bundle of dissociated hair cells of the chick. *Journal of Physiology* 399:115-137.

Osborne MP, Comis SD, Pickles JO. 1988. Further observations on the fine structure of tip-links between stereocilia of the guinea pig cochlea. *Hearing Research* 35:99-108.

PATRAN Plus User Manual. 1990. PDA Engineering, Costa Mesa.

Perkins WH, Kent RD. 1986. *Functional Anatomy of Speech, Language, and Hearing.* Pro-ed, Austin.

Peterson EH. Professor, Department of Biological Sciences, Ohio University. Personal communications.

Pickles JO. 1985. Recent advances in cochlear physiology. *Progress in Neurobiology* 24:1-42.

Pickles JO, Corey DP. 1992. Mechanoelectrical transduction by hair cells. *TINS* 15:254-259.

Reddy JN. 1984. *An Introduction to the Finite Element Method.* McGraw Hill, New York.

Russell IJ, Richardson GP, Kossl M. 1989. The response of cochlear hair cells to tonic displacements of the sensory hair bundle. *Hearing Research* 43:55-70.

Strelioff D, Flock A. 1984. Stiffness of sensory-cell hair bundles in the isolated guinea pig cochlea. *Hearing Research* 15:19-28.

Szymko YM, Dimitri PS, Saunders JC. 1992. Stiffness of hair bundles in the chick cochlea. *Hearing Research* 59:241-249.

Tilney LG, Egelman EH, DeRosier DJ, Saunders JC. 1983. Actin filaments, stereocilia, and hair cells of the bird II. *Journal of Cell Biology* 96:822-834.

Tilney LG, Tilney MS, DeRosier DJ. 1992. Actin filaments, stereocilia, and hair cells: how cells count and measure. *Annual Reviews of Cell Biology* 8:257-374.

VITA

Robert Keith Duncan was born in Chattanooga, Tennessee on March 25, 1969. He spent his formative years in Kings Mountain, North Carolina graduating from Kings Mountain Senior High School in 1987. He received his Bachelor of Science in 1992 from Virginia Polytechnic Institute and State University in Engineering Science and Mechanics. During this time he co-oped with the Central Intelligence Agency and completed an undergraduate research project with the Center for Adhesive Sealant Sciences under the guidance of Dr. David Dillard. Mr. Duncan, a local church youth leader, enjoys spending his time studying and teaching about his faith. In addition to these academic pursuits, he also enjoys taking time at the piano. Upon graduation, he will matriculate in the University of Pennsylvania's doctoral program in Bioengineering.